

Aus dem Institut für Pathologie der Medizinischen Fakultät Mannheim

(Direktor. Prof. Dr. med. Alexander Marx)

**Thymic Tissue Metabolomics and Bioengineering of an Artificial Thymic Carcinoma 3D
Cell Culture for in vitro 3D/2D Drug Screening and the Investigation of Toxicity
Employing a Novel Nuclear Magnetic Resonance Technique**

Inauguraldissertation

zur Erlangung des akademischen Grades Doctor scientiarum humanarum

(Dr. sc. hum.)

der

Medizinischen Fakultät Mannheim

der Ruprecht-Karls-Universität

zu

Heidelberg

vorgelegt von

Mohammad AlWahsh

aus

Dubai

2021

Dekan: Prof. Dr. med. Sergij Goerd

Referent: Prof. Dr. med. Alexander Marx

CONTENT

CONTENT	1
LIST OF ABBREVIATIONS	1
LIST OF FIGURES	3
LIST OF TABLES	6
1 Introduction	7
1.1 Thymus and thymic malignancies	7
1.2 Metabolomics	7
1.3 Metabolic re-programming.....	8
1.4 Nuclear Magnetic Resonance Spectroscopy techniques employed for metabolic studies	9
1.4.1 The Signals of Nuclear Magnetic Resonance	10
1.4.2 High Resolution Magic Angle Spinning (MAS)-NMR spectroscopy for metabolic profiling of intact tissues	11
1.4.3 The tools and inserts used in HR-MAS-NMR spectroscopy	12
1.4.4 NMR measurement techniques.....	13
1.4.5 Cryogenic NMR	15
1.5 Cell culture	16
1.6 Bortezomib (BTZ).....	19
1.7 Aims of the study	20
2 MATERIAL AND METHODS	21
2.1 Material	21
2.1.1 Consumables	21
2.1.2 Equipment	22
2.1.3 NMR chemicals, standards and consumables.....	24
2.1.4 Software.....	25
2.1.5 Media and buffers.....	26
2.1.6 Chemicals and reagents	26
2.1.7 Patients and Tissue Samples.....	28
2.1.8 Cell lines.....	29
2.1.9 Primers.....	29
2.2 Methods	30
2.2.1 Human Tissue Samples of Thymic Epithelial Tumors (TETs)	30
2.2.1.1 Tissue Sample Preparation	30

2.2.1.2 HR-MAS- ¹ H-NMR measurement conditions.....	31
2.2.1.3 NMR related statistical Analysis for tissue samples	32
2.2.1.4 MetPA analysis of metabolite profiles for metabolic pathway detection.....	33
2.2.1.5 Metabolic gene set enrichment analysis of the TCGA transcriptomic dataset.....	33
2.2.1.6 Transcriptomics related statistical Analysis	34
2.2.1.7 Analysis of online available datasets.....	34
2.2.1.8 General statistical Analysis	35
2.2.2. Two Dimensional and Three Dimensional cell culture	35
2.2.2.1 Cultivation of TET cell lines	35
2.2.2.2 Cell thawing and cryopreservation.....	35
2.2.2.3 Passaging the cells.....	36
2.2.2.4 Methanol extraction for 2D cells.....	36
2.2.2.5 NMR measurement conditions for 2D cell culture.....	37
2.2.2.6 NMR related statistical Analysis for 2D.....	37
2.2.2.7 Formation of spheroids.....	38
2.2.2.8 Novel NMR measurement setup for spheroids as a new tool to investigate the metabolism of 3D cell culture systems with time and spatial resolution under viable conditions.	40
2.2.2.9 NMR measurement conditions for spheroids	48
2.2.2.10 NMR related statistical Analysis for 3D cells	48
2.2.2.11 Drug Treatment	49
2.2.2.12 CellTiter-Glo® Luminescent Cell Viability Assay	49
2.2.3 Laser Scanning Confocal Microscopy (LSCM)	50
2.2.4 Antibody staining	51
2.2.4.1 Fixation, Embedding and slicing.....	51
2.2.4.2 Staining.....	52
3 Results	53
3.1 Tissue metabolomics of thymic epithelial tumors (TETs): To identify altered metabolic signatures in aggressive TETs in order to open new targeted therapeutic options for nonresectable thymomas and thymic carcinomas.	53
3.1.1 ¹ H NMR spectroscopy reveals 37 metabolites in TETs	53
3.1.2 Metabolic profiles are closely associated with the WHO histotypes of TETs	56
3.1.3 ¹ H NMR spectral analysis discriminates ‘indolent’ from ‘aggressive’ TETs.....	58
3.1.4 ¹ H NMR analysis reveals differentially activated metabolic pathways in TETs	60
3.1.5 Transcriptome-based metabolic pathways are differentially enriched in TETs	61
3.2 Investigation of the metabolism of a 3D cell culture model with time and spatial resolution under viable conditions: Application of a new flow NMR technique	66

3.3 Production of 3D cell culture with two new techniques and characterization of the spheroids obtained	71
3.3.1 Preparation of spheroids	71
3.4 NMR based toxicology: In vitro NMR metabolomics with the newly developed technique to study the impact of the anti-cancer drug bortezomib on 3D cell culture models of the thymic carcinoma cell lines 1889c and Ty82	79
3.4.1 Dose response curves for 2D and 3D cell cultures	79
3.4.2 Impact of bortezomib on the metabolite profiles of Ty82 cells and 1889c cells in 2D cell culture	82
3.4.3 Impact of bortezomib on the metabolite profiles of Ty82 cells and 1889c cells in 3D cell culture, measuring whole spheroids	86
4 Discussion	89
4.1 TET tissue metabolomics studies	89
4.1.1 General versus TET-specific metabolites	89
4.1.2 Metabolite profiles meet KEGG pathway activation and gene expression	91
4.1.3 Therapeutic perspectives	92
4.1.4 Conclusion	93
4.2 A new NMR technique for online metabolomics studies of 3D cell culture	93
4.2.1 Comparison of the technique to other approaches	93
4.2.2 Conclusion	95
4.3 New technique to prepare spheroids suitable for NMR	95
4.3.1 The rotation technique to produce spheroids	95
4.3.2 Conclusion	96
4.4 NMR toxicology: Bortezomib impact on 2D and 3D culture of thymic cell lines	96
4.4.1 Bortezomib as a drug against thymic malignancies?	96
4.4.2 Bortezomib impact detected with NMR metabolic profiling	97
4.4.3 Conclusions	98
4.5 Limitations of the study	98
5 Summary	100
6 References	101
7 CURRICULUM VITAE	113
8 ACKNOWLEDGMENT	115

LIST OF ABBREVIATIONS

ANOVA	Analysis of Variance
ERETIC	Electronic Reference to access in vivo Concentrations
GLUT	Glucose Transporter
GSEA	Gene Set Enrichment Analysis
HK	Hexokinase
HRMAS	High Resolution Magic Angle Spinning
IDH	Isocitrate Dehydrogenase
KEGG	Kyoto encyclopedia of Genes and Genomes
MG	Myasthenia Gravis
NMR	Nuclear Magnetic Resonance
PKM	Pyruvate Kinase
PYCR1	Pyrroline-5-Carboxylate Reductase
qRT-PCR	quantitative real time polymerase chain reaction
ROC	Receiver Operating Characteristic
ROS	Reactive Oxygen Species
sPLS-DA	Scarce Partially Least Squares Discriminant Analysis
TET	Thymic Epithelial Tumor
TC	Thymic Carcinoma
TCA	Tricarboxylic Acid
TCGA	The Cancer Genome Atlas
TSCC	Thymic Squamous Cell Carcinoma
MS	Mass spectrometry
FID	Free induction decay
FT	Fourier transform
Kel-F	Polychlorotrifluoroethylene
CPMG	Carr-Purcell-Meiboom-Gill
MALDI	Matrix-Assisted Laser Desorption/Ionization

LIST OF ABBREVIATIONS

2D	Two-dimensional
3D	Three-dimensional
BTZ	Bortezomib
TSP	3-(Trimethylsilyl)propionic-2,2,3,3-d ₄ acid
FGFb	Recombinant Human Fibroblast growth factor
DMEM	Dulbecco's Modified Eagle Medium
RPMI 1640	Roswell Park Memorial Institute
DPBS	Dulbecco's phosphate-buffered saline 1x
D ₂ O	Deuterium oxide
1889c	Thymic carcinoma cell line
Ty82	Thymic NUT carcinoma cell line
DIs	Disposable inserts
AUS	Area under the curve
PCA	Principal component analysis
v/v	volume/volume
N ₂	Nitrogen
SRT	Simple rotation technique
TMTS	Thymic Multicellular Tumor Spheroids
TTS	Thymic tumor spheroid
ECM	Extracellular matrix
DMSO	Dimethyl sulfoxide
EC	Effective Dose
ATP	Adenosine triphosphate
LSCM	Laser Scanning Confocal Microscopy
EthD-1	Ethidium homodimer
PFA	Paraformaldehyde
HCA	Hierarchical clustering analysis

LIST OF FIGURES

Figure 1.4.1.1 Signals in the time domain (t, left) and in the frequency domain (v, right) of NMR experiments, related to each other by the Fourier transform (FT).....	11
Figure 1.4.2.1 Schematic of a HR-MAS setup with a magic angle gradient.....	12
Figure 1.4.3.1 The tools and inserts used for HR-MAS NMR.....	13
Figure 1.4.4.1 Suppression of disturbing water signals.....	14
Figure 1.4.4.2 Suppression of disturbing macromolecule signals with a Carr-Purcell-Meiboom-Gill (CPMG) pulse sequence.....	15
Figure 1.5.1 Differences of metabolism of cells from the aerobic outer area and the hypoxic core of spheroids.....	18
Figure 2.2.2.4.1. Home-made N ₂ evaporation unit which helps to evaporate the methanol slowly prior to the freeze-drying step.....	37
Figure 2.2.2.7.2.. Formation of 3D cells with 3D Petri Dish®. A) Autoclaved mold with 2% agarose. B) Empty agarose mold. C) Equilibration of empty mold with fresh culture medium. D) Mold with spheroids (small white dots).....	39
Figure 2.2.2.8.1: Schematic representation of the 3D NMR measurement setup.....	42
Figure 1.2.2.8.3: Summarized NMR spectra and corresponding integrated intensity (blue curve) of a lithium lactate methyl resonance stepping the offset frequency by 25 Hz from -1.5 to 1.5 kHz using slice selective excitation.....	45
Figure 2.2.2.8.4 The slice selective sequence employed in this work. Slice selective pulses accompanied by a z-gradient (G _z) and the resulting FID signals are shown in blue.....	46
Figure 2.2.2.8.5: Model spheroid with a core diameter of 300 μm and an outer diameter of 700 μm, measurement slice and a path for which the intensity distribution has to be determined.....	47
Figure 2.2.3. Home-made sample holder for live cell imaging.....	50
Figure 3.1.1.1 Representative HRMAS ¹ H-NMR spectrum of a B2 thymoma measured at a tissue temperature of 4 °C and referenced to TSP.....	53
Figure 3.1.1.2 Boxplots showing the concentrations of the 37 metabolites found overall in thymomas (A, AB, B1, B2, B3, n=12), thymic carcinomas (TC, n=3) and normal thymi (NT, n=4).....	55

LIST OF FIGURES

- Figure 3.1.2.1 Heatmap with identified metabolites in thymic epithelial tumors (TETs): Hierarchical clustering analysis (HCA) was performed on 37 identified metabolites using Pearson correlation as the distance metric in 14 of the 15 TETs (1 A, 3 AB, 1 B1, 5 B2, 2 B3 thymomas and 3 thymic carcinomas, TC) and 4 non-neoplastic thymi (NT).....57
- Figure 3.1.3.1 Boxplots of the concentrations of metabolites, normalized to the sum of normal thymi (NT) in groups of clinically indolent thymomas (A, AB, B1 thymomas, group A, red; n=5) and aggressive thymic epithelial tumors (TETs) (B2 and B3 thymomas and TCs, group B, green, n=10).....58
- Figure 3.1.3.2 Receiver operating characteristic (ROC) curves for the metabolites cysteine, alanine, glutathione, creatine, inosine, alanine, lactic acid and myo-inositol, based on a grouping A= indolent thymomas and B=aggressive thymic epithelial tumors.....59
- Figure 3.1.5.1 Transcriptomic profiles of 7 representative genes selected from each of the 7 metabolic pathway determined in 57 thymic epithelial tumors (TETs: A, AB, B1, B2 and B3 thymomas and thymic carcinomas, TC) including the 15 thymic epithelial that were studied by HRMAS-¹H NMR.....61
- Figure 3.1.5.2 Transcriptomic profiles of 21 additional genes selected from the 7 metabolic pathways and determined in the 15 thymic epithelial tumors (TETs: A, AB, B1, B2 and B3 thymomas and thymic carcinomas, TC) that were studied by HRMAS-¹H NMR.....62
- Figure 3.2.1.1: Results from spatial resolved NMR experiments on a single Ty82 spheroid (diameter of 700 μ m) acquiring 24 slices (each slice measured for 4 h) up to a total time of 112 h, with the medium flow being stopped after 20 h.....67
- Figure 3.2.1.2 Light-microscopy images of three measured spheroids aligned to the spatial resolved intensity profiles of identified metabolites.....68
- Figure 3.2.1.3 Identification of viable cells (DAPI(+)) as compared to proliferative (Ki67(+)) cells in spheroids of different size generated from Ty82 NUT carcinoma cells.....70
- Figure 3.3.1.1 (Top) Images of Ty82 spheroids grown in serum-rich (TMTS) media. (Middle) Images of spheroids grown in serum-poor (TTS) media. (Bottom) Spheroid diameter of Ty82 cells as a function of seeding density, comparing growth in serum-rich (TMTS) and serum-poor (TTS) media and culture periods of 4, 8 and 12 days.....71
- Figure 3.3.1.2 Confocal microscopy image of untreated Ty82 spheroids (Serum poor/rich) stained with a combination of three dyes: 10 μ M Hoechst to visualize nuclei and nuclei fragmentation (Left), 2 μ M EthD-1 as a marker for dead cells (Middle left), 1 μ M calcein AM for viable cells (Middle right), and a merged image (Right). Images were taken using a Leica TCS SP8 DLS, and a maximum projection was applied to the 3D-stack with 1 μ m intervals. Scale bars represent 100 μ M.....72
- Figure 3.3.1.3 Characterization of 1889c (left) and Ty82 (right) spheroids using Ki67 (top row) and cleaved caspase-3 antibody (bottom row). Confocal microscopy fluorescence images are shown using DAPI to stain cellular nuclei (blue), Ki67 to stain the proliferating cells (green) and cleaved caspase-3 as an apoptotic marker (green).73

LIST OF FIGURES

- Figure 3.3.1.4 (Top) 1889c spheroids grown in microtissue molds, without matrigel, with seeding numbers of 1000, 8000 and 15000 cells. The combined use of microtissue molds and matrigel resulted in reproducible 3D models of 1889c cells that showed optimal growth (Middle) 1889c cells grown in microtissue molds and in the presence of various proportions of matrigel (5, 10, 15 and 20%) starting with 8000 seeding cells (Bottom) Comparison of spheroid formation and size in either the absence or presence of matrigel.....73,74
- Figure 3.3.1.5 Confocal microscopy image of untreated 1889c spheroids (Serum rich) stained with a combination of three dyes: 10 μ M Hoechst to visualize nuclei and nuclei fragmentation (Blue bottom Left), 2 μ M EthD-1 as a marker for dead cells (Red top right), 1 μ M calcein AM for viable cells (Green Top left), and a merged image (bottom right). Images were taken using a Leica TCS SP8 DLS, and a maximum projection was applied to the 3D-stack with 1 μ m intervals. Scale bars represent 100 μ M.....75
- Figure 3.3.1.6 A) Spheroidal growth of 1889c cells after 5, 6 and 8 days (from left to right) using Ultra Low Attachment plates. B) Spheroidal attachment to the bottom using normal plastic plates. C) Confocal imaging to check the viability of cells from the spheroid. Green reflects viable cells and red reflects dead cells.....76
- Figure 3.3.1.7 Removal of serum to induce spheroid formation reduces compactness of 1889c spheroids. Serum was highly important for 1889c (but not for Ty82) cells to form round shaped spheroids that are suitable for NMR measurements. For this reason TTS was excluded from subsequent experiments with 1889c cells.....77
- Figure 3.4.1.1 Dose response curves for bortezomib for the cell lines Ty82 (top row) and 1889c (bottom row) in 2D cell culture.....79
- Figure 3.4.1.2 Dose response curves for bortezomib for the cell lines Ty82 with 10% serum (top row), with 0.5% serum (middle row) and 1889c with 10% serum (bottom row) in 3D cell culture.....80
- Figure 3.4.2.1: NMR-based profiling revealed 45 metabolites in Ty82 cells grown in 2D culture, after bortezomib treatment.....82
- Figure 3.4.2.2: NMR-based profiling revealed 44 metabolites in the 1889c cell line in 2D culture after bortezomib treatment.....84
- Figure 3.4.3.1: Concentrations of 9 metabolites in a Ty82 spheroid.....86
- Figure 3.4.3.2: Concentrations of 9 metabolites in a 1889c spheroid.....87
- Figure 4.1.1.1 Venn diagram of the metabolite distribution in breast cancer, thymic epithelial tumors (TETs) (this study) and lung cancer.....90

LIST OF TABLES

Table 1.5.1: Comparative assessment of 2D and 3D cell culture properties.....	17,18
Table 2.1.1: List of Consumables.....	21,22
Table 2.1.2: List of equipment and instruments.....	21,22,23
Table 2.1.3: List of NMR chemicals, standards and consumables.....	24,25
Table 2.1.4: List of Software.....	25,26
Table 2.1.5: List of Media and buffers.....	26
Table 2.1.6: List of reagents, chemicals and antibodies.....	27,27
Table 2.1.7: Clinico-pathological characteristics of the 12 thymoma and 3 thymic carcinoma (TC) patients, as well as 4 controls (non-neoplastic thymuses, NT) studied here by HRMAS- ¹ H NMR spectroscopy.....	28
Table 2.1.8: The immortal human thymic carcinoma cell line, 1889 and the NUT carcinoma cell line, Ty82.....	29
Table 2.1.9.1: Primers for quantifying mRNA levels of 28 selected genes in the 15 snap-frozen thymic epithelial tumors that were studied by HRMAS- ¹ H NMR. GAPDH was used as housekeeping gene for qRT-PCR analysis.....	29,30
Table 2.1.9.2: Official full names of the 53 genes used for functional annotation clustering.....	30
Table 2.2.2.7.2: Spheroid size by number of cells seeded.....	41
Table 3.1.1.1: Metabolites detected in fifteen thymic epithelial tumors (TETs) using HRMAS ¹ H-NMR spectroscopy.....	55
Table 3.1.4.1: “KEGG metabolite-based metabolic pathways” identified by the MetPA algorithm using 37 metabolites detected in the indolent group A (A, B1 and AB thymoma subtypes) and aggressive group B (B2, B3 and TC) thymic epithelial tumors.....	61
Table 3.1.5.1 “KEGG transcriptome-based metabolic pathways” retrieved from the TCGA thymic epithelial tumor (TET) database (Radovich et al., 2018) applying the DAVID enrichment analysis tool to 53 genes with significantly (p<0.05) different expression between indolent group A (A1, AB, B1 thymomas) and aggressive group B TETs (B2, B3 thymomas; thymic carcinomas).....	65
Table 3.4.1.1: EC20, EC50 and EC80 values for bortezomib for the cell lines Ty82 and 1889c, both for 2D and 3D cell culture.....	82

1 Introduction

1.1 Thymus and thymic malignancies

The thymus (Miller, 2020) is an important lymphoid organ which is located in the anterior upper mediastinum, in front of the superior vena cava, on top of the heart and behind the sternum. The thymus is a primary lymphatic organ, where T-cell maturation takes place which is the result of a close symbiosis between thymocytes (= thymic lymphocytes) and a variety of thymic stromal cells, including thymic epithelial cells. Thymomas and thymic carcinomas (TCs) are rare thymic epithelial tumors (TETs) with an incidence of 2 to 4 cases per 1.000.000 people (Hsu et al., 2019). According to the WHO, thymomas are classified into type A, AB, B1, B2, B3 and rare other histological subtypes and are frequently associated with paraneoplastic syndromes like myasthenia gravis (Marx et al., 2013). TCs, on the other hand, have no thymus-like features and are biologically and histologically similar to carcinomas in organs other than the thymus (Kelly, 2013). TCs display the characteristics of aggressive epithelial tumors and are associated with autoimmune diseases only exceptionally (Kelly, 2013). According to histologic differences, TCs can be further subdivided into subtypes, the most common of which is thymic squamous cell carcinoma (Yang et al., 2020). Although all thymomas are nowadays considered malignant, type A, AB and B1 thymomas (“indolent TETs”) generally show low tumor stages and follow a more indolent clinical course (Tseng et al., 2017). Type B2 and B3 thymomas as well as thymic carcinomas (TCs) are generally aggressive cancers (“aggressive TETs”) (Marx, Belharazem et al., 2021). The molecular pathogenesis of thymomas and TCs is still poorly understood (Marx, Belharazem et al., 2021). A deep understanding of the molecular processes in tumor tissue would eventually offer new treatment options for aggressive thymomas and TCs with the potential to improve prognosis. The identification of new biomarkers may also help to support the development of more effective therapeutic strategies (J. Du & Zhou, 2017), which would be highly relevant for aggressive TETs that are currently not curable if not resectable. Among the potential biomarkers that have not been studied in TETs so far are metabolic signatures. Therefore, this thesis focused on the elucidation of metabolic features of aggressive as compared to indolent TETs.

1.2 Metabolomics

The approach of metabolomics, meaning the study of small molecules involved in metabolic pathways of living organisms, represents a valuable tool in the understanding of several diseases

(Ussher et al., 2016) including cancer (Gogiashvili et al., 2018a). Metabolites are organic small molecules with a molecular weight <1,500 Dalton that can act as substrates or products in biochemical metabolic cycles (Lazar & Birnbaum, 2012). Metabolites control cellular energy transfer and communication with other cells and may show substantial and often discontinuous changes in their types and concentrations as a response to pathological perturbations or drug treatments (AlWahsh et al., 2019; Mussap et al., 2018). Hence, metabolomics may assist in patients care by unveiling alterations in biochemical pathways involved in diseases and/or in drug administration (AlWahsh et al., 2019) (Mussap et al., 2018). Metabolomics allows for an integrated view on biochemistry of an organism, which marks the difference between the analysis of single metabolites and the study of the whole set of metabolites (“metabolic profile”) in a biological system via the investigation of biofluids, cells or tissue extracts (Rangel-Huerta et al., 2019). The metabolome can be seen as a highly dynamic molecular fingerprint of a biofluid or a tissue (Liang et al., 2015). The importance of studying the metabolome as a means to discover a set of metabolites as cancer biomarkers has been demonstrated (Henry & Hayes, 2012; Maruvada et al., 2005; Z. Song et al., 2019). The study of specific metabolites to identify cancer fingerprints or signatures can aid in cancer detection and prognosis as well as in the assessment of the pharmacodynamic effects of a drug based therapy. Knowledge about metabolite levels in human tumor tissue is required to quantitatively understand tumor metabolism (Johnson et al., 2016) and its relation to clinicopathological features of a given tumor (Gogiashvili et al., 2018a). Furthermore, metabolomics perfectly complements transcriptomics, genomics and proteomics in their potentials to analyze the physiological condition of a biological system.

1.3 Metabolic re-programming

Re-programming of cellular energy metabolism to support continuous cell growth and proliferation has emerged as a hallmark of many cancers (Hanahan & Weinberg, 2011; He et al., 2016). The approach of metabolomics, i.e. the study of a subset of small molecules derived from the global or targeted analysis of metabolic profiles from biological samples (Bingol, 2018) has the potential to become a valuable tool in the diagnosis and risk prediction in various diseases, including cancer, and can reveal even subtle abnormalities (L. Chen et al., 2018). Specifically, studies of metabolites to identify cancer fingerprints were helpful to elucidate new therapeutic targets such as CD147/EMMPRIN and CD44 in prostate cancer (Bruzzone et al., 2020; Putri et al., 2013; Zheng et al., 2020) and predict prognosis (Thurtle et al., 2019). The latter would be a major step forward for many patients with thymomas showing “aggressive

histotypes” but low tumor stages (e.g. B2 or B3 thymomas in stage pT1a/Masaoka-Koga stages IIa or IIb) (Radovich et al., 2018), in whom over- or undertreatment is a clinical issue, since it is currently unknown, which patients will profit from adjuvant radiotherapy (Girard et al., 2015). There is an increasing interest in biomarker-driven personalized cancer therapy (Lee & Hu, 2019; Trifonova et al., 2016). The development of molecular tests to detect biomarkers for the prediction of the outcome of targeted therapies has found growing interest (Min et al., 2017). The decision, on which therapy option to choose can be difficult, if tumors show more than one potential vulnerability (Lee & Hu, 2019). Biological markers (biomarkers) have been defined by Hulka and colleagues (Mueller, 1991) as “cellular, biochemical or molecular alterations that are measurable in biological media such as human tissues, cells, or fluids.” (Mueller, 1991). Later on, the definition has been broadened to include biological characteristics that can be objectively measured and evaluated as an indicator of normal biological processes, pathogenic processes, or pharmacological responses to a therapeutic intervention (Naylor, 2003). Biomarkers can be classified into four types: diagnostic, prognostic, predictive, and therapeutic. A diagnostic biomarker allows the early detection of a cancer in a noninvasive way and thus secondary cancer prevention. A predictive biomarker serves to foresee the response of a patient to a targeted therapy and helps to define subpopulations of patients that will most probably show a response to a specific therapy. A prognostic biomarker provides information on the likely course of the disease and gives a hint to therapeutic results (Italiano, 2011; Lin et al., 2012; Xue et al., 2019). A therapeutic biomarker is generally a protein that could be used as target for a therapy (Lin et al., 2012). Recently, nuclear magnetic resonance spectroscopy (NMR)-based metabolomics analysis (Z. Song et al., 2019) and multivariate statistical techniques have been incorporated into a multidisciplinary approach to profile changes in small molecules associated with the onset and progression of human diseases. The purpose of these efforts is to identify unique metabolite biomarkers in a specific human disease so as to (1) accurately predict and diagnose diseases, including separating distinct disease stages; (2) analyze the pathways of pathogenesis as well as disease progression and (3) help in therapy and therapy efficacy evaluation (Z. Song et al., 2019).

1.4 Nuclear Magnetic Resonance Spectroscopy techniques employed for metabolic studies

The two most successful detection methods used for the metabolomics analysis of tumor tissue are nuclear magnetic resonance (NMR) and mass spectrometry (MS). Although the higher sensitivity of MS facilitates the quantification of a higher number of metabolites as compared to NMR, certain characteristics of NMR make this method indispensable in metabolomics

(Beckonert et al., 2007) (Bingol & Brüscheiler, 2014). NMR can be used to analyze hundreds of small molecules simultaneously and efficiently in human samples including blood, serum and metabolite extracts. Moreover, high resolution (HR) magic angle spinning (MAS) nuclear magnetic resonance spectroscopy (Gogiashvili et al., 2019) offers the unique possibility to determine metabolite concentrations in intact human cancer tissue specimens, delivering quantitative information for approximately 40 metabolites without major manipulation of the tissue samples prior to NMR analyses (Keun, 2014). Furthermore, the method is non-destructive, offering the possibility of subsequent (post-NMR) investigations (e.g. of transcriptomic analyses) of the *same* specimen (Gogiashvili et al., 2019). Because of these advantages, NMR was considered the most appropriate analytical technique for metabolomics studies of thymic tissues.

1.4.1 The Signals of Nuclear Magnetic Resonance

NMR active nuclei must have a magnetic moment, which is associated with a nuclear spin. In contrast to a classical magnetic moment, the nuclear moment can take just certain orientations with respect to the external field, as it follows the rules of quantum physics. In the case of the hydrogen (^1H) nucleus there is an orientation parallel and antiparallel to the external magnetic field B_0 , which correspond to different energies, with the higher energy level being associated with the antiparallel orientation. According to the Boltzmann distribution, there are more moments in the lower energy state than in the higher one. In a magnetic field of 14.1 T this corresponds to 10.000 moments in the higher state and 10001 moments in the lower state. The energy difference, like in other spectroscopies, can be overcome by an absorption of electromagnetic radiation. The sum of all the magnetic moments in the sample results in a net magnetization vector in the direction of the B_0 field. An electromagnetic pulse, when applied to the sample, rotates the sum magnetization vector from the B_0 direction to an axis perpendicular to the B_0 direction. This tilted “transverse” magnetization gives a signal in the receiver coil. The magnetization is, however, not stable and decays exponentially. For this reason, the signal delivered by the receiver coil sampled as a function of time shows the characteristic exponential decay pattern of a “free induction decay” (FID), see Figure 1.4.1.1. After calculating a Fourier transformation of the time domain data the NMR spectrum is obtained.

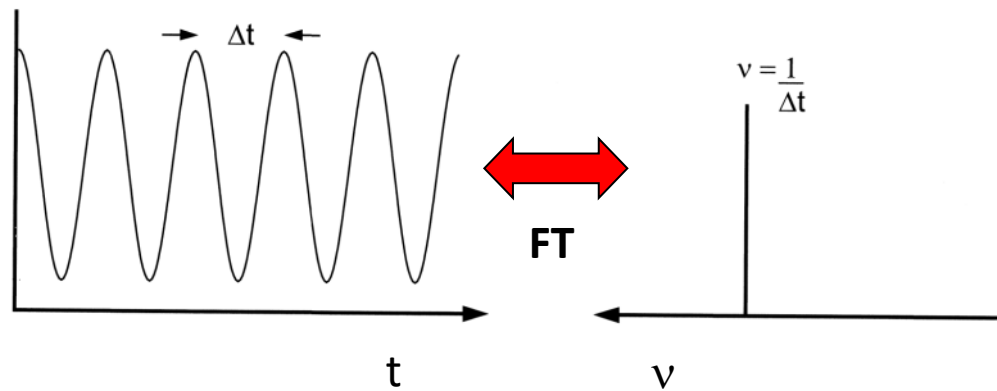


Figure 1.4.1.1 Signals in the time domain (t, left) and in the frequency domain (v, right) of NMR experiments, related to each other by the Fourier transform (FT).

1.4.2 High Resolution Magic Angle Spinning (MAS)-NMR spectroscopy for metabolic profiling of intact tissues

While the NMR technique as explained so far gives well resolved signals in liquid samples, the observation of metabolites within intact tissue results in poorly resolved signals due to line broadening effects like dipolar coupling and chemical shift anisotropy that occur in (semi)solid materials. These line broadening effects can be removed, however, if during the measurement the sample is spun at the magic angle $\theta = 54.7^\circ$ (Figure 1.4.2.1) (Tilgner et al., 2019). Here θ is the angle between the sample tube and the B_0 field (Figure 1.4.2.1). The spinning rate has to be chosen comparable to the NMR line width that would occur if the sample was measured under static conditions. However, in order not to generate spinning sidebands, the spinning rate has to be chosen even higher, namely 5 kHz (Gogiashvili et al., 2019).

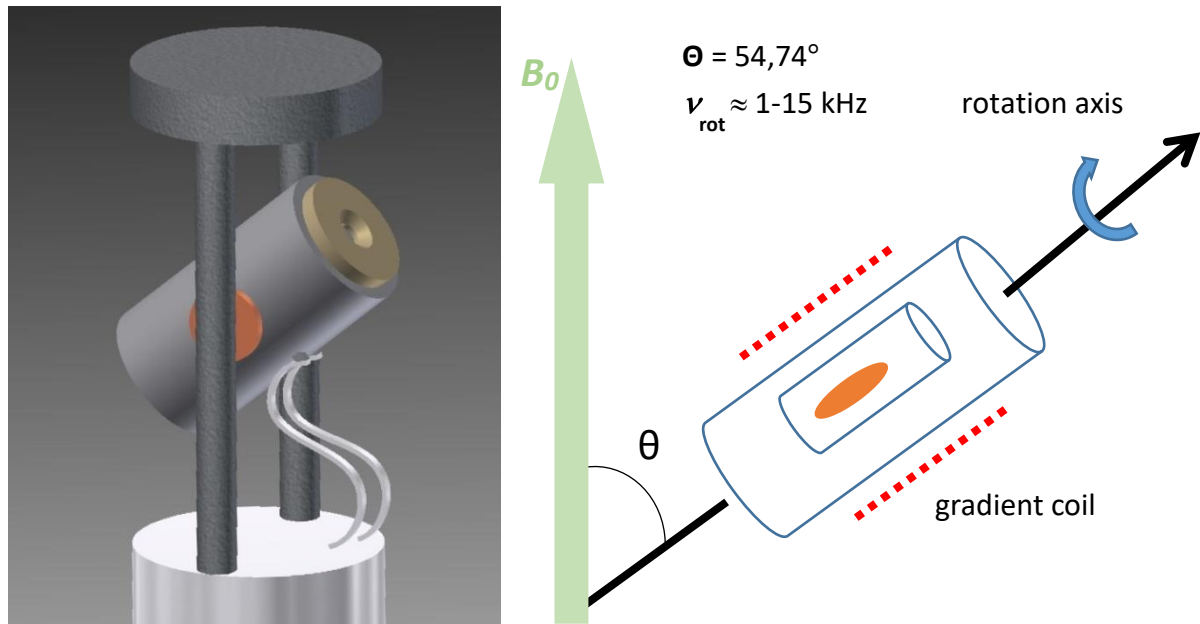


Figure 1.4.2.1 Schematic of a HR-MAS setup with a magic angle gradient (Reprinted from *Metabolites* 2019, 9, 19-45, doi:10.3390/metabo9020019, Publication Date: January 22, 2019).

1.4.3 The tools and inserts used in HR-MAS-NMR spectroscopy

Samples in HR MAS NMR have to be filled into a rotor, see Figure 1.4.3.1. To avoid loss of liquid during the fast sample rotation for the semisolid tissue samples, various types of inserts are commercially available for HR-MAS samples, e.g. the disposable insert (Figure 1.4.3.1). This is a small Kel-F container (Which is a polychlorotrifluoroethylene with dimensional stability) , which holds the tissue sample and can be closed tightly with a screw (Figure 1.4.3.1).

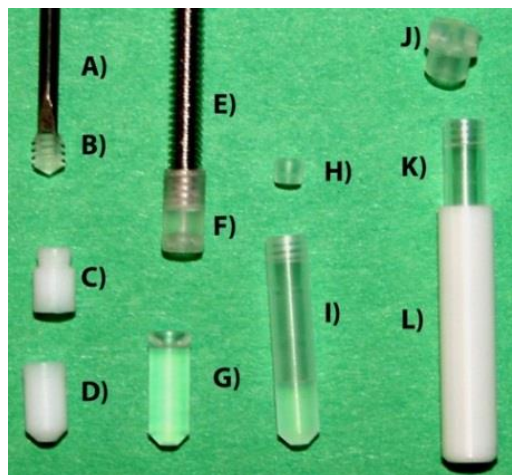


Figure 1.4.3.1 The tools and inserts used for HR-MAS NMR (Source: Alam and Jenkins, 2012). A) the specialized tool for screw cap insertion, B) the sealing screw cap, C) the upper Teflon insert, D) lower Teflon insert for 30µL volume, E) screw for insertion of the top insert. F) Top Kel-F insert, G) bottom Kel-F insert of the cap, H) plug for disposable insert, I) disposable 30µL Kel-F insert, J) rotor cap, K) disposable insert introduced partially in a 4 mm rotor, L) 4 mm zirconia MAS Rotor. All these parts are provided by the BRUKER HR-MAS system.

1.4.4 NMR measurement techniques

Water is a dominating component of biological samples and the strong ^1H -NMR signal of it exceeds the metabolite signals by several orders of magnitude. If not suppressed, it impedes a correct quantification of the latter. The ^1H -NMR spectrum of a sample with high water content is displayed in Figure 1.4.4.1a. Figure 1.4.4.1b shows a spectrum of the same sample with water suppression using a so called “presaturation pulse”, which reduces the intensity of the water signal to the same level as the metabolite signal intensities (Figure 1.4.4.1c) (Hwang & Shaka, 1995). In this way, the quantification of the metabolite signals is possible.

Introduction

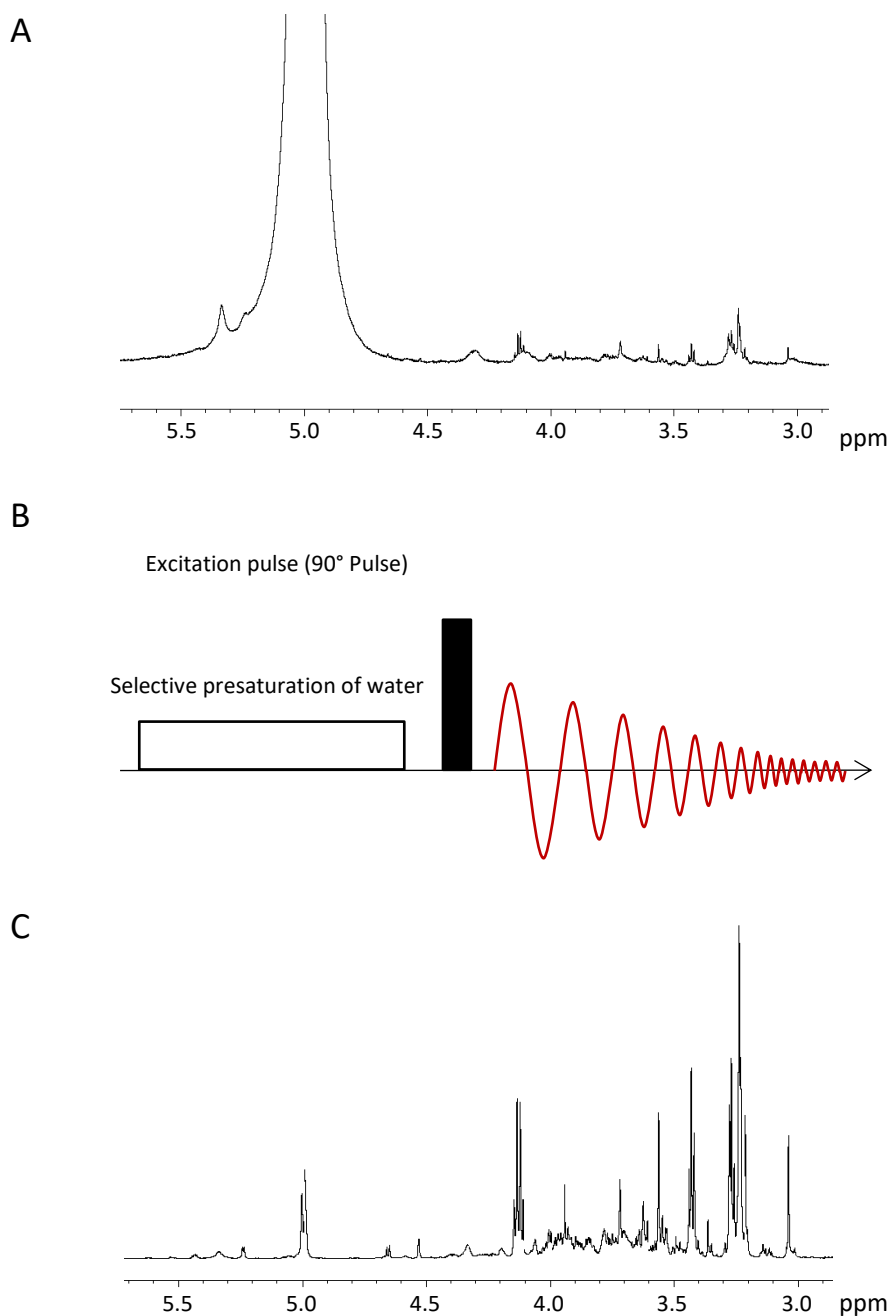


Figure 1.4.4.1 Suppression of disturbing water signals: (A) ^1H NMR spectrum of a tumor sample without water suppression. The strong water signal impedes the correct quantification of the metabolite signals. (B) Presaturation pulse for water signal suppression. (C) ^1H NMR spectrum of a cancer tissue sample with a completely suppressed water signal, allowing for a straightforward quantification of the metabolite signals of the sample (Reprinted from *Metabolites* 2019, 9, 19-45, doi:10.3390/metabo9020019, Publication Date: January 22, 2019).

Using HR-MAS NMR to analyze cancer tissue, the broad lipid signals must be removed to acquire a high resolution spectrum that allows the detection and quantification of metabolites.

Introduction

Suppression of the lipid signals is commonly performed with a spin-echo Carr-Purcell-Meiboom-Gill (CPMG) pulse sequence (Bliziotis et al., 2020) (Figure 1.4.4.2).

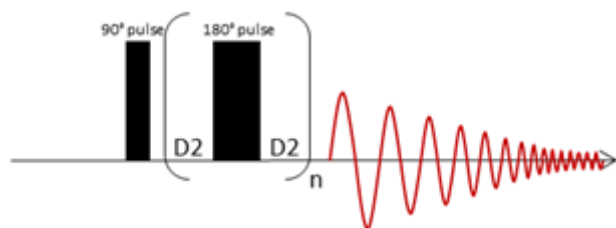


Figure 1.4.4.2 Suppression of disturbing macromolecule signals by CPMG pulse sequence: The sample is excited with a 90° pulse, followed by a sequence of n 180° pulses, each pulse bracketed by two delay times $D2$, in which no pulse is acting on the sample. Subsequently, the signal is recorded. The total delay time $n \cdot 2 \cdot D2$ is chosen so as to suppress the signals of macromolecules like lipids and proteins, but leaves the signal of metabolites unaffected (Reprinted from *Metabolites* 2019, 9, 19-45, doi:10.3390/metabo9020019, Publication Date: January 22, 2019).

For metabolomics studies on 3D cell cultures, extraction techniques that have been well established for 2D cell models have been employed so far. Unfortunately, the extraction of metabolites not only effects metabolic concentrations, but fails to preserve any spatial information on the metabolite concentrations, which is highly valuable information when characterizing the cells' response to drugs. There are approaches to set up a spatial resolved metabolomics using Matrix-Assisted Laser Desorption/Ionization (MALDI) MS (Machálková et al., 2019), but this method just provides a “snap-shot” of an anticipated time point and is destructive. NMR as a noninvasive technique is much better suited for the investigation of living spheroids and the detection of their metabolites, but conventional NMR techniques fail due to the small sample size and the low metabolite concentrations. Hence a measurement technique has to be developed first, that is suitable for ultra-small volumes and concentrations of bio-medical samples enabling to deal with the special ultra-low concentrations of spheroid metabolites. Moreover, a special microfluidic cell has to be developed to ensure both the viability of the living cells and to serve as an NMR sample holder. The setup of a customized NMR technique to record ^1H -NMR signals of 3D tumor models is one of the aims of this thesis.

1.4.5 Cryogenic NMR

Introduction

To run measurements on cell culture samples with the highest possible sensitivity, the technique of cryogenic NMR (Kovacs & Moskau, 2013) is employed: Helium gas is compressed and fed into a closed cycle chiller, where it undergoes thermal expansion, and cools down to 20 K.. The gas is then used to cool the coils and the preamplifier to 20 K. The sample is thermally isolated from the cryogenic circuit by a high vacuum chamber. As a result the sample and the magnet are kept at room temperature, while the electronic noise sensitive parts of the NMR detection system are at 20 K, in this way reducing the noise level of the NMR measurements and increasing the sensitivity.

1.5 Cell culture

Ex vivo two-dimensional (2D) tumor cell cultures and cell lines grown in 2D are known to only partially reflect tumor biology in vivo, making the “translation” of findings (e.g. drug sensitivity test) to (pre-)clinical testing problematic. Lack of the tumor microenvironment and non-physiological growth in 2D in conventional in vitro cultures are major reasons for this (Jensen & Teng, 2020).

The rare occurrence of thymoma and thymic carcinoma renders finding a good model for drug test and validation prior to in-vivo based testing an important issue. Therefore, I developed a three dimensional (3D) cell culture model (Russell et al., 2017), while the majority of cancer drug studies still uses a 2D culture format measuring proliferation, growth, viability, and apoptosis. However, 3D models have been shown to be a better mimic of a large number of tissue features than 2D model, including mechanical impacts, structural organization, communication between tumor cells and the extracellular matrix, as well as gas, nutrition and waste product gradients (Russell et al., 2017) (Table 1.5.1). More importantly, some 3D tumor models proved more relevant in terms of drug susceptibility and resistance mechanisms than 2D cultures (Zaal & Berkers, 2018). One important feature of some 3D models is the oxygen depleted core (Figure 1.5.1), caused by limited oxygen diffusion, leading to an anaerobic metabolism of glucose to lactic acid and ultimately to an decreased pH-value (Roy & Finley, 2019) and cell dormancy. The hypoxic cells found in the core area of spheroids are of major interest here, since hypoxia has been found to be the basis of drug resistance in many cancers (J.-Q. Li et al., 2017).

In technical terms, scaffold-less formed cell spheroids are among the most frequently used 3D models, as they can be produced in large quantities employing ultra-low-attachment (ULA) round-bottom microplates (Vinci et al., 2012) and hanging drop techniques (Kelm et al., 2003).

Introduction

Because of these advantages, spheroids were studied here as a 3D model, since the establishments of organoids as likely even more “physiological” 3D model has not been achieved so far.

Table 1.5.1 Comparative assessment of 2D and 3D cell culture properties (Reprinted with permission from: Farhat, J.; Pandey, I.; AlWahsh, M. Transcending toward Advanced 3D-Cell Culture Modalities: A Review about an Emerging Paradigm in Translational Oncology. Cells 2021, 10, 1657. doi: 10.3390/cells10071657).

Main properties	2D cell culture	3D cell culture
Cell morphology	<ul style="list-style-type: none"> • Cells grow as a flat and elongated 2 dimensional monolayer on petri plates or flasks 	<ul style="list-style-type: none"> • Cells grow as 3D spheroids within multiple layers
Cell microenvironmet	<ul style="list-style-type: none"> • Equal quantity of nutrients and growth factors received by all cells • Majority of cells are in the same cell cycle • Absence of in-vivo like environment 	<ul style="list-style-type: none"> • Variable quantity of nutrients are ingested by cells based on the cell cycle • Mimic an in-vivo cell mechanism
Cell interaction	<ul style="list-style-type: none"> • Coordination between cells is limited 	<ul style="list-style-type: none"> • Cell-cell interaction is active
Cell proliferation	<ul style="list-style-type: none"> • Irregularly rapid intensity 	<ul style="list-style-type: none"> • Gradual and balanced
Drug response	<ul style="list-style-type: none"> • Cellular resistance is not well expressed • Drug Pharmacodynamic/ Pharmacokinetic mechanisms are not 	<ul style="list-style-type: none"> • Drug- dose response is well studied as it is more likely to matches the in vivo resistance

well studied

Molecular mechanisms	<ul style="list-style-type: none"> • Variable gene / protein expression, mRNA splicing and cells biochemistry 	<ul style="list-style-type: none"> • Expressed genes, proteins, mRNA and other cells processes are well assessed and measured
Response to extrinsic stimuli	<ul style="list-style-type: none"> • Not a valid reflection of the biological cell response • Unable to respond to gravity since their inability to evolve into a 3D cell 	<ul style="list-style-type: none"> • Effective reflection of the intrinsic response • Constantly able to respond to gravity since they can formulate their 3D cells

One important feature of spheroids is the oxygen depleted core (Figure 1.5.1), caused by limited oxygen diffusion through the cell layers, leading to an anaerobic metabolism of glucose to lactic acid and ultimately to an increased pH-value and cell dormancy. Especially for cancer research, the hypoxic cells found in the core area of spheroids are of major interest, since they possess an increased resistance against several anti-cancer drug classes.

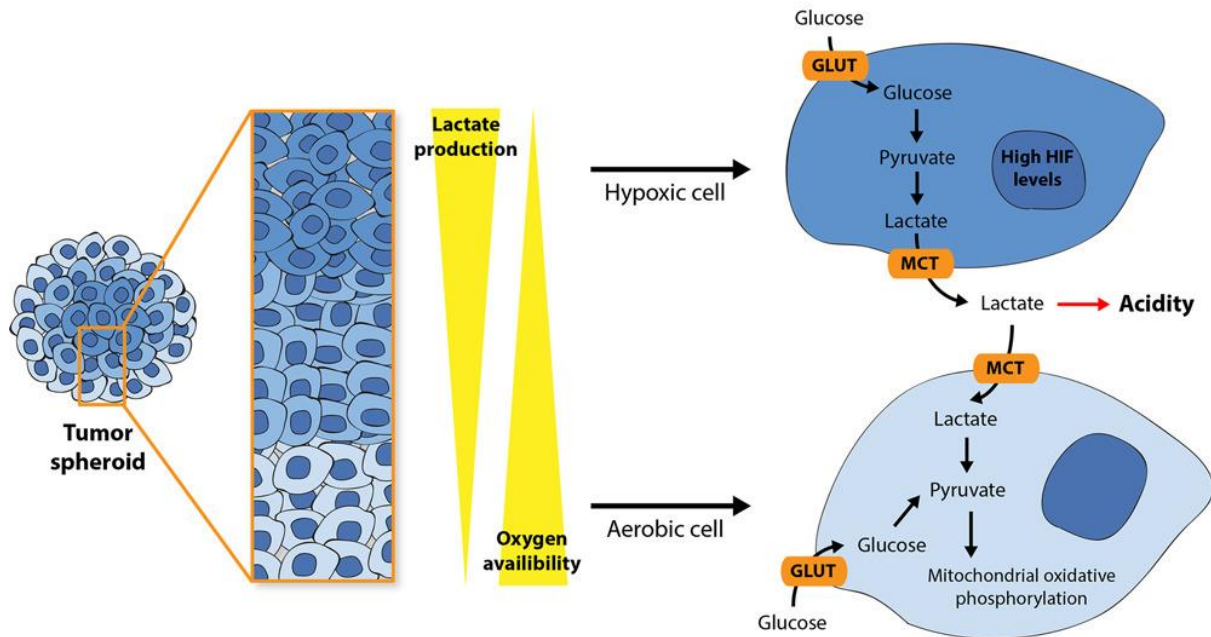


Figure 1.5.1 Differences of metabolism of cells from the aerobic outer area and the hypoxic core of spheroids (Source: Nunes, Barros, Costa, Moreira & Correia, 2018)

1.6 Bortezomib (BTZ)

Prior to the start of this thesis, Dr. D. Belharazem and Prof. A. Marx had discovered that neoplastic thymic epithelial cells show a vulnerability towards the classical proteasome inhibitor, Bortezomib (manuscript in preparation), however, without metabolomics readouts. Therefore, this thesis addressed the question, which impact Bortezomib might have on the metabolite profiles of the two thymic carcinoma cell lines, Ty82 and 1889c. Proteasome inhibition is known as a strategy to generate an imbalance between the production and degradation of proteins in cancer cells, which can result in apoptosis of the malignant cells via overproduction of ROS (Obeng et al., 2006) (N. Anderson et al., 2018; Moreau et al., 2012). Bortezomib (PS-341) is a potent proteasome inhibitor that targets the ubiquitin-proteasome pathway (Davies et al., 2007). Bortezomib is approved by the Food and Drug Administration for the treatment of multiple myeloma and mantle cell lymphoma (Dooley & Anderson, 2016). Because oxidative stress plays a role in the mechanism of action of bortezomib and is commonplace in cancer cells, an anticancer efficiency of bortezomib is also found in other cancers, like e.g. hematologic malignancies (Niewerth et al., 2015), where early phase clinical studies have demonstrated tolerability and activity in a variety of cases. By its mechanism of inhibiting protein degradation, bortezomib targets a wide range of pathways that are relevant to

tumor progression and therapy resistance and can directly modulate expression of cyclins, p53, NF- κ B, Bcl-2, and Bax (Adams, 2002). Although bortezomib has shown its greatest benefit in the treatment of multiple myeloma, it targets many key cell cycle regulators that are relevant to tumor progression and therapy resistance in solid tumors like lung cancer (Orlowski et al., 2007). For an unresectable stage III thymic cancer it has been reported (Dooley & Anderson, 2016) that a combination of intensity modulated radiation therapy and bortezomib treatment, continued also post-radiation, appears to be a useful definitive treatment option for unresectable thymic carcinoma tumors. However, the metabolic consequences of bortezomib applied to thymic malignancies have remained enigmatic.

1.7 Aims of the study

From the above discussion of gaps of knowledge concerning the metabolism of native and treated thymic epithelial tumors, the following aims of this study were deduced:

- 1) Tissue metabolomics of thymic epithelial tumors (TETs): To identify altered metabolic signatures in aggressive TETs in order to open new targeted therapeutic options for non-resectable thymomas and thymic carcinomas.
- 2) Investigation of the metabolism of a 3D cell culture model with time and spatial resolution under viable conditions: Application of a new flow NMR technique
Production of 3D cell culture with two new techniques and characterization of the spheroids obtained
- 3) Production of 3D cell culture with two new techniques and characterization of the spheroids obtained
- 4) NMR based toxicology: In vitro NMR metabolomics with the newly developed technique to study the impact of the anti-cancer drug bortezomib on 3D cell culture models of the thymic carcinoma cell lines, 1889c and Ty82

2 MATERIAL AND METHODS

2.1 Material

2.1.1 Consumables

Table 2.1.1: List of Consumables

Cell culture black microplates, 96 wells	Greiner Bio-One, Frickenhausen, Germany
Cryopreservation tubes (Cryo.s™)	Greiner Bio-One, Frickenhausen, Germany
Costar® 96 well plate, Ultra-Low attachment surface	CORNING Life Sciences, Kennebunk, ME, USA
Costar® 24 well plate, Ultra-Low attachment surface	CORNING Life Sciences, Kennebunk, ME, USA
Costar® 6 well plate, Ultra-Low attachment surface	CORNING Life Sciences, Kennebunk, ME, USA
Pipette TIPS (0.1, 1, 2, 5 ml)	Eppendorf, Hamburg, Germany
Pipette TIPS (10, 200, 1000 µl)	Eppendorf, Hamburg, Germany
Pipettes (10, 100, 200, 1000 µl)	Eppendorf, Hamburg, Germany
Serological pipettes (5, 10, 25, 50 ml)	Eppendorf, Hamburg, Germany
Mr. Frosty™	Thermo Fisher Scientific, Waltham, MA, USA
6 well plates	Sarstedt, Nümbrecht, Germany
12 well plates	Sarstedt, Nümbrecht, Germany
24 well plates	Sarstedt, Nümbrecht, Germany

MATERIAL AND METHODS

96 well plates	Sarstedt, Nümbrecht, Germany
Falcon™ tubes (15, 50ml)	Sarstedt, Nümbrecht, Germany
Multichannel pipette	Eppendorf, Hamburg, Germany
C-Chip disposable hemocytometers	NanoEnTek, Waltham, USA
MicroTissues 3D Petri Dish® 9x9 array	Sigma-aldrich, St. Louis, USA
Low binding micro tubes (0.5,1.5, 2ml)	Sarstedt, Nümbrecht, Germany
Cell culture T-75 Flasks, red filter cap	Sarstedt, Nümbrecht, Germany
Cell culture T-25 Flasks, white filter cap	Sarstedt, Nümbrecht, Germany
Multichannel pipette	Eppendorf, Hamburg, Germany
Eppendorf conical tubes 15 and 50ml, amber	Eppendorf, Hamburg, Germany
Glass pasteur pipettes	Brand, Werheim, Germany
SuperFrost Plus™	Thermoscientific, Braunschweig, Germany

2.1.2 Equipment

Table 2.1.2: List of equipment and instruments

Nuclear magnetic resonance spectroscopy Ascend™ 600MHz	Bruker, Fällanden, Switzerland
High sensitivity CryoProbe	Bruker, Fällanden, Switzerland
High-resolution magic angle spinning probe (HR-MAS)	Bruker, Fällanden, Switzerland
ARE/AREX-6 Series hot plate stirrers	VELP Scientifica Srl, Usmate Velate MB, Italy

MATERIAL AND METHODS

ISMATEC® reglo ICC	ISMATEC®, Weinheim, Germany
SONOREX SUPER RK 100 H	BANDELIN electronic GmbH & Co KG, Berlin, Germany
IKA® RCT basic IKAMAG™	IKA-Werke GmbH & Co. KG, Staufen, Germany
Eppendorf, Centrifuge 5702	Eppendorf, Hamburg, Germany
Eppendorf, Centrifuge 5430 R	Eppendorf, Hamburg, Germany
Eppendorf, Centrifuge 5424 R	Eppendorf, Hamburg, Germany
ALLEGRA X-15R	Beckman Coulter, Brea, CA, USA
Alpha 2-4 LSC basic	Christ, Osterode am Harz, Germany
Ultra-Low Temperature Freezer MDF-U700VX	Panasonic, Gunma, Japan
Leica TCS SP8 DLS Digital Light sheet and Confocal Microscope	Leica, Wetzlar, Germany
The Cube Microscope Temperature Control System	LIFE IMAGING SERVICES, Basel, Switzerland
The brick Gas Mixer CO ₂ controller	LIFE IMAGING SERVICES, Basel, Switzerland
KERN 770	KERN & Sohn GmbH, Balingen, Germany
Steri-Cycle CO ₂ incubator HEPA class 100	Thermo Fisher Scientific, Langenselbold, Germany
Autoclave Sturdy SA-260MA class B	HMC Europe GmbH, Tüßling, Germany
Nikon microscope Eclipse TE300	Nikon, Tokyo, Japan

MATERIAL AND METHODS

Miniature Shaker KM for CO ₂ Incubators	Edmund Bühler GmbH, Bodelshausen, Germany
Tecan Spark 20M plate reader	TECAN, Crailsheim, Germany
CB 170(E7) Incubator	Binder GmbH, Tuttlingen, Germany
Janke & Kunkel IKA Labortechnik VF2	IKA-Werke GmbH & Co. KG, Staufen, Germany
Multishaker platform	NeoLab, Heidelberg, Germany
DFK 33UX174 microscope camera	The Imaging Source Europe GmbH, Bremen, Germany

2.1.3 NMR chemicals, standards and consumables

Table 2.1.3: List of NMR chemicals, standards and consumables

3-(Trimethylsilyl)propionic-2,2,3,3-d ₄ acid sodium salt (TSP)	Sigma-aldrich, St. Louis, MO, USA
Deuterium oxide (D ₂ O)	Sigma-aldrich, St. Louis, MO, USA
NMR tubes Boro600-5-8	Deutero, Kastellaun, Germany
Disposable Biopsy Punch	PFM Medical, Köln, Germany
MAS rotor kit	Bruker, Rheinstetten, Switzerland
Sucrose	Sigma-aldrich, St. Louis, MO, USA
Glass capillaries 1423057, 1423060	Hilgenberg, Malsfeld, Germany
PTEF-tubes	Chromatographie Service GmbH, Langerwehe, Germany

MATERIAL AND METHODS

5ml Henke-ject®	Henke-Sass, Wolf GmbH, Tuttlingen, Germany
2-Way vlv Bio w/ 1/16in Ftgs and Ferrules	IDEX Health & Science, Lake Forest, IL, USA
Microcapillary tube Drummond Microcaps® (1,2 and 10 µl)	Sigma-aldrich, St. Louis, MO, USA
Needles	B.Braun, Melsungen, Germany

2.1.4 Software

Table 2.1.4: List of Software

Image J	https://imagej.net
Graphpad Prism V6.0	GraphPad Software, La Jolla, CA, USA (www.graphpad.com)
Chenomx	Chenomx Inc., Edmonton, Alberta, Canada
Topspin	Bruker BioSpin, Karlsruhe, Germany
LasX	Leica, Wetzlar, Germany
MetaboAnalyst	University of Alberta (https://www.metaboanalyst.ca/)
IC Measure capture 2.0.0.133 software	The Imaging Source Europe GmbH, Bremen, Germany
PAN cancer atlas	NIH, Bethesda, ML, USA
CBioPortal	http://www.cbioportal.org/

MATERIAL AND METHODS

Microsoft PowerPoint software	Microsoft, Redmond, WA, USA
Microsoft Word software	Microsoft, Redmond, WA, USA

2.1.5 Media and buffers

Table 2.1.5: List of Media and buffers

Dulbecco's Modified Eagle Medium (DMEM)	Gibco, Paisley, UK
Roswell Park Memorial Institute (RPMI 1640)	Gibco, Paisley, UK
Dulbecco's phosphate-buffered saline 1x (DPBS)	PAN biotech, Aidenbach, Germany
Fetal Bovine Serum (FBS)	Sigma-aldrich, St. Louis, MO, USA
HEPES	Gibco, Paisley, UK
Trypsin-EDTA (0.05%)	PAN biotech, Aidenbach, Germany
Pen Strep	Sigma-aldrich, St. Louis, MO, USA

2.1.6 Chemicals and reagents

Table 2.1.6: List of reagents, chemicals and antibodies

Bortezomib 10 and 25mg	Cayman Chemical, Ann Arbor, MI, USA
CellTiter-Glo luminescent cell viability assay	Promega, Fitchburg, WI, USA
Matrigel® Matrix Basement Membrane	CORNING Life Sciences, Kennebunk, ME, USA
25KU Heparin sodium salt from porcine intestinal mucosa	Sigma-aldrich, St. Louis, MO, USA

MATERIAL AND METHODS

Recombinant Human Fibroblast growth factor (FGFb)	Life technologies, Carlsbad, CA, USA
EGF, recombinant Epidermal growth factor	Sigma-aldrich, St. Louis, MO, USA
ROTHistol	Carl Roth, Karlsruhe, Germany
Ethanol	VWR, Darmstadt, Germany
Calcein-AM	Sigma-aldrich, St. Louis, MO, USA
Ethidium Homodimer	Sigma-aldrich, St. Louis, MO, USA
Hoechst 33342	Abcam, Cambridge, United Kingdom
B-27™ Supplement (50X)	Gibco, Paisley, UK
Donkey serum (Blocking buffer)	Sigma-aldrich, St. Louis, MO, USA
Extracellular matrix proteins	Sigma-aldrich, St. Louis, MO, USA
Citrate buffer	Sigma-aldrich, St. Louis, MO, USA
Hydrocortisone	Sigma-aldrich, St. Louis, MO, USA
Trypan Blue solution	Sigma-aldrich, St. Louis, MO, USA
UltraPure™ Agarose	Life technologies, Carlsbad, California, USA
Cleaved Caspase-3 (Asp175) (D3E9) Rabbit mAb (Alexa Fluor® 488 Conjugate)	Cell signaling technology , Danvers, MA, USA
Ki-67 (D3B5) Rabbit mAb (Alexa Fluor® 488 Conjugate)	Cell signaling technology, Danvers, MA, USA
Isopropanol	Sigma-aldrich, St. Louis, MO, USA
Methanol	Sigma-aldrich, St. Louis, MO, USA
DAKO grease pencil	Agilent, Santa Clara, CA, USA

2.1.7 Patients and Tissue Samples

Patient characteristics are summarized in Table (2.1.7). Samples were worked-up and classified according to WHO criteria [1] by two expert pathologists. Where appropriate, WHO thymomas were grouped as indolent thymomas (ITETs - group A: A, AB and B1 thymomas) or aggressive TETs (ATETS - group B: B2 and B3 thymomas as well as TCs). The study was approved by the local Ethics Committee (approval #2009-290N-MA/2010) at the Medical Research Center, Medical Faculty Mannheim, Heidelberg University, Mannheim, Germany and by the ethics committee of the Leibniz-Institut für Analytische Wissenschaften - ISAS - e.V., Dortmund, Germany.

Table 2.1.7 Clinico-pathological characteristics of the 12 thymoma and 3 thymic carcinoma (TC) patients, as well as 4 controls (non-neoplastic thymuses, NT) studied here by HRMAS-¹H NMR spectroscopy. The classification of thymomas (type A, AB, B1, B2, and B3) and TC followed the World Health Organization (WHO) (Travis et al., 2015). MG+ (%): percentage of patients with Myasthenia gravis; N: number of cases; nk: not known; Stage according to Masaoka-Koga (Detterbeck et al., 2011) (Part of these results were recently submitted for publication in *CANCERS*.)

Diagnosis	N	Age (years)	Sex (M/F)	Stage (I-IV)
Type A	1	77	M	n.k.
Type AB	3	46	M	II, R0
		65	M	II, R0
		77	M	IIb, R0
Type B1	1	72	M	III
Type B2	5	75	F	III, R0
		73	F	IIIb, R1
		51	M	IVa, R0
		73	F	III, RX
		72	F	Iva R0
Type B3	2	80	F	I, R0
		58	M	II, R
TC	3	75	M	III
		69	M	II
		78	M	II
NT	4	27	M	
		42	M*	
		39	F*	
		20	F*	

* Non-neoplastic thymuses with mild thymitis (lymphofollicular hyperplasia)

2.1.8 Cell lines

Table 2.1.8.: The immortal human thymic carcinoma cell line, 1889 and the NUT carcinoma cell line, Ty82 were provided by Prof. Dr. med. Alexander Marx, University Medical Centre Mannheim, Heidelberg University.

Cell line	Cell type
1889c	Thymic carcinoma cell line ^a
Ty82	Thymic NUT carcinoma cell line ^b

^a (Ehemann et al., 2008)

^b (Kuzume et al., 1992)

2.1.9 Primers

Table 2.1.9.1: Primers for quantifying mRNA levels of 28 selected genes in the 15 snap-frozen thymic epithelial tumors that were studied by HRMAS-¹H NMR. GAPDH was used as housekeeping gene for qRT-PCR analysis (Part of these results were recently submitted for publication in *CANCERS*.).

Gene Name	Primer Forward	Primer reverse
HK1	AATGCTGGGAAACAAAGGT	AGAGGAATCCCTTCTTGGG
HK3	GTGGCATTTCATGGAATGGG	AACCCTTGGTCCAGTTCAGG
PDK1	CTGTGATACGGATCAGAAACCG	TCCACCAAACAATAAAGAGTGCT
PKM	CCATTACCAGCGACCCACAG	GGGCACGTGGGCGGTATCT
SLC2A1	GGCCAAGAGTGTGCTAAAGAA	ACAGCGTTGATGCCAGACAG
SLC16A3	CGTTCTGGGATGGGACTGAC	ATGTGCCTCTGGACCATGTG
SLC16A14	TGAAGACGACCGAAAGGCTAA	ATGTGAACAAAGAAGGACGAGA G
IDH1	GGTAAAACCTATCATCATAGGT CG	CACATACAAGTTGGAAATTTCTG G
IDH2	GCTGCAGTGGGACCAC TATT	CTCTGCAGTACAAGGC CACA

ALOX12	AGAAAAGTTGACTAGTCCAGTG T	AAAAGCTGTGCTAAACCAATTCC GA
GCLC	TGTCGCTGGGGAGTGATTTC	CAATGCCTTCCTGCAACAGC
SCO2	TCACTCACTGCCCTGACATC	CGGTCAGACCCAACAGTCTT
PYCR1	CCTACGGGGCTGCCAAGAT	ACTCT CCAGCACATGCAAGG
SHMT2	CGAGTTGCGATGCTGTACTT	CTGCGTTGCTGTGCTGAG
MGST1	ATTGGCCTCCTGTATTCCTTG	TAATCCCTCTGCTCCCCTCC
SLC3A2	ACTTGGCTGAGTGGCAGAAT	AGATCGCTGGTGGATTCAAG
CBS	CCACATCACCACACTGCC	GCCGAACTTCTTCCCAATCT
PADI1	CACAGCTCTGGTTGGCTTCA	CTGCACGTCCTTCAGCATCA
PADI2	TGAAGCACTCGGAACACGT	TTGTCACTGCTGGCCTCG
ASS1	CTCCACGATGTCAATACGGC	CAACACCCCTGACATTCTCG
NOS2	GACTGTTGAGATGGAAGAAC	ATCTTCCTGTCTCCGAGGGC
NOS3	GTGATGGCGAAGCGAGTGAAG	CCGAGCCCGAACACACAGAAC
HPRT1	TGGACAGGACTGAACGTCTTG	CCAGCAGGTCAGCAAAGAATTTA
ADSL	CCGCTCTTCCCTGGTCCAGTC	GATTTTCGTTTAATTCTCTTC
IMPDH	TTCGTGCCCTACCTCATAGC	ATGGACCGAAGGACAGACAG
ALDH9A1	CCTGGAGCGAGTCCTCGGGTT	CCCGCTCCAGAACCTCGGCT
SLC1A4	GACCGTACGGAGTCGAGAAG	GGGGGTTTCCTTCCTCAGTG
SLC1A5	AAGCACATCAGCCGTTTCAT	AGTGAGGACACCTCCAGCAG
GAPDH	TCGACAGTCAGCCGCATCT	CCGTTGACTCCGACCTTCA

2.2 Methods

2.2.1 Human Tissue Samples of Thymic Epithelial Tumors (TETs)

2.2.1.1 Tissue Sample Preparation

Preparation of tissue samples for NMR analysis was performed in a humidity-free environment using a nitrogen atmosphere at 10°C (Gogiasvili et al., 2019). These conditions are essential in order to prevent condensation due to working in an open environment on dry ice. After removing the tissue from -80°C storage, it was kept at 10°C for 30 min in a fridge to equilibrate its temperature with the surroundings. Tumor tissue samples for analysis were taken from the thawed tumor specimen using a 2-mm punch (PFM Medical, Köln, Germany) in order to fit into 33 µL disposable inserts (DIs) (Bruker, Rheinstetten, Germany) for 4-mm MAS rotors. The punched tissue was weighed on a calibrated balance, and the DIs were then, after the tissue was inserted, filled with D₂O containing 3-(Trimethylsilyl)propionic-2,2,3,3-d₄ acid sodium salt (TSP) as an internal standard to reference the frequency scale of the spectrum to 0 ppm. The

prepared DIs were stored in a -80 degree freezer until measurement (Part of these results were recently submitted for publication in *CANCERS*.).

2.2.1.2 HR-MAS-¹H-NMR measurement conditions

NMR spectral acquisition was performed using a Bruker Avance III NMR spectrometer equipped with a 14.1 T magnet at 278 K. Acquisition and pre-processing of NMR spectra was performed under the control of a workstation with TopSpin 3.2 (Bruker BioSpin, Karlsruhe, Germany). Two different ¹H-NMR spectra were collected: a 1D ¹H spectrum providing quantitative metabolite data for statistical analysis, while 2D TOCSY and 2D ¹H-¹³C HSQC experiments assisted in peak assignment and metabolite identification using standard Bruker pulse programs. For 1D ¹H spectra performed for each sample, a Carr Purcell Meiboom Gill (CPMG) pulse sequence with 200 echoes was used to suppress the macromolecular background. Solvent signal suppression was achieved by pre-saturation during the relaxation delay (Frequency range 7 kHz, 16 K data points, relaxation delay 4 s, 128 scans, HRMAS rotation frequency 5 kHz). All spectra were processed using an exponentially decaying window function with a line broadening of 0.3 Hz and the baseline was automatically corrected. Each NMR spectrum was referenced to the signal of 3-trimethylsilylpropionic-2,2,3,3-d₄-acid sodium salt (TSP) at 0.0 ppm. As is already known, the TSP signal may be affected by proteins or other macromolecules present in samples and for that reason I used the “**E**lectronic **R**eference **T**o access **I**n vivo **C**oncentrations” (ERETIC) technique for the calibration of sample spectra (Akoka et al., 1999). The spectral region between 0.8 to 10 ppm was analyzed for metabolites and their concentrations (in mM) using the Chenomx NMR Suite 7.3 (Chenomx Inc., Edmonton, Alberta, Canada) based on its 600 MHz library. Chenomx NMR Suite 7.3 compares the integral of a known reference signal (e.g. TSP or formic acid) with signals derived from a library of compounds containing chemical shifts and peak multiplicities. As an ERETIC reference a sample of a 0.3%-TSP-solution in D₂O was used, which was measured under the same conditions as the tissue samples. The reference signal was calibrated with ERETIC, imported into the Chenomx-Software and all metabolite concentrations were

calculated in relation to this reference signal. From the resulting relative concentrations the absolute concentrations in the tissue sample were calculated as follows:

$$\text{Metabolite concentration} = \frac{\text{mass (0.3 \% TSP in D}_2\text{O in mg)} \times 0.003}{\text{molecular mass TSP (172.24 g/mole)}} \\ \times \frac{\text{concentration of metabolite signal in Chenomx (mM)}}{\text{concentration of TSP from ERETIC (mM)}} \times \frac{10^6}{\text{mass of tissue (mg)}}$$

(Part of these results were recently submitted for publication in *CANCERS*.)

2.2.1.3 NMR related statistical Analysis for tissue samples

To check whether there is a significant statistical difference between the classes A (indolent/non-aggressive thymomas) and B (aggressive thymic epithelial tumors), a Welch two sample t-test was run using the “t.test” module implemented in R 3.6.2. The “geom_boxplot” and “facet_wrap” modules of R 3.6.2 were used to generate the boxplots of metabolite concentrations.

Further statistical analyses were performed using the web server Metaboanalyst 4.0 (Chong et al., 2019). Metabolite data were mean-centered and the intensities of the spectral peaks of each given sample were normalized to the sum of all metabolite concentrations to avoid the contribution of dilution effects. Data (non-aggressive vs. aggressive cancers) was then subjected to a “scarce partial least square-discriminant analysis” (sPLS-DA) (Lê Cao et al., 2011) which can be thought of as a supervised version of a principal component analysis (PCA) in the sense that it achieves dimensionality reduction with full awareness of the class labels. sPLS-DA preserves as much covariance as possible between the original data and its labeling. For the identification of biomarkers receiver operating characteristic (ROC) curves were generated for all metabolites. The aim of classical ROC curve analysis is to evaluate the performance of a single feature, either one metabolite or a combined metabolite ratio pair, as a biomarker. The ROC curve summarizes the sensitivity and specificity of that single feature to accurately classify data, which can then be used to compare the overall accuracy of different biomarkers. It is reported that an “area under the curve” (AUC) value between 0.9 and 1.0 is excellent, and a value between 0.8 and 0.9 is good. A greater AUC value indicates a greater ability to distinguish thymoma from TC. The AUC can be interpreted as the probability that a randomly selected diseased subject is classified as diseased rather than a casually selected healthy subject.

Finally, a metabolic pathway analysis (Xia & Wishart, 2010) was performed for all identified metabolites in order to identify the most relevant metabolic pathways involved in the TC and thymoma groups (Part of these results were recently submitted for publication in *CANCERS*.).

2.2.1.4 MetPA analysis of metabolite profiles for metabolic pathway detection

To investigate whether identified metabolites represent a random sample of compounds or reflect the enrichment of known metabolic pathways, the identified metabolites and their concentrations were subjected to MetPA (Xia & Wishart, 2010) metabolic pathway analysis using Metaboanalyst 4.0 (Chong et al., 2019). The output of the MetPA analysis are KEGG pathways (henceforth called “KEGG metabolite-based metabolic pathways” (Kanehisa et al., 2008), p-values that indicate the degree of enrichment of these pathways, and ‘impact-values’ that reflect the number of metabolites significantly altered in the respective pathway (Part of these results were recently submitted for publication in *CANCERS*.).

2.2.1.5 Metabolic gene set enrichment analysis of the TCGA transcriptomic dataset

To investigate whether KEGG metabolite-based metabolic pathways were reflected by enriched KEGG pathways on the transcriptomic level (henceforth called “KEGG transcriptome-based metabolic pathways”), I interrogated the transcriptomic profiles of the TCGA thymic cancer database (CBioPortal, <http://www.cbioportal.org/>) using Gene Set Enrichment Analysis (GSEA) as described recently (Yamada et al., 2020). The TCGA database comprises 10 type A, 48 AB, 12 B1, 25 B2, 10 B3, 2 rare other thymomas, and 10 TCs (Radovich et al., 2018), and the comparison between indolent (A, AB, B1 thymomas) and aggressive TETs (B2 and B3 thymomas and TCs) formed the basis to rank genes due to their t-values for GSEA (Geistlinger et al., 2016). Since the D-glutamine and D-glutamate KEGG pathway (hsa00271) comprises only 5 genes, GSEA was not feasible. To check whether our cohort (n=15) analyzed by NMR is representative of the TCGA cohort (n=117), I used qRT-PCR to quantify transcripts of 27 genes selected from the identified metabolic pathways in snap frozen TET material as described (Yamada et al., 2020). For primers and conditions see Table 2.1.9.1. Since the expression profiles of 25 of the 27 genes overlapped in both cohorts (Figures 3.1.5.1, 3.1.5.2), our cohort is likely fairly representative of the TCGA cohort. In addition to GSEA, I also used the DAVID annotation database provided at <https://david.ncifcrf.gov> (Huang et al., 2013) to identify

MATERIAL AND METHODS

pathway enrichment. This analysis was focused on 90 genes selected from the “KEGG transcriptome-based metabolic pathways” on the basis of their most differential expression between indolent and aggressive TETs using p-values <0.05 . In addition to GSEA, which was based on the comparison between indolent (A, AB, B1 thymomas) and aggressive TETs (B2, B3 thymomas and TC) using expression levels of all member genes of the seven “KEGG transcriptome-base metabolic pathways”, I used the DAVID annotation database provided at <https://david.ncifcrf.gov> (Huang et al., 2013) to identify pathway enrichment. However, this analysis relied on the expression levels of genes with differential expression between individual thymoma types with similar lympho-epithelial composition but different (indolent vs. aggressive) biological behavior. This established strategy takes into account that the variable abundance of non-neoplastic T cells in the various TET histotypes can obscure molecular differences between them (Yamada et al., 2020). Using a p-value <0.05 as a cutoff, the individual comparisons of A with B3 thymomas, A thymomas with TC (all T-cell-poor), and AB-plus-B1 with B2 thymomas (all T-cell-rich) identified 53 differentially expressed genes among the member genes of the seven “KEGG transcriptome-based metabolic pathways” for subsequent DAVID analysis (Part of these results were recently submitted for publication in *CANCERS*.).

2.2.1.6 Transcriptomics related statistical Analysis

The statistical analyses of gene expression data were performed with GraphPad Prism V6.0 (GraphPad Software Inc, La Jolla, CA, USA). Two-tailed student’s *t*-test and one-Way ANOVA were applied when gene expression of metabolism-related genes altered in different groups of thymic tumors in comparison to normal thymuses. A subsequent Tukey’s multiple comparisons test was used to compare variances, with $p < 0.05$ at a confidence level of 95% ($p < 0.05$) was considered as significant (Part of these results were recently submitted for publication in *CANCERS*.).

2.2.1.7 Analysis of online available datasets

I analyzed the TCGA datasets (CBioPortal, <http://www.cbioportal.org>) that contain cohorts of thymic epithelial cancers (Thymoma and thymic carcinoma), and the dataset on mRNA expression profiles provided by Petrini et al. containing 22 cases of TETs: type A (n=5), AB (n=2), B2 (n=3), B3 thymomas (n=5), and TC (n=7, including 5 TSQCCs, and 2

MATERIAL AND METHODS

undifferentiated carcinomas (GSE57892) (Part of these results were recently submitted for publication in *CANCERS*.).

2.2.1.8 General statistical Analysis

All statistical analyses were performed with GraphPad Prism V6.0 (GraphPad Software Inc, La Jolla, CA, USA). Two-tailed student's t-test was used with $p < 0.05$ and a confidence level of 95% when comparing cFLIP gene expression levels in different groups of thymoma. A subsequent F-test was used to compare variances with $p < 0.05$ at a confidence level of 95% (in both tests $p < 0.05$ was considered as significant) (Part of these results were recently submitted for publication in *CANCERS*.).

2.2.2. Two Dimensional and Three Dimensional cell culture

2.2.2.1 Cultivation of TET cell lines

The human thymic carcinoma cell line, 1889c and the thymic NUT carcinoma cell line, Ty82 were used here. For the 1889c cell line the standard 2D cell culture medium consists of Roswell Park Memorial Institute (RPMI) medium 1640 1X with 25mM HEPES supplemented with 10% (v/v) fetal bovine serum (FBS) and 1% (v/v) penicillin and streptomycin. For the Ty82 cell line Dulbecco's modified eagle media (DMEM) was used with the same supplements as for the 1889c cell line. Cells were incubated in a 5% CO₂ chamber at 37°C and used for experiments during the logarithmic growth phase.

2.2.2.2 Cell thawing and cryopreservation

For thawing, in order to get rid of any remaining effect of DMSO, and for storage in liquid nitrogen, cell pellets were thawed in a water bath at 37°C for less than 1 minute. The process of thawing has to be stopped, before the ice is completely molten. Then fresh culture medium is added and the mixture is centrifuged two times at a speed of 1100 rpm for 5 minutes to remove the DMSO. Afterwards it is re-suspended in fresh culture medium and left overnight as 2D culture in the incubator. After an overnight incubation in a humidified 5% CO₂ atmosphere at 37°C to grow the cells in a T25 biolite 25cm² vented plastic flask, the medium is replaced with fresh medium to remove any remaining DMSO. Afterwards cells were grown for at least two passages before starting the experiments and the medium was changed every 2-3 days. On the other hand, for freezing the cells, freezing solutions were prepared freshly before the use

MATERIAL AND METHODS

and kept cold, consisting of 40% growth medium with 40% FBS and 20% DMSO. After forming cells pellets, 1ml of cell suspension was mixed with 1ml of freezing solution, stored in cryopreservation tubes and transferred to a cell freezing container (Mr. Frosty™) containing isopropanol and stored at -80°C for 24 hours. For short term usage one can keep the cells at -80°C but for long term usage tubes should be stored in liquid nitrogen.

2.2.2.3 Passaging the cells

After thawing the cells and when the confluency is about 80%, culture medium in the flask was removed and the cells were briefly washed with 10ml PBS. After gentle swirling, PBS was discarded and 1ml of trypsin-EDTA (for both cell lines) was added with direct monitoring under an inverted microscope to check the cells' detachment. After ensuring the cells' detachment 9 ml of culture medium was added and cells were slowly aspirated and mixed. Afterwards 10ml of culture medium that contains 1ml trypsin and 9ml medium with cells was centrifuged at a speed of 1100rpm for 5 minutes. Afterwards the cell pellet was re-suspended in 10ml fresh culture medium and counted with C-ships for further experiments if needed. Cells were kept in a 5% CO₂ chamber at 37°C until the start of a following experiment..

2.2.2.4 Methanol extraction for 2D cells

Ty82 cells and 1889c cells were cultured in 6-well plates with a starting seeding number of 10000 cells per well in 300µl culture, for both control cell cultures and cell cultures treated with bortezomib. After 24 hours, cells were treated for 2 days, before methanol extraction was performed for both controls and treated samples in order to measure the samples with NMR. The protocol consists of three main parts 1) Methanol extraction 2) N₂-evaporation 3) Freeze-drying. Starting with methanol extraction, plates were taken from the incubator and placed on ice. All plates were washed with cold PBS (1x) 3 times. Afterwards, PBS was removed and the plates are placed in a bucket that is filled with liquid nitrogen for 2 minutes afterwards moving the plates on ice again and 5 ml cold methanol is added to the plate. Subsequently, the plates were put on a shaker in the fridge for 15 minutes. After 15 minutes, the 5 ml of methanol were collected into a 15 ml falcon, and centrifuged at 4000 rpm for 30 minutes at 4°C. Then supernatant were collect into new falcon. For N₂ evaporation a self-made device (Figure 2.2.2.4.1) was used with long cannulas (nitrogen comes out from the cannulas) under the hood to pump the nitrogen inside the samples and dry out the samples. The falcons with samples were placed in a falcon stand before starting the evaporation, carefully inserting cannulas until

MATERIAL AND METHODS

just above the methanol level. Evaporate approximately for 5 h (about 1 ml per h) with nitrogen flow. Methanol level were checked every hour and insert cannulas deeper into the sample tubes. It was important to wipe the cannulas with methanol before and after use to avoid any contamination, then samples were stored at -80°C or continue directly with freeze-drying. For freeze-drying warm up phase was started via cool to -27°C afterwards the samples were placed without a lid in the falcon stands and wait until they dry out, then stored at -80°C until measurement commences.

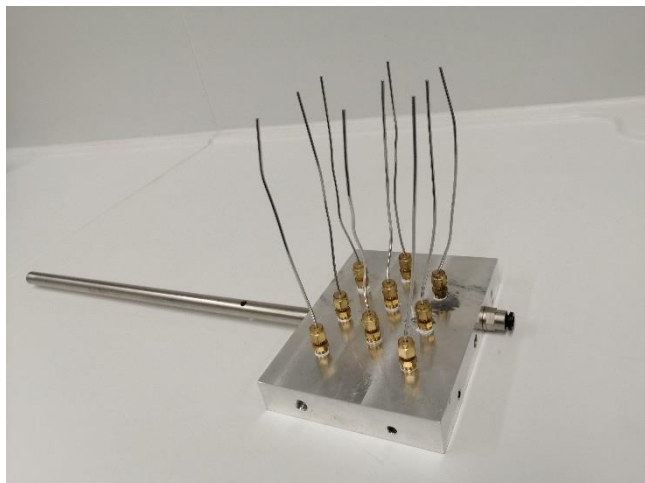


Figure 2.2.2.4.1. Home-made N_2 evaporation unit which helps to evaporate the methanol slowly prior to the freeze-drying step.

2.2.2.5 NMR measurement conditions for 2D cell culture

All NMR experiments were performed at a BRUKER AVANCE NEO 600 spectrometer operating at a frequency of 600.13 MHz for ^1H detection. For sensitivity reasons, a cryogenic NMR probe was employed. 2D cell culture samples were measured with a double watergate pulse sequence with excitation sculpting (Hwang & Shaka, 1995) for suppression of the water signal. I used the “Electronic REference To access In vivo Concentrations” (ERETIC) technique (Akoka et al., 1999) for the calibration of the sample spectra.

2.2.2.6 NMR related statistical Analysis for 2D

Statistical analyses were performed using the web server Metaboanalyst 4.0 (Chong et al., 2019). Metabolite data were mean-centered and the intensities of the spectral peaks of each given sample were normalized to the sum of all metabolite concentrations to avoid the

contribution of dilution effects. The “geom_boxplot” and “facet_wrap” modules of R 3.6.2 were used to generate the boxplots of metabolite concentrations.

2.2.2.7 Formation of spheroids

2.2.2.7.1 Simple rotation technique (SRT)

The simple rotation technique was used to produce uniform and reproducible 3D cells that can be used in post analysis especially with NMR testing experiments since spheroid morphology is of prime importance. Costar® 24 well flat Bottom Ultra-Low Attachment Surface plates that overcome the need for plate coating (Reduce batch to batch variation from coating producer) are required to prevent cells' adhesion to the bottom. For this purpose, a Lab rotator has to be placed inside the incubator at a speed of 100 rpm, that mechanically enhances cell-cell adhesion which forms spherically reproducible 3D cell culture. Two different medium recipes were used to produce the 3D cells to see both the effect of serum on the 3D shape growth and to reach the most reproducible shape. The first one is Thymic Multicellular Tumor Spheroids (TMTS) Serum which consists of the same ingredients of the 2D culture medium for both cell lines. The second medium used for both is Serum Free medium, Thymic tumor spheroid (TTS), which consists of 50mL RPMI without HEPES with 5mL (v/v) penicillin and streptomycin, 100uL Epidermal Growth Factor human EGF, 500uL B-27 Supplement (50x) light sensitive, 10uL Recombiant Human FGFb, 25µL Insulin, 500µL Hydrocortisone, 250µL Heparin. Four different seeding numbers were used for the Ty82 cell line, namely 1000, 2000, 3000 and 5000 cells to see the growth speed and morphology. After the cells grow in 2D for some time and they reach 80% confluency, they were trypsinized and seeded with different cell numbers via counting with C-chips as mentioned before. The medium is changed every 2-3 days. Spheroid sizes ranged between 450-800 µm after approx. 12days; if kept longer the size gets bigger. The Ty82 cell line formed uniform and reproducible 3D structures using this technique for both TMTS and TTS, while the 1889c cell line formed clusters instead of round, 3D structures (i.e. spheroids). Therefore, the conventional method had to be combined with the use of Matrigel® in order to reproducibly achieve 3D structures of the same quality as in the case of Ty82 cells as explained in detail next.

2.2.2.7.2 Microtissues natural 3D

3D Petri Dish® grows cells in three dimensions and forms multi-cellular microtissues that more closely mimic tissues in vivo by maximizing cell-cell interactions. A wide range of starting seeding numbers is proposed in the manufacturer's protocol, depending on the cell type and desired final spheroid size. The use of this method was important to overcome the problems with the formation of 1889c cells, since it allows the co-culturing of the cells with matrigel/ECM [ECM, extracellular matrix] and a high reproducibility like SRT (simple rotation technique) but with shorter times. Starting with autoclaving the molds with 0.5 g UltraPure™ Agarose, the agarose was mixed with 25 ml PBS, under sterile conditions, then dissolved and cooked in the microwave to get a clear homogenous solution. After cooling down the agarose to 60°C, 500 µL were added to each mold (each containing 81 wells). The gel was left to solidify, then the agarose was carefully removed from the mold and equilibrated with culture medium to remove any possible air bubble. Figure 2.2.2.7.2 shows the work flow. The molds containing cells were filled with 2.5 ml medium, which was changed every 30 hours. After leaving the cells for around 3 days to reach the required size they were transferred into 24 well plates with SRT in order to improve their morphology for NMR measurement. In order to remove the cells from the 3D molds, one well from a 24well plates was filled with 1 ml culture medium, and the mold was gently inverted upside-down and centrifuged at 500rpm speed for 5minutes. Table 2.2.2.7.2 shows the different seeding numbers with possible final spheroid size.

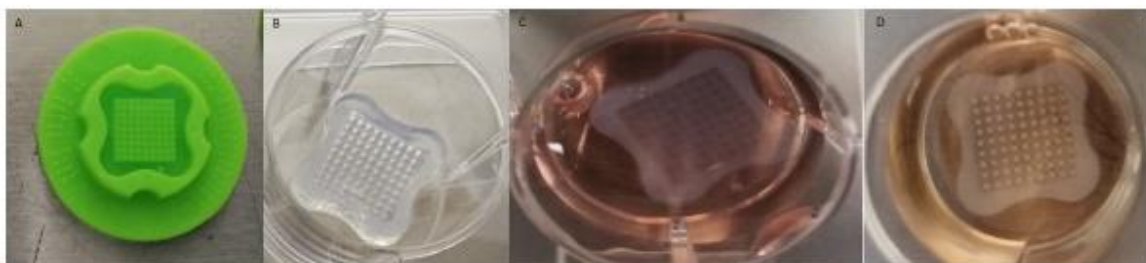


Figure 2.2.2.7.2.. Formation of 3D cells with 3D Petri Dish®. A) Autoclaved mold with 2% agarose. B) Empty agarose mold. C) Equilibration of empty mold with fresh culture medium. D) Mold with spheroids (small white dots).

Table 2.2.2.7.2. Spheroid size by number of cells seeded

Spheroid diameter (μm)	Cells/spheroid	Total cells seeded (cells/190 μl)
200	1,000	81,000 /190 μl
300	3,375	273,000/190 μl
400	8,000	648,000/190 μl
500	15,625	1.3 x10 ⁶ /190 μl
600	27,000	2.2 x10 ⁶ /190 μl
700	42,875	3.5 x10 ⁶ /190 μl

2.2.2.8 Novel NMR measurement setup for spheroids as a new tool to investigate the metabolism of 3D cell culture systems with time and spatial resolution under viable conditions.

This technique has been patented: „Verfahren zur Analyse des Metaboloms dreidimensionaler lebender Zellkulturen mittels NMR-Spektroskopie“, DPMA Nr. 64/24651 jm/s.

2.2.2.8.1 Experimental setup

For the measurement set-up for spatial resolved NMR spectroscopy of living spheroids, three main requirements have to be fulfilled: 1) the spheroid has to be kept under physiological conditions, namely proper temperature, pH-value, dissolved oxygen and carbon dioxide content as well as nutrition supply and waste product removal. In an incubator, the latter two are achieved by frequent medium replacements. 2) The position of the spheroid has to be fixed, without imposing any additional mechanical stress on the spheroid cells. 3) All compartments of the sample setup inside the NMR probe have to be designed to minimize magnetic susceptibility differences, i.e. the spheroid has to be positioned inside a glass capillary on a

platform fixing the location of the spheroid with respect to the external magnetic field and the z-gradient of the probe. As the capillary inner diameter (870 μm) was chosen larger than that of studied spheroids (500-860 μm) and of the platform (400 μm) the spheroid could be easily perfused with a medium flow. The U-shape of the capillary serves to remove consumed medium from the measurement chamber. In order to verify the performance of this setup different hydrogen free PTFE and KelF polymers in various setup geometries were tested, which, however, resulted in severe NMR line broadenings due to susceptibility differences. Thus, chose to build all components in the measurement area out of borosilicate glass to meet the third requirement as shown in Figure 2.2.2.8.1. As even the glass surface of the spheroid platform led to distortions, a cylindrical 2 mm high ultra-high pure agarose gel spacer was positioned between the platform and the spheroid. This setup prevents any unwanted interaction of the glass surface with the spheroids, while interactions with the agarose support ensures growth conditions comparable to an incubator. During a measurement, the sample chamber of the cryogenic probe was kept at 37 $^{\circ}\text{C}$ by the integrated temperature unit. The medium supply was homogenized using a magnetic stirrer and the gas phase above the liquid was continuously exchanged with synthetic air containing 5% CO_2 . The medium supply was kept at 37 $^{\circ}\text{C}$ to ensure a physiological O_2/CO_2 medium saturation and to stop gas bubble formation in the measurement chamber because of temperature differences. A peristaltic pump delivering a flow rate of 4 $\mu\text{L}/\text{min}$ ($v=16.8 \mu\text{m}/\text{min}$) serves to perfuse the spheroid. Note that all components in contact to the cell medium have been sterilized prior to a spheroid measurement using steam sterilization. Finally, the mandatory deuterium lock signal could be easily achieved with the presented setup, as the U-shape can be placed in a D_2O filled 5 mm standard NMR tube. While the D_2O lock signal is required to correct magnetic field drifts, a cell contact has to be avoided as unnatural high deuterium concentrations are known to impair cell metabolism. This established technique described here is the first worldwide both to monitor the metabolites within the spheroid in a spatiotemporal way and to check the drug impact on the spheroid as a whole (Reprinted with permission from *Anal. Chem.* 2021, 93, 40, 13485–13494, doi: 10.1021/acs.analchem.1c02221, Publication Date: September 3, 2021, Copyright 2021 American Chemical Society.).

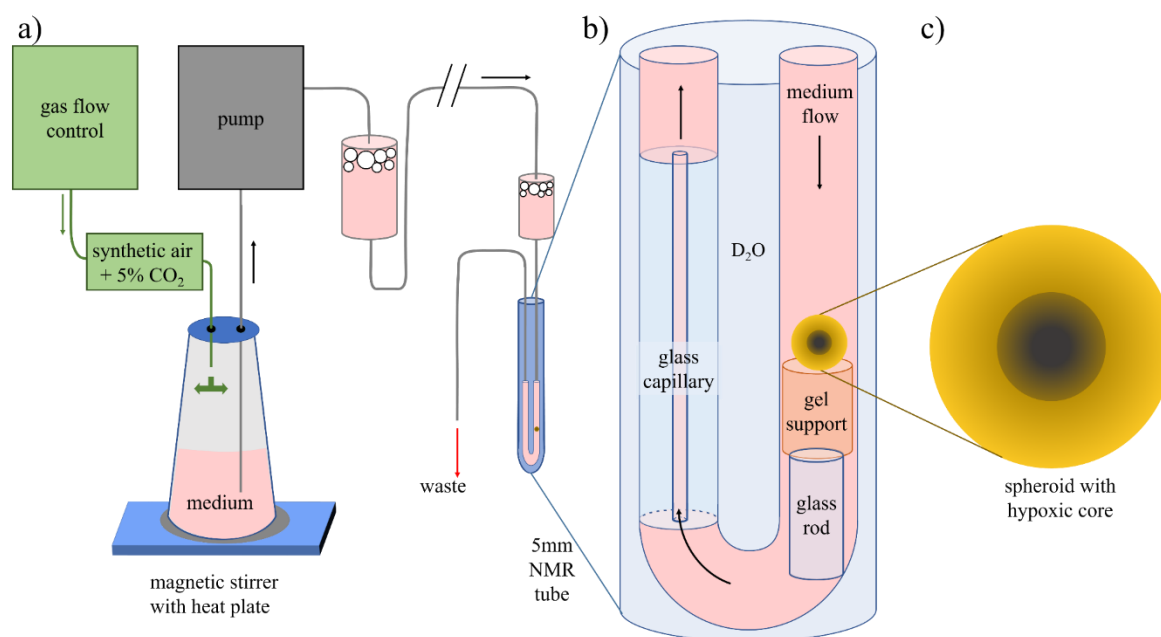


Figure 2.2.2.8.1: Schematic representation of the 3D NMR measurement setup. a) A general overview of necessary devices used to achieve incubator condition for the spheroid. The medium supply is kept at 37 °C under an air atmosphere containing 5% CO₂. The medium is transferred through a PTFE tube using a peristaltic pump. To trap gas bubbles formed in the tubes, two liquid chambers are placed behind the medium supply and before the measurement chamber. b) Enhanced representation of the measurement chamber showing the spheroid positioned on a gel support on top of a glass platform. Medium background intensity at the position of the spheroid is reduced by a glass capillary on the other side of the U-shape. The U-shape itself is located in a standard 5 mm NMR tube filled with D₂O to achieve a lock signal. c) Enhanced picture of a spheroid exhibiting a hypoxic core area. (Reprinted with permission from *Anal. Chem.* 2021, 93, 40, 13485–13494, doi: 10.1021/acs.analchem.1c02221, Publication Date: September 3, 2021, Copyright 2021 American Chemical Society.)

2.2.2.8.2 Whole spheroid NMR pulse sequences and pulse properties for toxicity testing

Experimental conditions were the same as in the slice selective experiments (see chapter 2.2.2.8.3), except for the bandwidth of the selective pulse, which was adjusted to a slice thickness of 1 mm at a gradient strength of 0.28 T/m. This gradient strength is considered a compromise between the effect of a shift dependency of the slice position of an NMR signal as

well as the bandwidth and hence power increase of a selective pulse to excite or to refocus magnetization.

2.2.2.8.3 Spatial-resolved NMR pulse sequences and pulse properties for slice selective experiments

In the 3D cell culture models studied within this thesis metabolic show merely a dependance on the distance to the center of the spheroid, i.e. radial concentration profiles describe the metabolic profile of a spheroid in full because of its spherical symmetry. The experiment described here, however, delivers slice selectively acquired NMR data. A mathematical technique, called double Abel transform, therefore has to be used to calculate radial concentration profiles from the slice selective data. The measurement of slices, which was preferred over the measurement of voxels, has two advantages: As the signal-to-noise ratio is proportional to the detection volume, a strong increase of signal is found in slice selective experiments as compared to voxel selective experiments. Second, the hardware requirements are much lower as only a single gradient coil is required, a requirement, which is easily met for standard NMR hardware.

In the absence of a gradient, the resonance frequencies ν_0 are mainly given by the external magnetic field strength B_0 and the chemical shielding σ , while an imposed gradient adds a magnetic field in the z -direction (B_z), resulting in a the resonance frequency ω_z according to

$$\omega_z = \gamma(1 - \sigma)(B_0 + B_z) \approx \omega_0 + \gamma G_z z \quad (1)$$

where γ is the nuclear gyromagnetic ratio. The given approximation holds as long as the shielding parameter is small. In the rotating coordinate system equation (1) can be rewritten as

$$\Omega_z \approx \Omega_0 + \gamma G_z z \quad (2)$$

Here Ω_z corresponds to the offset of a pulse from the frequency of the rotating frame (typically set to the receiver frequency) that is needed to excite nuclear spins at a distinct z -position. In a spatial selective NMR experiment the bandwidth of the pulse $\Delta\omega_p$ is chosen in such a way, that the resonance condition holds only within a slice of the height Δz :

$$\Delta\omega = \Delta\Omega_z \approx \gamma G_z \Delta z \quad (3)$$

It is important to emphasize that the position of the slice excited by a pulse is different for every NMR resonance depending on its chemical shift. While this effect is minor for in vivo NMR spectroscopy employing spatial resolution on the mm scale, it is important when resolution as low as a few μm is desired and/or high field strengths are employed. In a 2D spatial resolved experiment, the center frequency of the slice selective pulse can be incremented, which allows for a scan of the z-dimension. Afterwards the correct position of each resonance can be calculated by rewriting equation (2) as

$$z = \frac{(\Omega_z - \Omega_0)}{G_z * \gamma} \quad (4)$$

In this study, I employed sinc pulses, with an experimentally determined excitation profile as depicted in Figure 2.2.2.8.3. In order to avoid phase distortions, the pulses for excitation and refocussing are incorporated in a Hahn-echo. The selective pulses for excitation and refocusing were phase cycled to select the desired coherences. To speed up the measurement, I employed two slice selective pulses in a Hahn-echo sequence depicted in Figure 2.2.2.8.4a, which allows an interleaved slice acquisition: Two or more slices can be acquired subsequently, skipping the relaxation delay in between, i.e. I measure two slices before employing a hardware recovery delay of 1s that is required to fulfill the probe head gradient coil specification. During hardware recovery an optional water suppression by presaturation can be employed. To avoid problems with spin lattice relaxation, the two subsequent experiments have to be chosen at two z-positions the difference of which is larger than the excited slice thickness. As the bandwidth of a pulse is usually not rectangular (Figure 2.2.2.8.3a), I set this difference to even more than twice the excitation slice thickness. Figure 2.2.2.8.3b illustrates the above described interleave procedure for an example of a spheroid with a diameter of 860 μm giving the results shown in Figure 2.2.2.8.3c. After all slices have been measured (here 24) the procedure is repeated according to the number of scans following an eight step phase cycle. Compared to the standard method, in which the full number of scans is acquired slice after slice, this procedure strongly decreases the measurement time and additionally avoids time differences between slices (Reprinted with permission from *Anal. Chem.* 2021, 93, 40, 13485–13494, doi: 10.1021/acs.analchem.1c02221, Publication Date: September 3, 2021, Copyright 2021 American Chemical Society.).

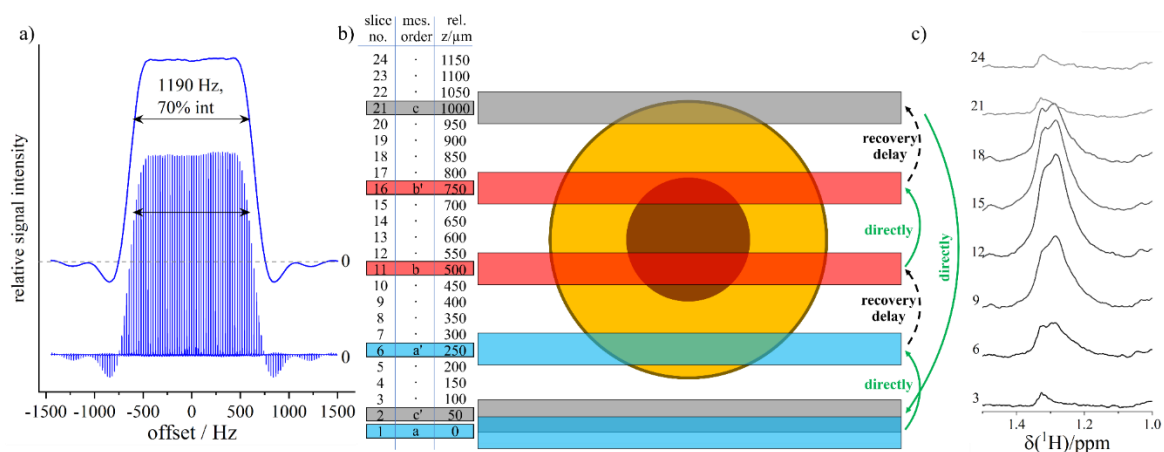


Figure 2.2.2.8.3: a) Summarized NMR spectra and corresponding integrated intensity (blue curve) of a lithium lactate methyl resonance stepping the offset frequency by 25 Hz from -1.5 to 1.5 kHz using slice selective excitation. The bandwidth of 1190 Hz corresponds to a slice thickness of 100 μm for ^1H nuclei at a gradient of 0.28 T/m. b) Graphical representation of a slice selective experiment using a step size of 50 μm and $\Delta z=100 \mu\text{m}$. After acquiring two slices separated by 250 μm directly after each other (e.g. 1 and 6) a recovery delay is placed before the measurement of the next two slices. The table indicates the slice number, its relative position and the measurement order using letters, where equal letters with and without a prime have been measured without a recovery delay in between. c) Shows a cutout of ^1H NMR spectra measured for a spheroid with a diameter of 860 μm , where increasing signal intensities towards the center of the measurement regime proof unambiguously the successful detection of a single spheroid. (Reprinted with permission from *Anal. Chem.* 2021, 93, 40, 13485–13494, doi: 10.1021/acs.analchem.1c02221, Publication Date: September 3, 2021, Copyright 2021 American Chemical Society.)

The interleaved procedure was showed a negligible intensity decrease which was strongly overcompensated by the reduced measurement time. Interleaved acquisition just revealed differences in water suppression.

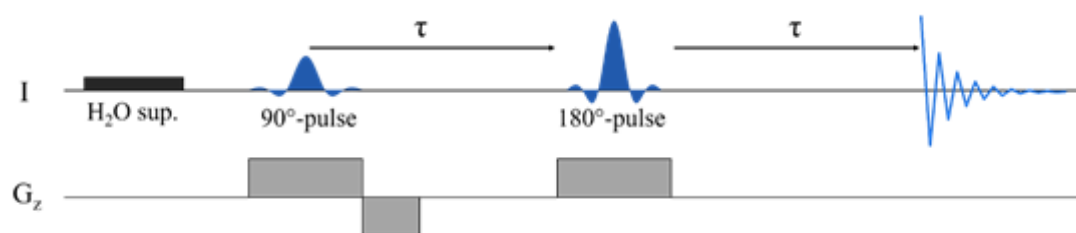


Figure 2.2.2.8.4 The slice selective sequence employed in this work. Slice selective pulses accompanied by a z-gradient (G_z) and the resulting FID signals are shown in blue (Reprinted with permission from Anal. Chem. 2021, 93, 40, 13485–13494, doi: 10.1021/acs.analchem.1c02221, Publication Date: September 3, 2021, Copyright 2021 American Chemical Society.)

2.2.2.8.4 Double Abel inversion allows access to radial concentration profiles

The pulse sequence in Figure 2.2.2.8.4 measures the signal intensity of an NMR resonance within a rectangular measurement slice. Consider for instance a slice taken in the center of a spheroid, then the signal from this slice comprises metabolites from both the hypoxic core and the shell of the spheroid. It would, however, be more interesting to discriminate between metabolite concentrations in these two domains, i.e. an individual radial intensity profile $g(r)$ has to be determined for every metabolite signal using the measured slice signal intensity $h(z)$. This can be achieved using inverse Abel transformation (Pretzier et al., 1992). The Abel transformation projects a 3D object with a rotation axis onto a plane or a circular 2D object on a 1D vector. Hence, if one wants to obtain radial metabolite distributions from a 3D object like a spheroid, a double Abel inversion has to be calculated. An analytical solution to this problem exists (Vest, 1974) and can be applied to the ideal model spheroid given by

$$g(r) = \frac{1}{2\pi z} \frac{dh(z)}{dz} \quad (5)$$

The results for an idealized model spheroid with a core diameter of 300 μm and shell thickness of 200 μm are shown in Figure 2.2.2.8.5. This model can be used to illustrate the signal intensity expected for NMR resonances homogeneously distributed within the shell, the core or the total spheroid. Figure 2.2.2.8.5b shows the ideal radial intensity profile that needs to be determined from the signal intensity. Core NMR resonances are found in the regime $r/\mu\text{m}$ $[-150, 150]$, while shell NMR resonances are found at $\pm[150, 350]$ with a normalized intensity of 1. For this model, the simulated measurement intensity depicted in Figure 2.2.2.8.5c corresponds to the total volume of the shell and the core within a certain measurement slice. Applying equation (5) to the three distributions directly leads to the desired radial intensity profile, however, with a defect at $r \rightarrow 0$ (Figure 2.2.2.8.5d). (Reprinted with permission from Anal. Chem. 2021, 93, 40, 13485–13494, doi: 10.1021/acs.analchem.1c02221, Publication Date: September 3, 2021, Copyright 2021 American Chemical Society.).

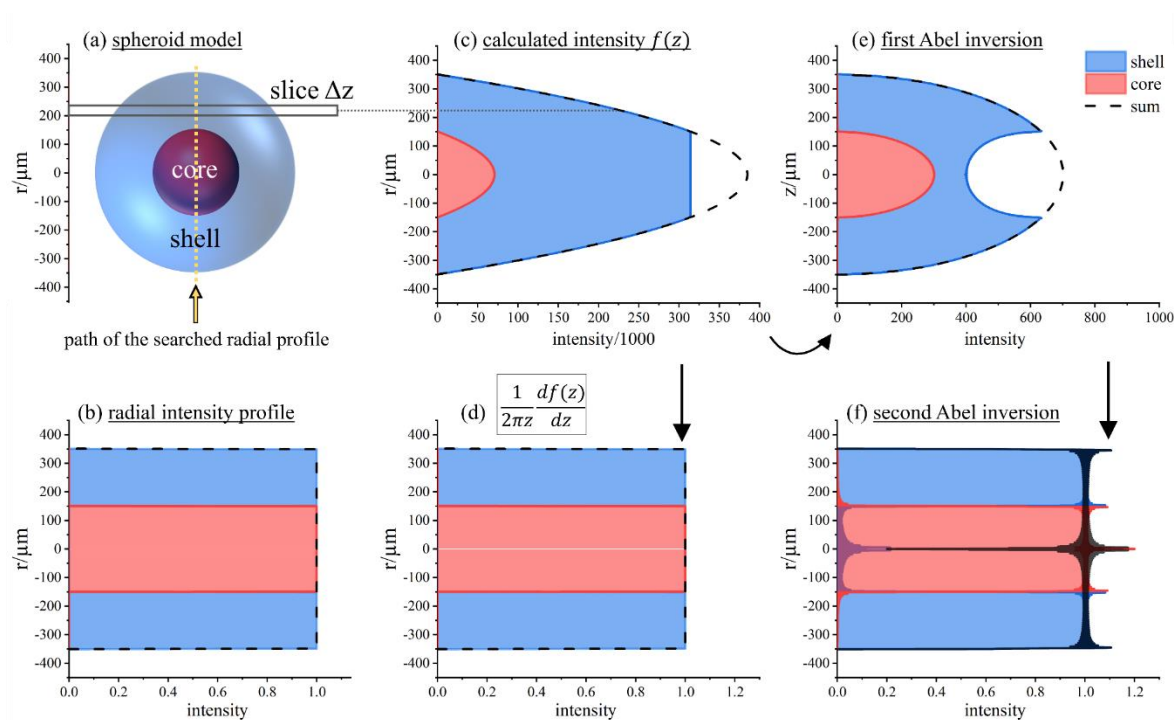


Figure 2.2.2.8.5: (a) Model spheroid with a core diameter of 300 μm and an outer diameter of 700 μm , measurement slice and a path for which the intensity distribution has to be determined. (b) Radial intensity profiles along the path indicated in (a) assuming metabolites homogeneously distributed in the core, the shell or the total spheroid normalized to unity. (c) Intensities $f(z)$ from the different domains of the same spheroid calculated via respective volumes within slices for a step width and Δz of 1 μm . (d) Profile $g(r)$ calculated using equation (5) for the intensity in (c). (e) and (f) show the results from the first and second Abel

inversion of the calculated intensity using 100 cosine functions. The inlets demonstrate that the resulting profiles would be also obtained performing a hypothetical slice selective experiment on the central 2D section of the spheroid and on the path shown in (a), respectively. (Reprinted with permission from *Anal. Chem.* 2021, 93, 40, 13485–13494, doi: 10.1021/acs.analchem.1c02221, Publication Date: September 3, 2021, Copyright 2021 American Chemical Society.)

2.2.2.9 NMR measurement conditions for spheroids

All NMR experiments have been carried out on a Bruker Avance NEO 600 spectrometer operating at 600.13 MHz (14.1 T) using a cryogenic NMR probe that allows for the application of a maximum z-gradient of 0.5 T/m. Rectangular pulses were performed at a frequency of 32 kHz, while power levels of spatial selective pulses have been carefully optimized. For the spatial selective pulses, a z-gradient of 0.28 T/m was used. This is considered a compromise between the effect of a shift dependency of the slice position of an NMR signal as well as the bandwidth and hence power increase of a selective pulse to excite or to refocus magnetization. In advance to any experiment with high spatial resolution, an experiment with low resolution was performed to localize the spheroid accurately. These localization experiments employed a slice thickness and step size of 200 μm . The same medium as under normal growth conditions in an incubator was used. All interpulse delays both in Hahn echo and in CPMG experiments were set to 1 ms. Quantification was achieved using a 9 mmol/L aqueous solution of sucrose filled in the spheroid measurement insert as an ERETIC (Akoka et al., 1999) reference.

2.2.2.10 NMR related statistical Analysis for 3D cells

Statistical analyses were performed using the web server Metaboanalyst 4.0 (Chong et al., 2019). Metabolite data were mean-centered and the intensities of the spectral peaks of each given sample were normalized to the sum of all metabolite concentrations to avoid the

MATERIAL AND METHODS

contribution of dilution effects. The “geom_point” and “facet_wrap” modules of R 3.6.2 were used to generate the boxplots of metabolite concentrations.

2.2.2.11 Drug Treatment

Bortezomib (Lot Nr 10008822, Cayman chemicals), was dissolved in dimethyl sulfoxide (DMSO) as a vehicle and diluted to the desired concentration of the growth media directly before usage. In order to produce the EC values two different stock solutions were prepared, the first one with 600mM and diluted to 1000 μ M with 10x series dilution, the second one with 200mM stock and diluted to 312 μ M with 10x series dilution. A control media just containing the vehicle without any bortezomib was prepared for control purposes. In all cases, care was taken to keep the maximum final DMSO concentration below 0.01%. Prior to treatment, 90% of the volume was replaced with a bortezomib solution in media at a concentration that resulted in the final treatment concentrations. The determination of EC20, EC50 and EC80 was performed in the first step employing a broad range of drug concentrations (with a variation by a factor of 10 as explained previously). Experiments were run in quadruplicate for each condition. For 2D cells 96 well plates were used with 1000 cells as starting seeding number and treated after 24 hours. For 3D cells after formation and growth to an approximate diameter of 500 μ m the spheroids were transferred using cutted tips to 96well plates and treated with different EC doses for 2 days.

2.2.2.12 CellTiter-Glo® Luminescent Cell Viability Assay

A quantification of ATP was performed to measure the number of viable cells employing a CellTiter-Glo® Luminescent Cell Viability Assay. The advantage of using this assay is the possibility to perform it with both 2D and 3D cells, which aids in comparison. ATP is known to be an indicator of metabolically active cells. Doses for bortezomib in the range 0.0001 μ M-1000 μ M were applied to determine EC20, EC50 and EC80 for both 3D models and 2D cells. The required spheroids were generated from Ty82 and 1889c cell lines using simple rotation combined with 3D molds and co-culturing with matrigel. The 2D culture was performed with a seeding number of 10000 cells in 96well plates for both cell lines and a treatment time of 48 hours, with the same conditions being applied to 3D cell culture, too. A standard curve for ATP as well as the untreated control were employed as a reference for data normalization. First CellTiter-glo® reagent was prepared via adding the CellTiter-glo® buffer to CellTiter-glo®

MATERIAL AND METHODS

substrate. After the end of the treatment duration, the medium containing drug was discarded and cells were washed with 1x PBS one time. For the 2D cell culture, each well was diluted 1:1 with CellTiter-glo® reagent and medium and rotated for 10mins with 350rpm. Plates were kept in aluminium foil since the CellTiter-glo® reagent is light sensitive. After that, plates were read using a luminometer. The same procedure is repeated for 3D cell culture, but in addition the spheroid is diluted with the CellTiter-glo® reagent five times to ensure optimum results.

2.2.3 Laser Scanning Confocal Microscopy (LSCM)

In order to characterize the spheroid morphology and the drug effects, Calcein AM (viable cells marker), Ethidium homodimer EthD-1 (dead cells marker), Hoechst 33342 (apoptotic marker) dyes are used for live cells imaging with an incubation time of two hours for each spheroid. After reaching the desired final spheroid size for control and after finishing the treatment duration for treated spheroids each spheroid was washed with PBS three times to remove any old medium and then incubated for two hours with a mixture solution of the dyes prepared in the normal culture medium. For Calcein AM 1 μ M was used, 3 μ M for EthD-1 and 3 μ M for Hoechst 33342. After incubation with the dyes, spheroids were washed three times to remove any remaining dye solution and placed in fresh 500 μ l phenol red free medium. Samples were mounted on ring like structures during the measurements (see Figure 1) with same conditions as incubator (5%CO₂ and 37°C). Images were captured using a Leica TCS SP8 DLS confocal microscope and an LSM Olympus confocal microscope.

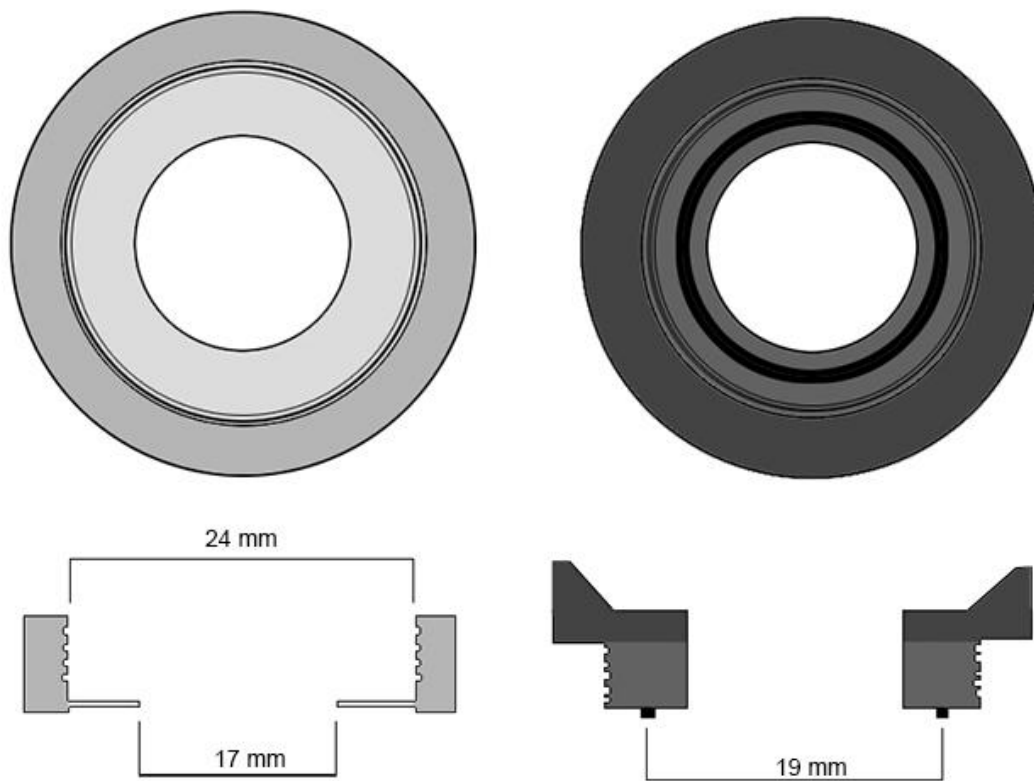


Figure 2.2.3. Home-made sample holder for live cell imaging.

2.2.4 Antibody staining

2.2.4.1 Fixation, Embedding and slicing

All spheroids were checked with a light microscope before the fixation step to ensure that they have clear and well defined edges. Starting with fixation, 500 μL PBS were pipetted per well in a 24 well plate. Spheroids were aspirated with a self-polished pipette, a 1000 μL pipette with cutted tips to be transferred in the 24 well plate and afterwards carefully washed with PBS three times followed by addition of 300 μL 4% paraformaldehyde (PFA) under the fume hood. The spheroids were left in PFA for at least 1 hour with gentle shaking using a rotating shaker, followed by PFA removal under the fume hood. Then the spheroids were washed three times with 500 μL PBS, then the plates were closed with parafilm and stored at 4°C until the next step. For embedding, PBS was removed and 200 μL eosin added to each spheroid (with a drop of glacial acetic acid) and incubated for 10 mins on a shaker at a speed of 100rpm. The aim of

MATERIAL AND METHODS

adding eosin is to visualize the spheroid later on during the cutting procedure. After 10mins all eosin was removed almost completely with some left with the spheroid to avoid dryness, then 500 μ L PBS was added to each well three times to wash any remaining eosin. Meanwhile 2% agarose/PBS were prepared and left to cool down. The spheroids washed from eosin were mixed with 200 μ L agarose in small eppis and mixed together gently under ice to solidify. After solidification the agarose containing the spheroids is put into embedding cassettes and the embedding machine is started overnight. The next day the cassettes were taken out of the machine and placed in heated compartments, embedded with paraffin in the pouring machine and then placed in a freezer for at least 3 hours before cutting each section with 4 μ m height using a microtome. Each slide is then placed in a template for further processing and stored at 4°C until staining.

2.2.4.2 Staining

Two different antibodies were used in this study, Ki-67 (D3B5) Rabbit mAb (Alexa Fluor® 488 Conjugate) antibody to check the proliferating area and distinguish between the core with other regions; and Cleaved Caspase-3 (Asp175) (D3E9) Rabbit mAb (Alexa Fluor® 488 Conjugate) as an apoptotic marker with standard staining by Fluoroshield™ with DAPI (4',6-Diamidin-2-phenylindol) to stain cellular nuclei. First the slides were incubated in Roti-histol for 5mins (2x) followed by rehydration with an alcohol gradient 100%,90%,80%,70% and 50% (1x) for 5mins then the slides were washed 2mins with distilled water. After the rehydration processes the slides were incubated with citrate buffer two times for 7 mins each in the microwave. After the incubation the slides were left at room temperature to cool down for 20-30minutes followed by washing 1x for 5mins in distilled water, then washed three times with 1xPBS each for 5minutes. Using a DAKO grease pencil the sections that contain the spheroid slices were drawn in circles followed by the addition of 5% blocking buffer in PBS to the slides and were left it for 2hours in the dark at RT. After that the slides were washed 3x 5mins in 1x PBS. Followed by incubation with antibodies with desired final concentration diluted in 1% blocking buffer with PBS overnight in the dark at 4°C. For Ki67 1:200 and Cleaved Caspase-3 1:50. The next day the slides were washed 3x 5mins in 1xPBS under gentle shaking under dark conditions. The staining with Fluoroshield™ with DAPI 4 drops to each slide, is carefully covered with cover slide and left at least for 2 hours to dry out before fluorescence imaging.

3 Results

3.1 Tissue metabolomics of thymic epithelial tumors (TETs): To identify altered metabolic signatures in aggressive TETs in order to open new targeted therapeutic options for nonresectable thymomas and thymic carcinomas.

3.1.1 ¹H NMR spectroscopy reveals 37 metabolites in TETs

Analysis of the 15 snap-frozen TETs using HRMAS ¹H-NMR spectroscopy (Figure 3.1.1.1) revealed 37 metabolites overall (Table 3.1.1.1), with their quantities depicted in Figure 3.1.1.2:

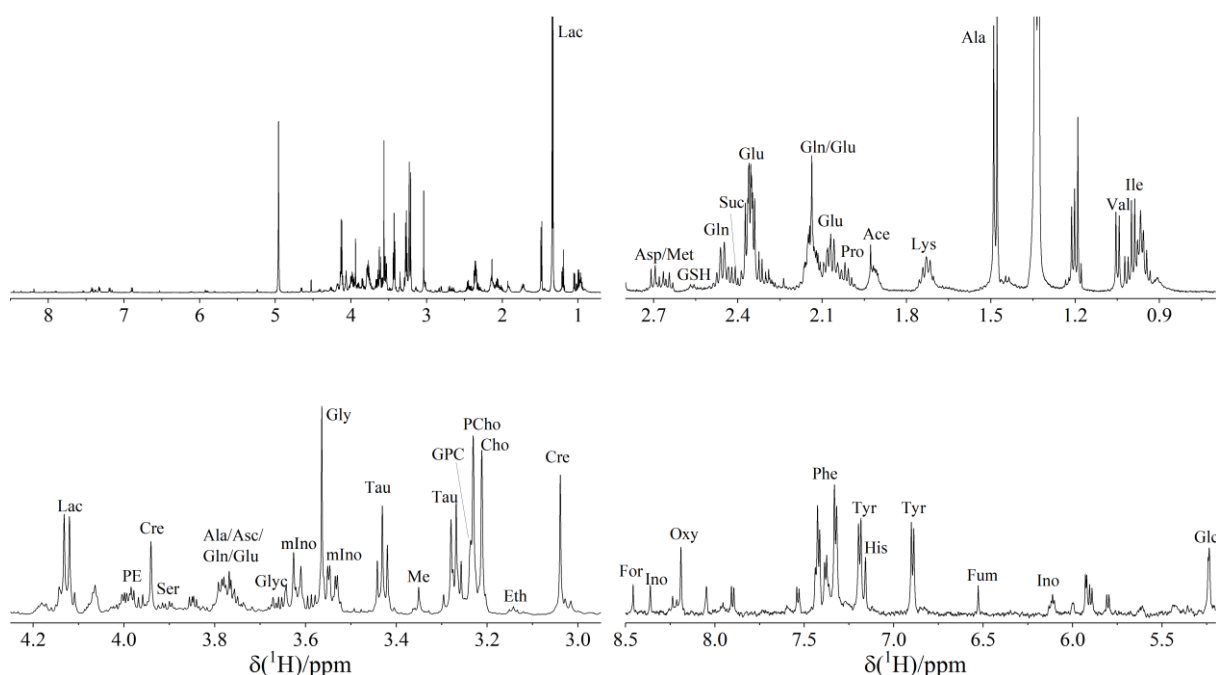


Figure 3.1.1.1 Representative HRMAS ¹H-NMR spectrum of a B2 thymoma measured at a tissue temperature of 4 °C and referenced to TSP. Abbreviations: Ace: acetate, Ala: alanine, Asc: ascorbate; Asp: aspartate, Cho: choline, Cre: creatine, Glc: glucose, Glu: glutamate, Gln: glutamine, GSH: glutathione, GPC: glycerophosphocholine; Gly: glycine, Ile: isoleucine, Ino: inosin, Lac: lactate, Leu: leucine, Lys: lysine, Met: methionine, mIno: myo-inositol; PCho: O-phosphocholine, PE: O-phosphoethanolamine, Phe: phenylalanine; Pro: proline, Ser: serine, Succ: succinate, Tau: taurine, Thr: threonine, Tyr: tyrosine, Val: valine (Part of these results were recently submitted for publication in *CANCERS*).

Results

Table 3.1.1.1 Metabolites detected in fifteen thymic epithelial tumors (TETs) using HRMAS ¹H-NMR spectroscopy. P-values and incidences (number of samples from a total of 15 cases, in which the respective metabolite could be detected) are given. P-values were determined by a Welch two sample t-test. Metabolites with significantly different expression levels between class A (indolent) and class B (aggressive) TETs are shown in bold (Part of these results were recently submitted for publication in *CANCERS*.).

Metabolite	p-value*	Incidence among 15 TETs	Metabolite	p-value*	Incidence among 15 TETs
Acetic acid	0.591	13	L-Isoleucine	0.909	11
L-Alanine	0.028	15	L-Lactic acid	0.046	15
Ascorbic acid	0.155	14	L-Lysine	0.605	9
L-Aspartic acid	0.172	11	Methanol	0.973	6
Choline	0.322	15	Glycerophosphocholine	0.235	15
Creatine	0.137	15	Acetylcholine	0.577	11
L-Cysteine	<0.0001	8	Phosphorylcholine	0.320	14
Ethanolamine	0.146	8	O-Phosphoethanolamine	0.590	12
Oxypurinol	<0.005	7	L-Phenylalanine	0.289	11
Fumaric acid	0.416	12	L-Proline	0.697	12
D-Glucose	0.175	10	L-Serine	0.284	13
L-Glutamic acid	0.207	14	Succinic acid	0.612	13
L-Glutamine	0.095	14	Taurine	0.454	15

Results

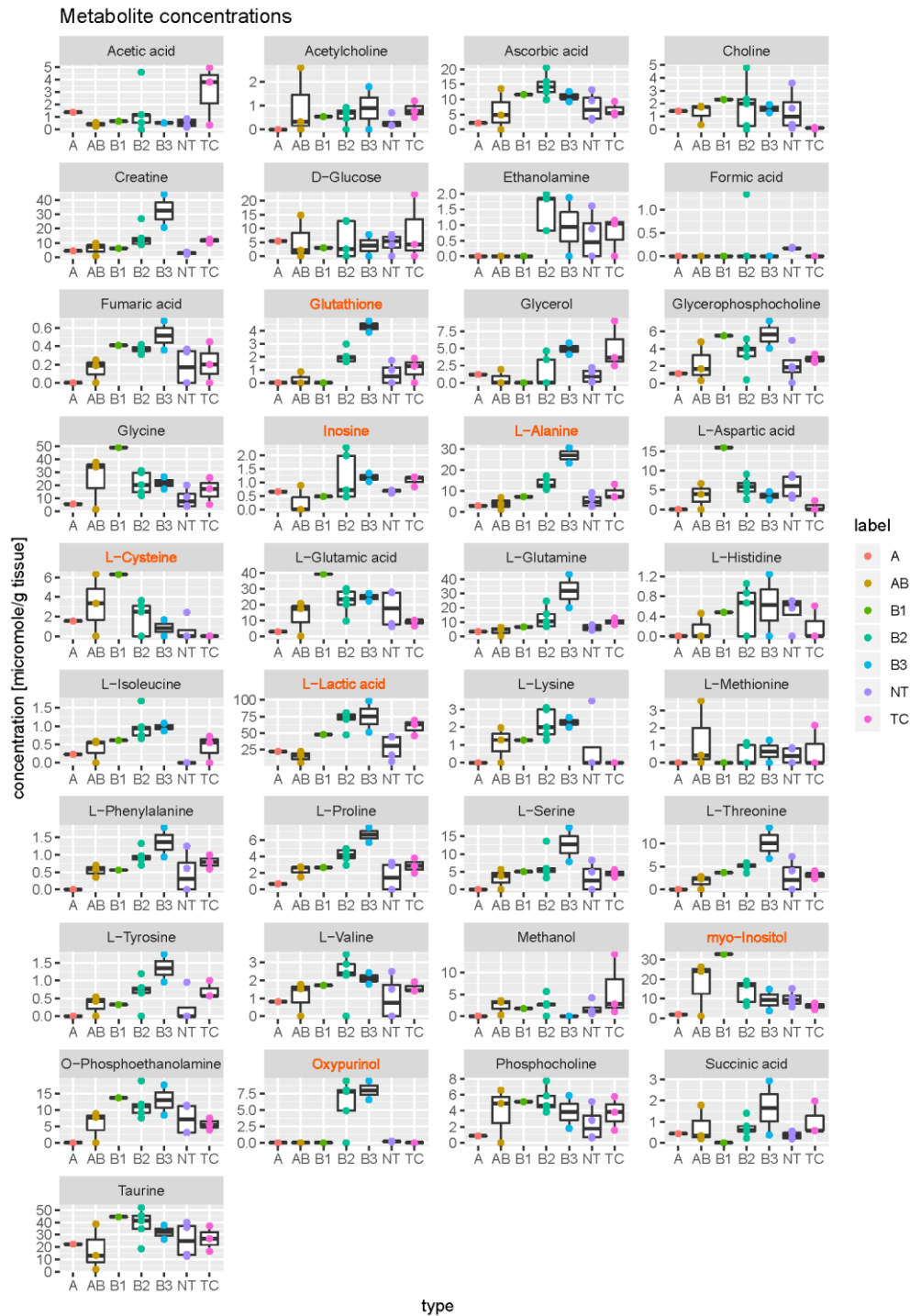


Figure 3.1.1.2 Boxplots showing the concentrations of the 37 metabolites found overall in thymomas (A, AB, B1, B2, B3, n=12), thymic carcinomas (TC, n=3) and normal thymi (NT, n=4). Due to the low number of cases in individual histological groups (n=1-4) no p-values are given. Metabolites with significantly different expression in indolent (A, AB, B1) and aggressive (B2, B3, TC) thymic epithelial tumors are highlighted in red/bold (Part of these results were recently submitted for publication in *CANCERS*).

Results

None of the 15 sample contained all 37 metabolites: 33 could be measured in 3 cases (all aggressive cases), 32 metabolites in 2 cases (1 indolent and 1 aggressive), 31 metabolites in 2 cases (1 indolent and 1 aggressive), while 8 cases (3 indolent and 5 aggressive) contained less than 31 metabolites. There was no correlation been histotype/aggressiveness and the number of detected metabolites.

3.1.2 Metabolic profiles are closely associated with the WHO histotypes of TETs

Unsupervised cluster analysis of the metabolite expression profiles of 14 of the 15 cases (from Table 3.1.1.1) resulted in the heatmap shown in Figure 3.1.2.1, which reveals clustering of the TCs together with the aggressive thymomas (B2 and B3). A third group comprises the indolent thymomas (A, AB, B1). All TETs cluster separately from non-neoplastic thymi.

Looking at individual metabolites, there were higher concentrations of oxypurinol, proline, alanine, choline and cysteine in aggressive thymomas compared to TCs. Furthermore, the cysteine to alanine ratio distinguished B3 thymomas from TCs, since B3 thymomas showed low levels of cysteine and high alanine levels, while TC showed even lower levels of both metabolites (Figure 3.1.2.1). No metabolite showed a consistently higher level in TCs than B2 and B3 thymomas; even high lactic acid levels that were typical of aggressive TETs were relatively lower in TCs (Figure 3.1.2.1).

Results

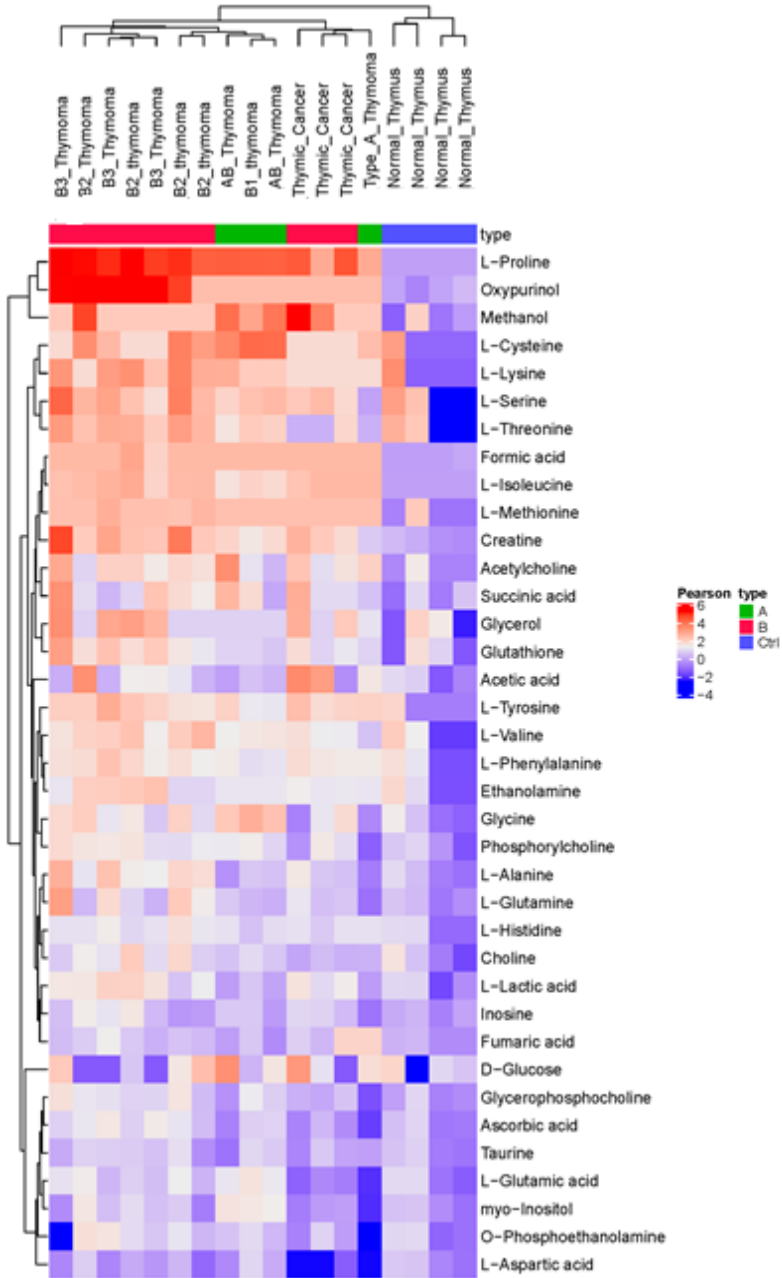
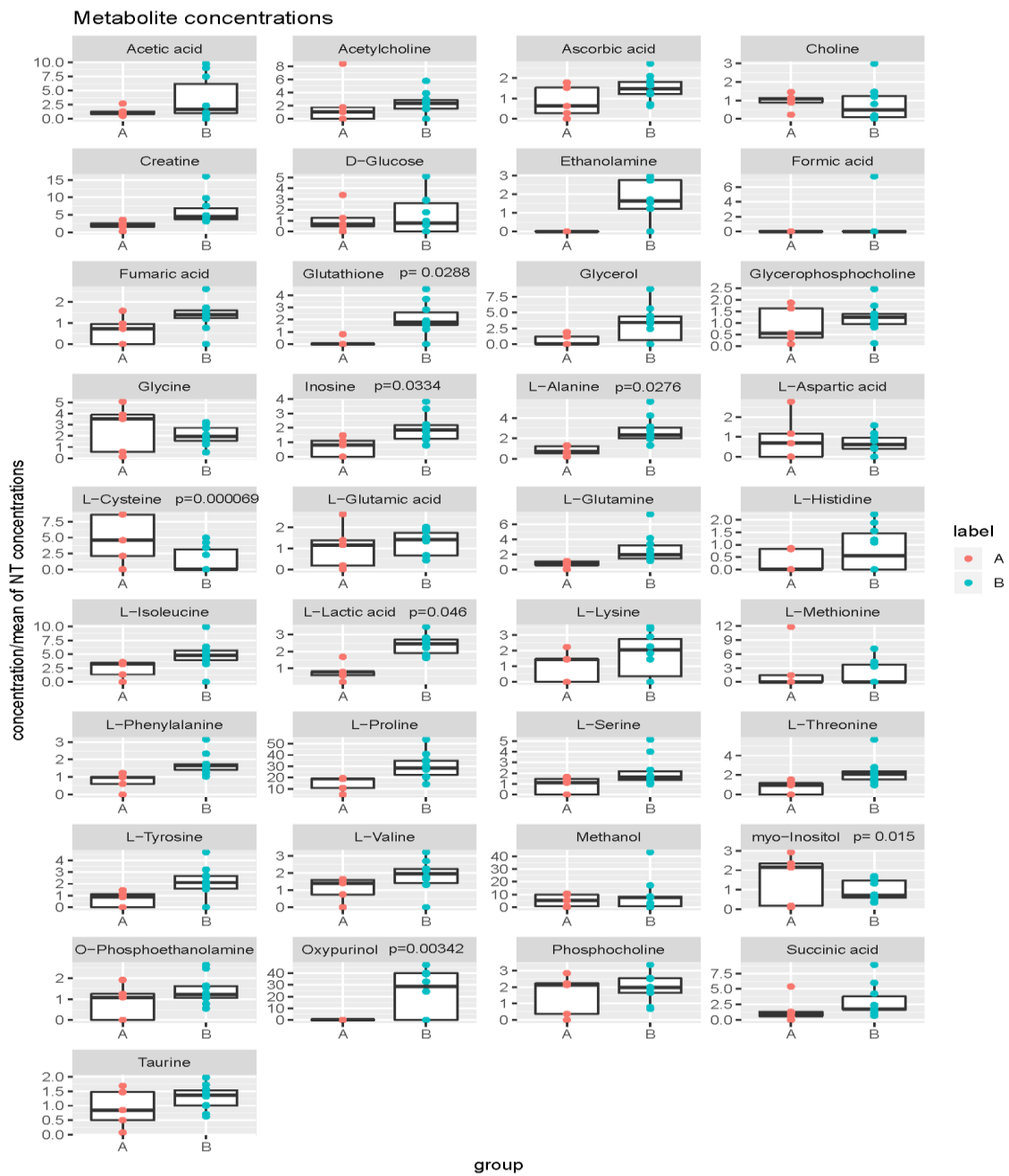


Figure 3.1.2.1 Heatmap with identified metabolites in thymic epithelial tumors (TETs): Hierarchical clustering analysis (HCA) was performed on 37 identified metabolites using Pearson correlation as the distance metric in 14 of the 15 TETs (1 A, 3 AB, 1 B1, 5 B2, 2 B3 thymomas and 3 thymic carcinomas, TC) and 4 non-neoplastic thymi (NT). One obvious outlier, an AB thymoma, was exempt from the analysis, since all its metabolite concentrations were extremely low or even zero. Note that aggressive thymomas (B2, B3 thymomas) and TCs form distinct clusters (Part of these results were recently submitted for publication in *CANCERS*).

Results

3.1.3 ¹H NMR spectral analysis discriminates ‘indolent’ from ‘aggressive’ TETs

Next compared the clinically important groups of indolent TETs (A, AB, B1 thymoma; group A, n=5), and aggressive TETs (B2, B3 thymomas and TCs; group B, n=10). Only seven of the 37 metabolites showed significantly different concentrations ($p < 0.05$; Welch two sample t-test) (Table 3.1.1.1, Figure 3.1.3.1).



Results

Figure 3.1.3.1 Boxplots of the concentrations of metabolites, normalized to the sum of normal thymi (NT) in groups of clinically indolent thymomas (A, AB, B1 thymomas, group A, red; n=5) and aggressive thymic epithelial tumors (TETs) (B2 and B3 thymomas and TCs, group B, green, n=10). P-values were determined with a Welch two sample t-test; significant differences are shown; non-significant p-values are given in Table 3.1.1.1. Higher levels of cysteine and myo-inositol were typical of indolent TETs, while higher levels of alanine, glutathione, inosine, lactic acid and oxypurinol were characteristic of aggressive TETs.

To identify the most relevant metabolite(s) for the distinction between the two groups, receiver operating characteristic (ROC) curves were generated, showing that cysteine, alanine and glutathione were the most discriminatory metabolites (AUC=1.0, 0.88 and 0.84 resp.) (Figure 3.1.3.2) (Part of these results were recently submitted for publication in *CANCERS*).

Results

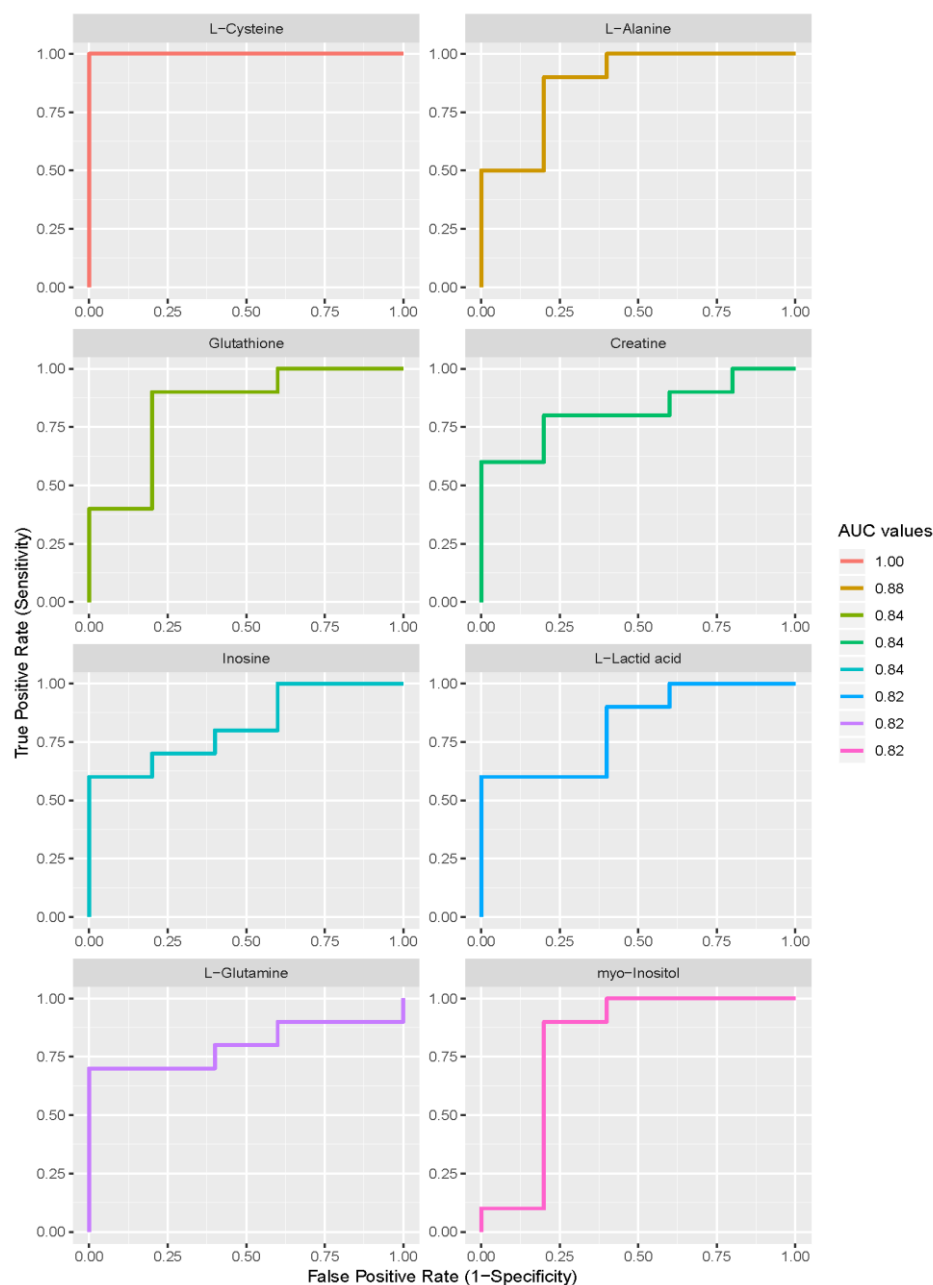


Figure 3.1.3.2 Receiver operating characteristic (ROC) curves for the metabolites cysteine, alanine, glutathione, creatine, inosine, alanine, lactic acid and myo-inositol, based on a grouping A= indolent thymomas and B=aggressive thymic epithelial tumors. The ROC curves of these metabolites show an “area under the curve” (AUC) value larger than or equal to 0.8.

3.1.4 ¹H NMR analysis reveals differentially activated metabolic pathways in TETs

When all metabolites (Table 3.1.1.1) detected in the 15 TETs were subjected to MetPA metabolic pathway analysis (Xia & Wishart, 2010), six “metabolite-based metabolic KEGG pathways” (Kanehisa et al., 2008) were predicted to be activated in the group of aggressive

Results

TETs (Table 3.1.4.1). In functional terms, these pathways imply an impact on transsulfuration, the homocysteine and tricarboxylic acid (TCA) cycles, the management of reactive oxygen species (ROS) and glycolysis (Table 3.1.4.1), i.e. on known tumor biological function. Surprisingly, not a single activated metabolic pathway was identified in the group of indolent TETs.

Table 3.1.4.1 “KEGG metabolite-based metabolic pathways” identified by the MetPA algorithm using 37 metabolites detected in the indolent group A (A, B1 and AB thymoma subtypes) and aggressive group B (B2, B3 and TC) thymic epithelial tumors. The first column lists the “key metabolite” associated with each enriched metabolic pathway. The assumed biological function associated with the given pathway is listed in column 3. P-values represent the differences in enrichment of the MetPA-derived “metabolite-based metabolic KEGG pathway” (column 2) between group A and group B TETs. “Impact” denotes the proportion of metabolites that are significantly changed in a given KEGG pathway (Part of these results were recently submitted for publication in *CANCERS*.).

Key metabolite	MetPA-derived KEGG pathway	Assumed Function	P-Value	Impact
Cysteine	Cysteine/methionine Metabolism	Transsulfuration Pathway	<0.001	0.22
Glycine	Glycine, serine and threonine metabolism	Homocysteine cycle	0.012	0.46
Glutathione	Glutathione metabolism	Redox state	0.013	0.37
Alanine	Alanine, aspartate and glutamate metabolism	TCA cycle	0.022	0.54
Lactate	Pyruvate metabolism	Glycolysis	0.029	0.14
Glutamine	Glutamine/glutamate metabolism	Glutaminolysis	0.032	0.50

3.1.5 Transcriptome-based metabolic pathways are differentially enriched in TETs

Due to the unavailability of an independent validation cohort of snap frozen TETs, I investigated whether the identified six metabolite-based metabolic KEGG pathways (Table

Results

3.1.4.1) are also enriched at the transcriptomic level using gene set enrichment analysis (GSEA) in the TCGA Thymoma dataset. This approach appeared reasonable since the transcriptomic data available from our cohort (n=15) suggested that it was fairly representative of the TCGA cohort (n=115) (Figures 3.1.5.1 and 3.1.5.2).

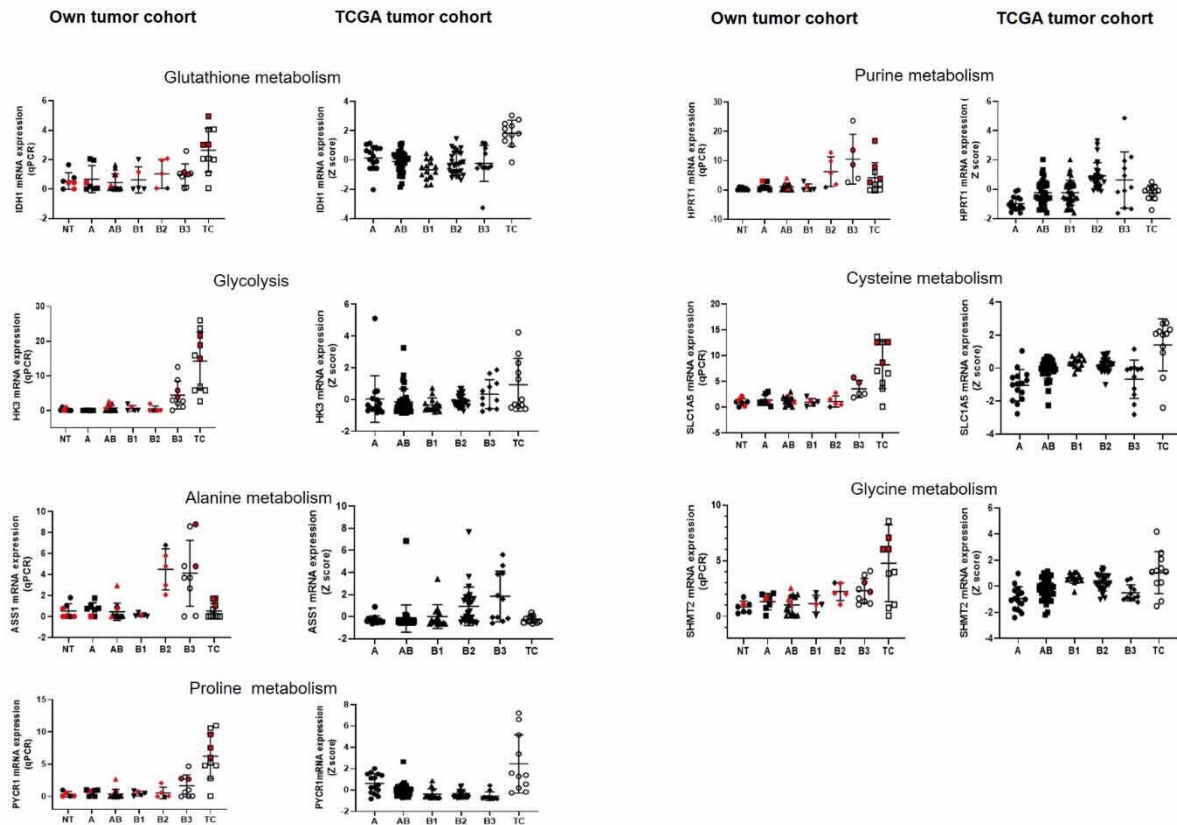


Figure 3.1.5.1 Transcriptomic profiles of 7 representative genes selected from each of the 7 metabolic pathway determined in 57 thymic epithelial tumors (TETs: A, AB, B1, B2 and B3 thymomas and thymic carcinomas, TC) including the 15 thymic epithelial that were studied by HRMAS-¹H NMR. Transcript levels were determined by qRT-PCR and compared to transcriptomic profiles of 115 TETs retrieved from the TCGA TET dataset. Note the strong similarity of the expression profiles in our current cohort and the TCGA cohort. Thymic epithelial tumors studied by HRMAS-¹H NMR are highlighted in red (Part of these results were recently submitted for publication in *CANCERS*).

Results

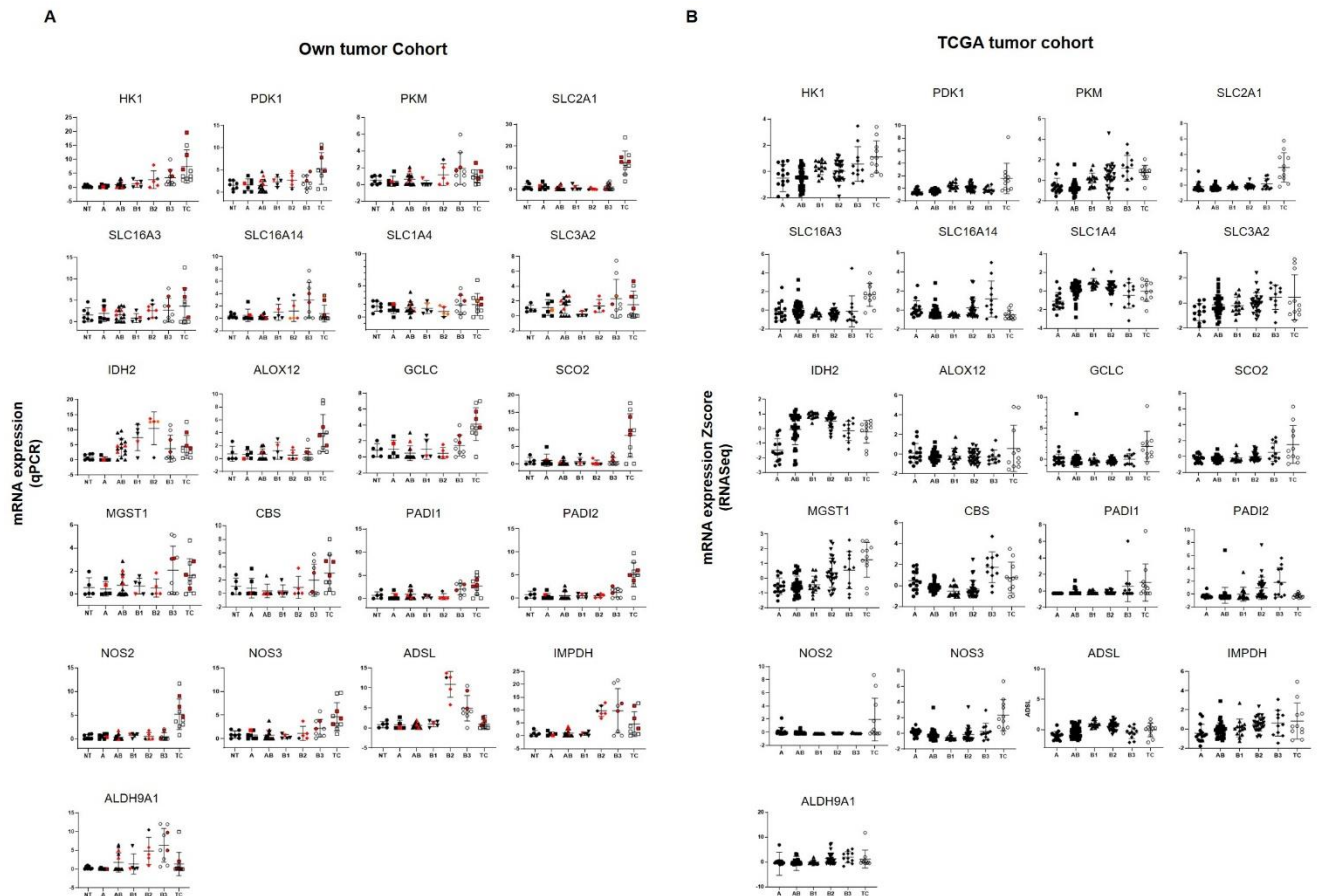


Figure 3.1.5.2 (a) Transcriptomic profiles of 21 additional genes selected from the 7 metabolic pathways and determined in the 15 thymic epithelial tumors (TETs: A, AB, B1, B2 and B3 thymomas and thymic carcinomas, TC) that were studied by HRMAS-¹H NMR. Transcript levels were determined by qRT-PCR (b) Transcriptomic profiles of 117 TETs retrieved from the TCGA TET dataset (Part of these results were recently submitted for publication in *CANCERS*).

Due to the paucity of associated genes ($n=5$), GSEA (Radovich et al., 2018) was not applicable for the D-Glutamine/D-Glutamate pathway. Since MetPA analysis did not identify pathways linked to the highly expressed metabolites, oxypurinol and proline (Table 3.1.4.1), I selected the KEGG purine metabolism pathway (hsa00230), and arginine and proline pathway (hsa00330) as obvious candidates for GSEA. Of the seven metabolic pathways finally compared between the indolent and aggressive TET groups (Table 3.1.5.1), six showed a significant enrichment or a strong trend: glycolysis, the TCA cycle (FDR <0.01); purine metabolism and the alanine/aspartate/glutamate pathway (FDR <0,02); and glutathione metabolism (FDR=0.052) and arginine/proline metabolism (FDR=0.109).

Results

Table 3.1.5.1 “KEGG transcriptome-based metabolic pathways” retrieved from the TCGA thymic epithelial tumor (TET) database (Radovich et al., 2018) applying the DAVID enrichment analysis tool to 53 genes with significantly ($p < 0.05$) different expression between indolent group A (A1, AB, B1 thymomas) and aggressive group B TETs (B2, B3 thymomas; thymic carcinomas). The seven selected pathways include five KEGG pathways predicted from $^1\text{H-NMR}$ spectroscopy-based metabolite profiling and two pathways selected ‘manually’ (hsa230, hsa330) assuming they may cover the highly expressed metabolites, oxypurinol and proline.

The seven representative genes for each metabolic pathway are highlighted in bold (Part of these results were recently submitted for publication in *CANCERS*).

Results

Key metabolite(s)	KEGG Pathways	KEGG-ID	P-Value	Fold Enrichment	FDR	Genes
Glutathione	Glutathione metabolism	hsa00480	1.3E-9	25.3	1.9E-08	GSTK1, GCLC, GGT6, GPX4, ANPEP, IDH1 , 2, MGST1, MGST2, LAP3
Alanine	Alanine, aspartate and glutamate metabolism	hsa00250	1E-7	28.7	1.1E-11	ALDH4A1, ADSL, FOLH1, GOT1, RIMKLA, NIT2, ASS1
Proline	Proline and arginine metabolism	hsa00330	2.9E-11	28.7	5.80E-10	ALDH4A1, GOT1, P4HA1, NOS2, NOS3, ARG1, PYCR1 , LAP3, PRODH, ALDH9A1
Glucose and lactic acid	Glycolysis / Gluconeogenesis	hsa00010	5.30E-06	15	3.9E-05	HK3, PKM , ALDOA, FBP1, PCK2, HK1, ALDH9A1, SLC2A1, SLC16A3, SLC16A14
Oxypurinol	Purine metabolism	hsa00230	4.8E-04	89,6	3.2E-03	NT5C3A, ADCY10, ADSL, PKM, PNP, IMPDH1, NUDT2, HPRT1 , DCK, GART
Glycine	Glycine, serine and threonine metabolism	hsa00260	2.30E-03	14.7	1.10E-03	SDS, SHMT2 , CBS, PSPH
Cysteine	Cysteine and methionine metabolism	hsa00270	2.10E-03	15.1	1.10E-03	SDS, GOT1, MDH1, CBS, SLC1A5 , SLC3A2

Results

aggressive TETs in the seven metabolic pathways (Table 3.1.5.1). While generally confirming the GSEA results, the arginine/proline metabolism pathway was found to be significantly enriched in the group of aggressive TETs as well (Table 3.1.5.1).

3.2 Investigation of the metabolism of a 3D cell culture model with time and spatial resolution under viable conditions: Application of a new flow NMR technique

The currently available methods to investigate metabolic processes in small 3D models (e.g. tumor cell spheroids) have the disadvantage to provide a “snap-shot” of the metabolic state at a selected time point and to be destructive, i.e. to require dissection of a spheroid to gain 3D Information. Accordingly, a measurement at another time point so far has require the selection of another spheroid. In order to enable me to perform non-invasive and, therefore, repetitive metabolic profiling over extended periods of time in the same tumor cell spheroid as a function of spatial position and time in the context of in vitro toxicology studies, I developed a novel Nuclear Magnetic Resonance (NMR) measurement technique that has a resolution of 100 μm (while typical spheroid here had diameters between 350 and 860 μm . The technical details of this new, non-destructive technique are given in “Materials and Methods”, chapter 2.2.2.8. To keep individual spheroids viable during the NMR investigations that lasted for several days, a flow system maintained ‘physiological’ conditions (including cell culture medium at 37°C and at incubator-equivalent CO₂ pressure).

To show that the new method can monitor dynamic metabolic changes in a single spheroid over time, I performed NMR measurements of spheroids that were generated with the NUT carcinoma cell line, Ty82. Spheroids were kept over a period of 20 h in fresh, flowing medium, followed by a period of 92 h of stopped flow (Reprinted with permission from Anal. Chem. 2021, 93, 40, 13485–13494, doi: 10.1021/acs.analchem.1c02221, Publication Date:September 3, 2021, Copyright 2021 American Chemical Society.).

Figure 3.2.1.1a-c show the time course of all determined metabolites. It was found that during the period of medium supply all metabolite concentrations remained either constant or increased, which was likely a consequence of spheroid growth.

Results

After the flow was stopped, a decrease of the glucose level and an extraordinary increase of the lactic acid concentration was observed (cf. Figure 3.2.1.1a). This was in accordance with the expectation that the energy metabolism of Ty82 cells continued to consume glucose, although the glucose concentration was no longer kept constant by the medium flow, while hypoxia accompanying the stopped medium flow fostered anaerobic glucose conversion into lactic acid. Most of the other metabolite concentrations started to decrease immediately after the stop of medium flow, while others stayed constant for some time before decreasing, and still others showed virtually no changes. The latter metabolites are summarized in Figure 3.2.1.1c). The reduced nutrition supply in combination with the hypoxic and increasingly acidic (lactic acid-rich) environment, clearly altered the metabolism of TY82 cells grown as spheroids. However, whether the decrease of most metabolites was due to consumption by the tumor cells or by diffusion into the surrounding, non-replenished medium, remains unresolved. The described differences can also be appreciated if the initial and final NMR spectra are compared (cf. Figure 3.2.1.1d). For example, the NMR signals of phosphocholine, glutamine and alanine had almost vanished at the end of the experiment, while the intensity of the lactic acid resonance at 1.32 ppm had more than doubled.

In conclusion, this proof-of-principle experiment showed that time-resolved NMR quantification of many metabolites can be achieved with a single, non-manipulated spheroid during an investigational period of almost 5 days. Therefore, this system appeared appropriate to investigate the impact of pharmacological interventions on the metabolism of cancer cells as described in the next chapter, 3.3. (Reprinted with permission from *Anal. Chem.* 2021, 93, 40, 13485–13494, doi: 10.1021/acs.analchem.1c02221, Publication Date: September 3, 2021, Copyright 2021 American Chemical Society.)

Results

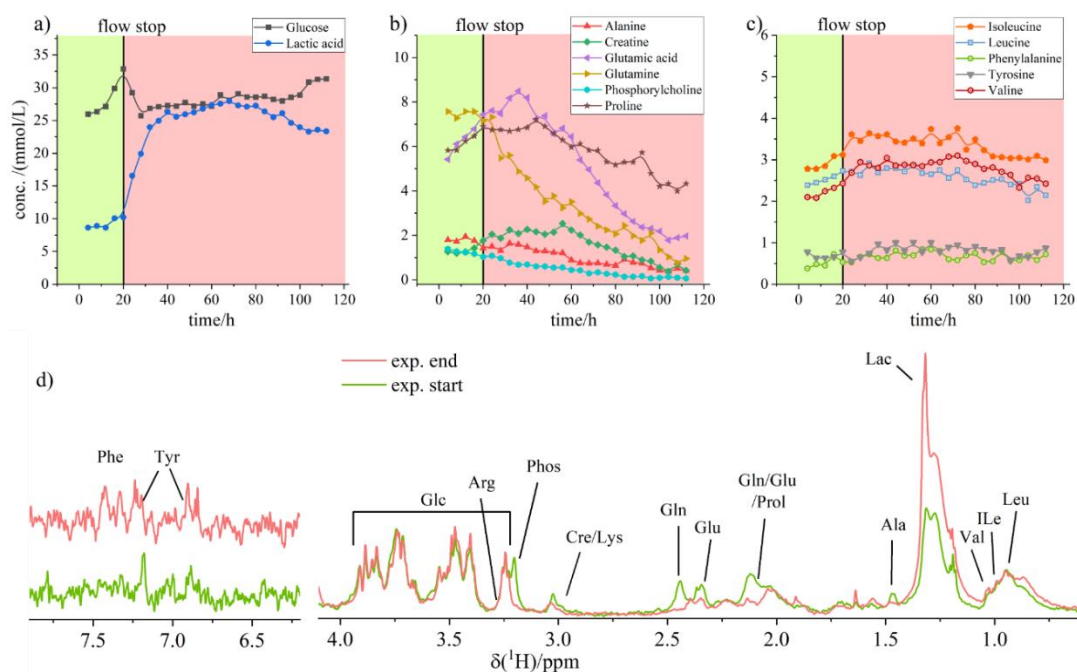


Figure 3.2.1.1: Results from spatial resolved NMR experiments on a single Ty82 spheroid (diameter of 700 μm) acquiring 24 slices (each slice measured for 4 h) up to a total time of 112 h, with the medium flow being stopped after 20 h. (a-c) Time dependence of the metabolite concentrations. (d) ^1H NMR spectra composed of 14 added single slice spectra at the start (green) and end (red) of the overall experiment. Phe: phenylalanine, Tyr: tyrosine, Glc: glucose, Arg: arginine, Phos: phosphocholine, Cre: creatine, Lys: lysine, Gln: glutamine, Glu: glutamic acid, Prol: proline, Ala: alanine, Lac: lactic acid, Val: valine, ILe: Isoleucine, Leu: leucine (Reprinted with permission from *Anal. Chem.* 2021, 93, 40, 13485–13494, doi: 10.1021/acs.analchem.1c02221, Publication Date: September 3, 2021, Copyright 2021 American Chemical Society.)

Having shown, that the measurement of metabolites in a single spheroid is possible over long periods of time (see above), I next wondered whether the spatial resolution of the radial metabolic profiles delivered by the new NMR technique are sufficient to reveal metabolic differences between the periphery and the core of single spheroids. For three spheroids of diameters of 600, 700 and 860 μm light microscopy images and radial metabolic profiles were compared (Figure 3.2.1.2).

Results

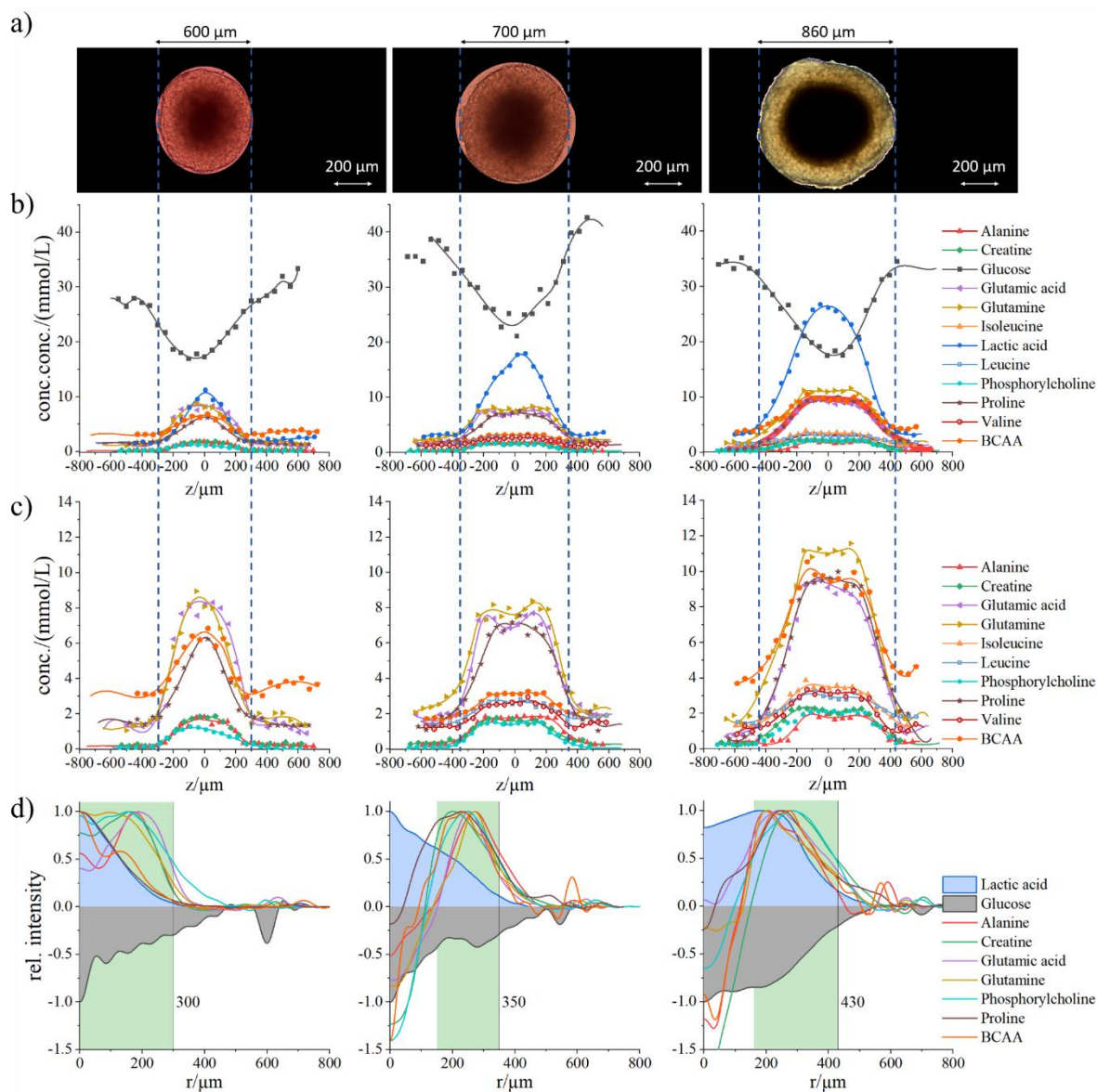


Figure 3.2.1.2 (a) Light-microscopy images of three measured spheroids aligned to the spatially resolved intensity profiles of identified metabolites shown in (b) and in the expansion in (c). In (d) the radial distribution of each metabolite is given calculated via double Abel inversion of data shown in (b) and (c). Lactic acid (blue) and glucose (grey) profiles are emphasized. Branched chain amino acid (BCAA) are just available as a sum signal and represent the sum of the concentrations of isoleucine, leucine and valine. (Reprinted with permission from *Anal. Chem.* 2021, 93, 40, 13485–13494, doi:

10.1021/acs.analchem.1c02221, Publication Date: September 3, 2021, Copyright 2021 American Chemical Society.)

I found minimal concentrations of most metabolites in the cores of spheroids, whereas concentrations of lactic acid were mostly high in the respective cores (Figure 3.2.1.2). In the smallest spheroid (diameter 600 μm) only the innermost core was depleted of glucose, with an almost linear increase to the outer shell (reflecting the glucose gradient in that spheroid). For the spheroid of 700 μm diameter, the area of glucose depletion was 50 μm wider, while for the largest spheroid (diameter 860 μm) it spread over 500 μm . High lactic acid and low glucose levels in the core combined with low lactic acid levels and high glucose levels in the outer shell suggest that hypoxic conditions in the core and either viable or proliferative activity hold in the outer shell. To get to know, whether cells in the outer shell of Ty82 cell-derived spheroids are viable or show proliferative activity, I investigated spheroids with an established dye labeling for viable cells, i.e. intact nuclei (4',6-Diamidin-2-phenylindol, DAPI, blue) and with an antibody to the proliferation-associated Ki-67 antigen (D3B5) Rabbit mAb, green). The results for two spheroids with diameters of 600 and 750 μm are shown in Figure 3.2.1.3. Analyzing spheroids with DAPI for intact nuclei showed that their distribution was uniform throughout in the 600 μm spheroid, while the core area of the 750 μm spheroid exhibited a less dense central distribution probably caused by hypoxia-induced necrosis. This results is in perfect agreement with our NMR based approach, where depletion of the majority of spheroids and lactic acid enrichment was found in the center of spheroids larger than 600 μm , while comparably high central metabolic concentrations in the 600 μm spheroid agree with the homogenous intact cell nuclear density found via staining. The proliferation marker, Ki67 showed intense fluorescence in a shell area with a width of approximately 200 μm in both spheroids. While a small inner domain of decreased fluorescence was detected in the 600 μm spheroid, almost no proliferation was detected in a large core area of the 700 μm spheroid coinciding with the region, in which numbers of intact nuclei were reduced.

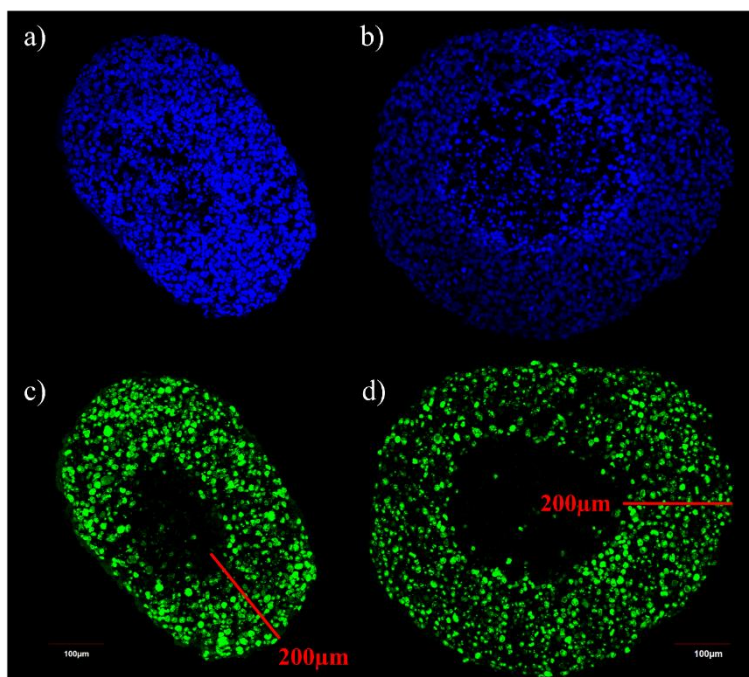


Figure 3.2.1.3 Identification of viable cells (DAPI(+)) as compared to proliferative (Ki67(+)) cells in spheroids of different size generated from Ty82 NUT carcinoma cells. In (a) and (b) confocal microscopy fluorescence pictures are shown of spheroids with diameters of 600 and 750 μm , respectively, using DAPI (4',6-Diamidin-2-phenylindol, staining nuclei blue). (c) and (d) are results of the identical slices using the proliferation marker Ki-67 (D3B5) Rabbit mAb (Alexa Fluor[®] 488 Conjugate). (Reprinted with permission from *Anal. Chem.* 2021, 93, 40, 13485–13494, doi: 10.1021/acs.analchem.1c02221, Publication Date: September 3, 2021, Copyright 2021 American Chemical Society.)

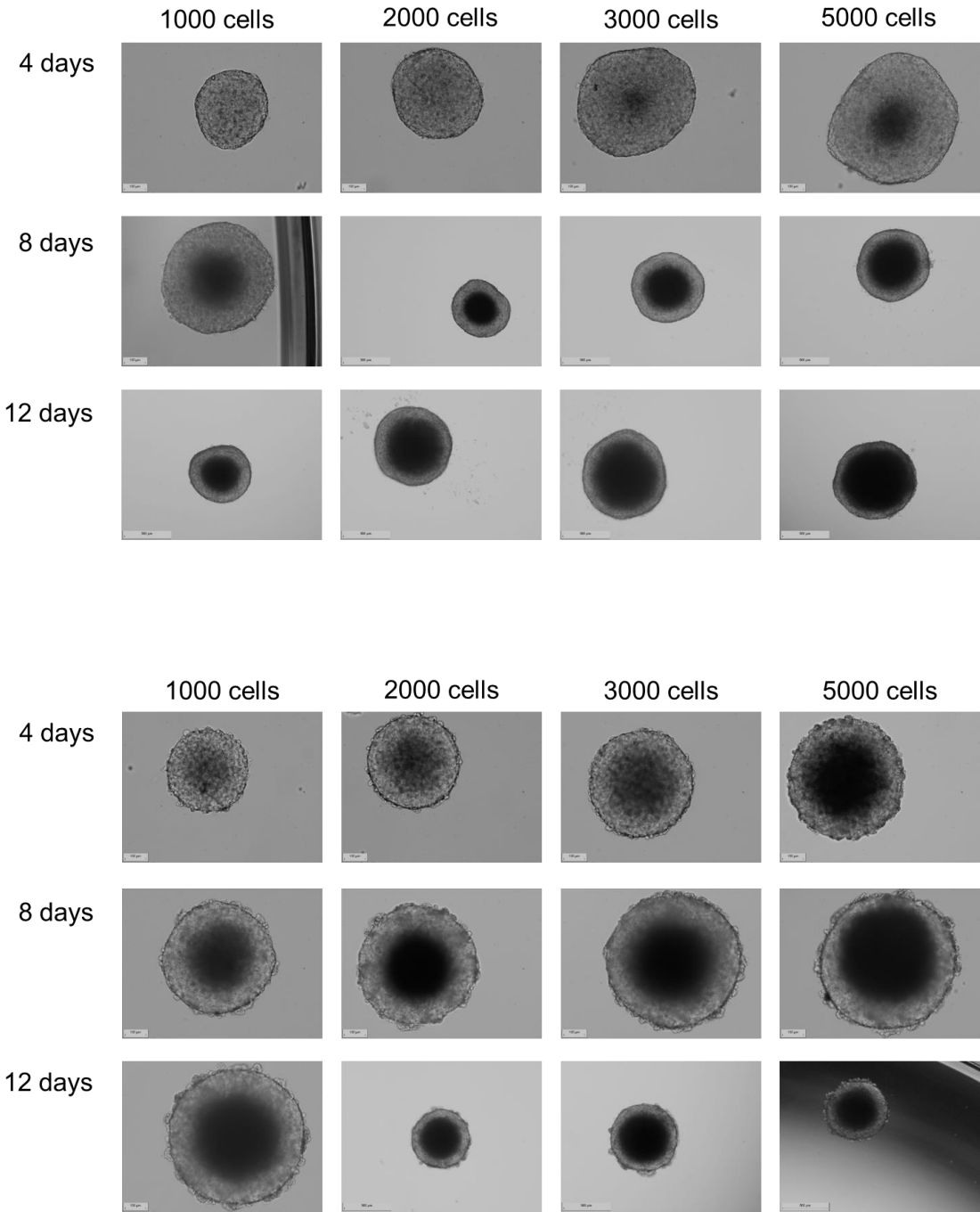
3.3 Production of 3D cell culture with two new techniques and characterization of the spheroids obtained

3.3.1 Preparation of spheroids

Using the techniques described in detail in the “Materials and Methods” chapter, spheroids were reproducibly prepared with the two cell lines, Ty82 and 1889c, reaching the aims of symmetrical spheres, i.e. round slices required for NMR measurements. The size could be improved both by changing the cell number and the growth rate. Spheroids were used to study drug resistance and metabolic profiles (for both see chapter 3.4). Figure 3.3.1.1 shows Ty82

Results

spheroids grown in serum-rich medium, in which they showed higher growth rates but imperfect roundness as compared to spheroids grown in a serum-poor medium (Figure 3.3.1.1). Spheroids were found to grow bigger under serum-rich (TMTS) than under serum-poor (TTS) conditions (Figure 3.3.1.1). Figure 3.3.1.2 shows the characterization of Ty82 spheroids with confocal microscopy using staining with 10 μ M Hoechst to visualize nuclei and nuclei fragmentation, EthD-1 as a marker for dead cells and calcein AM as a marker for viable cells. On the other hand, Figure 3.3.1.3 shows a staining for proliferating and apoptotic cells for spheroids from 1889c and Ty82 cells.



Results

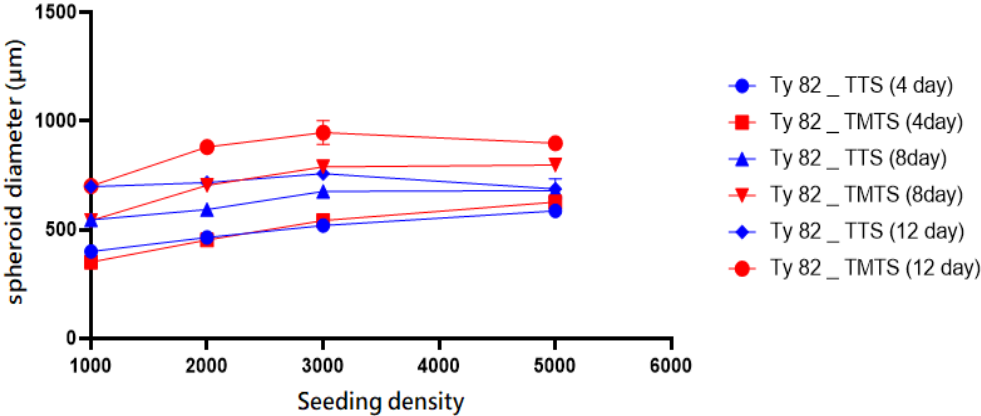
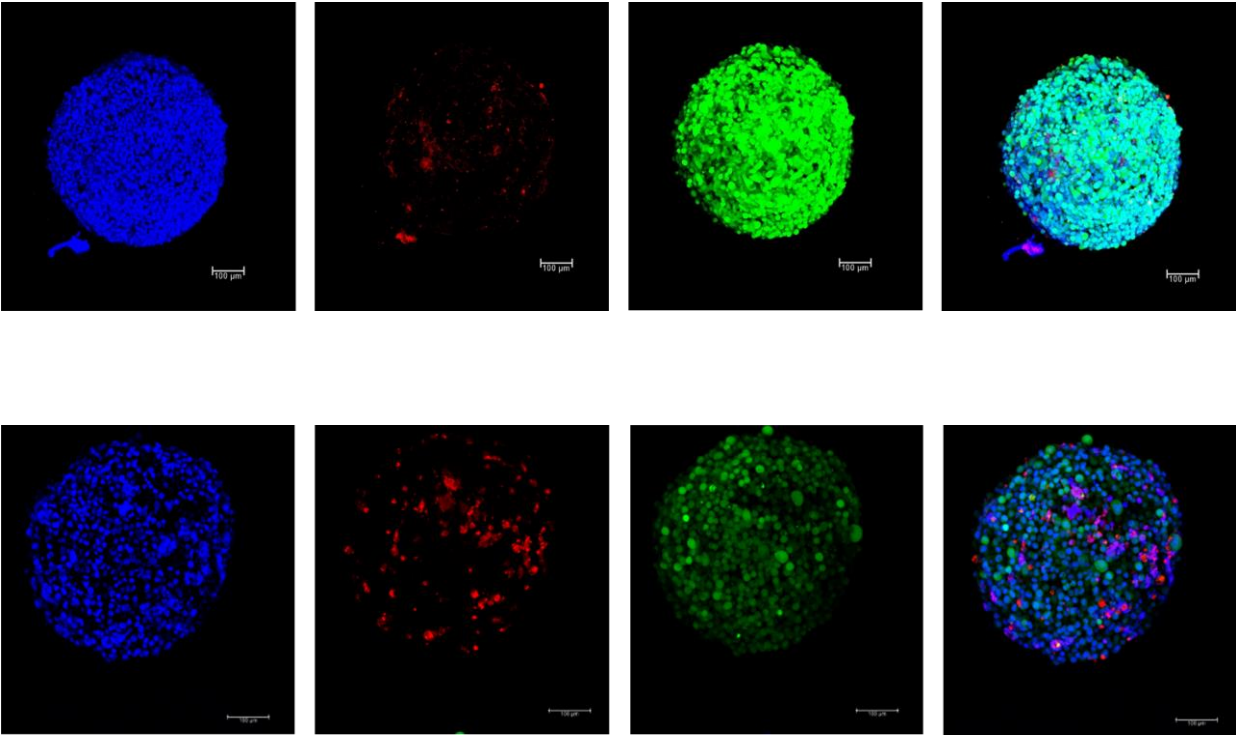


Figure 3.3.1.1 (Top) Images of Ty82 spheroids grown in serum-rich (TMTS) media. (Middle) Images of spheroids grown in serum-poor (TTS) media. (Bottom) Spheroid diameter of Ty82 cells as a function of seeding density, comparing growth in serum-rich (TMTS) and serum-poor (TTS) media and culture periods of 4, 8 and 12 days.



Results

Figure 3.3.1.2 Confocal microscopy image of untreated Ty82 spheroids (Serum poor/rich) stained with a combination of three dyes: 10 μ M Hoechst to visualize nuclei and nuclei fragmentation (Left), 2 μ M EthD-1 as a marker for dead cells (Middle left), 1 μ M calcein AM for viable cells (Middle right), and a merged image (Right). Images were taken using a Leica TCS SP8 DLS, and a maximum projection was applied to the 3D-stack with 1 μ m intervals. Scale bars represent 100 μ m.

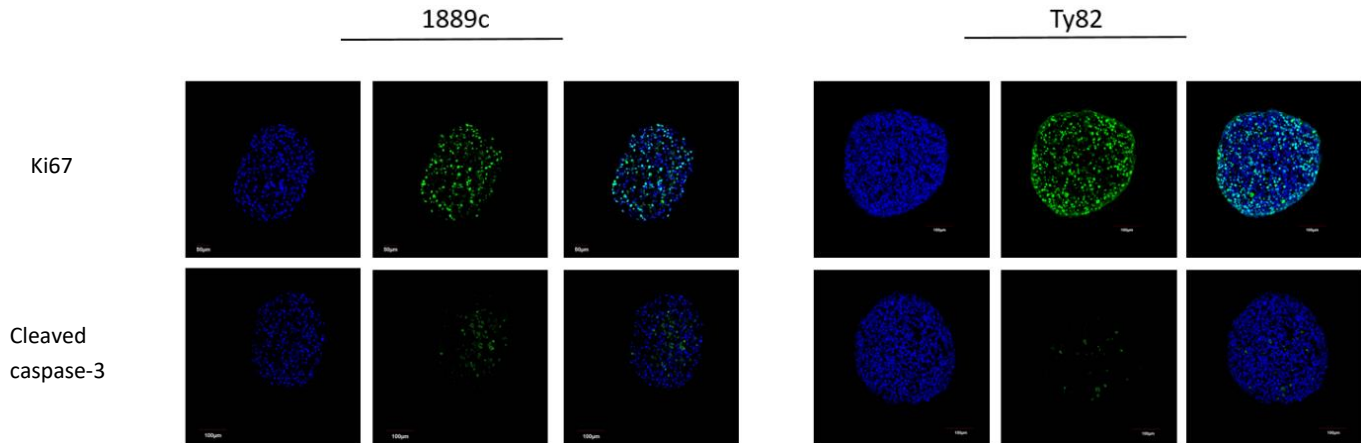
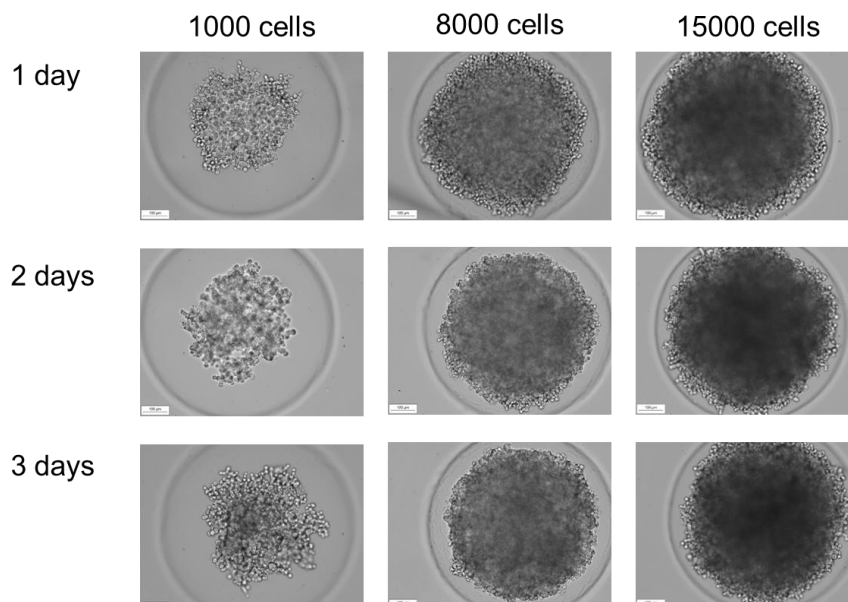


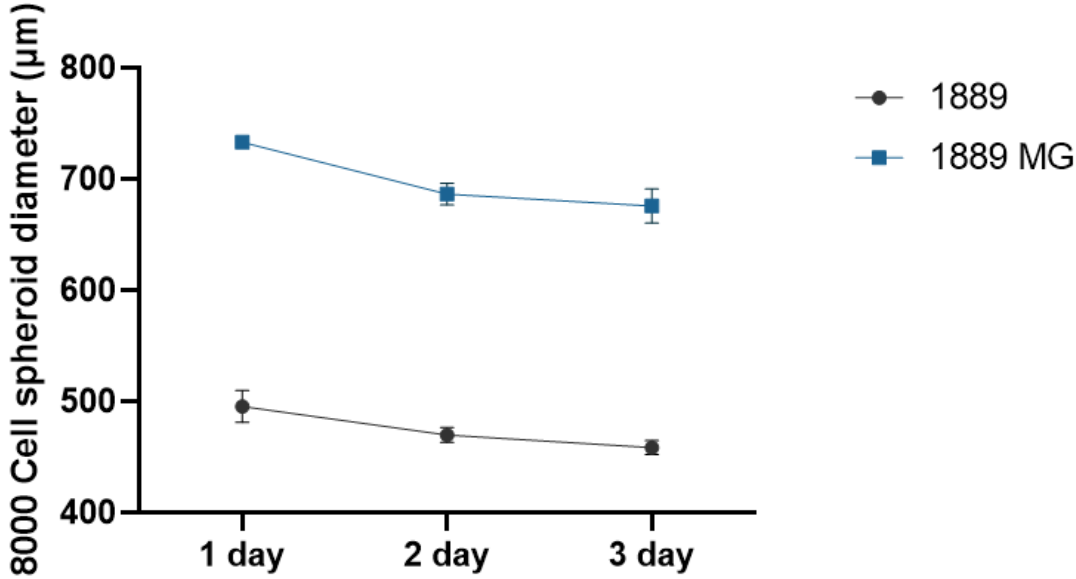
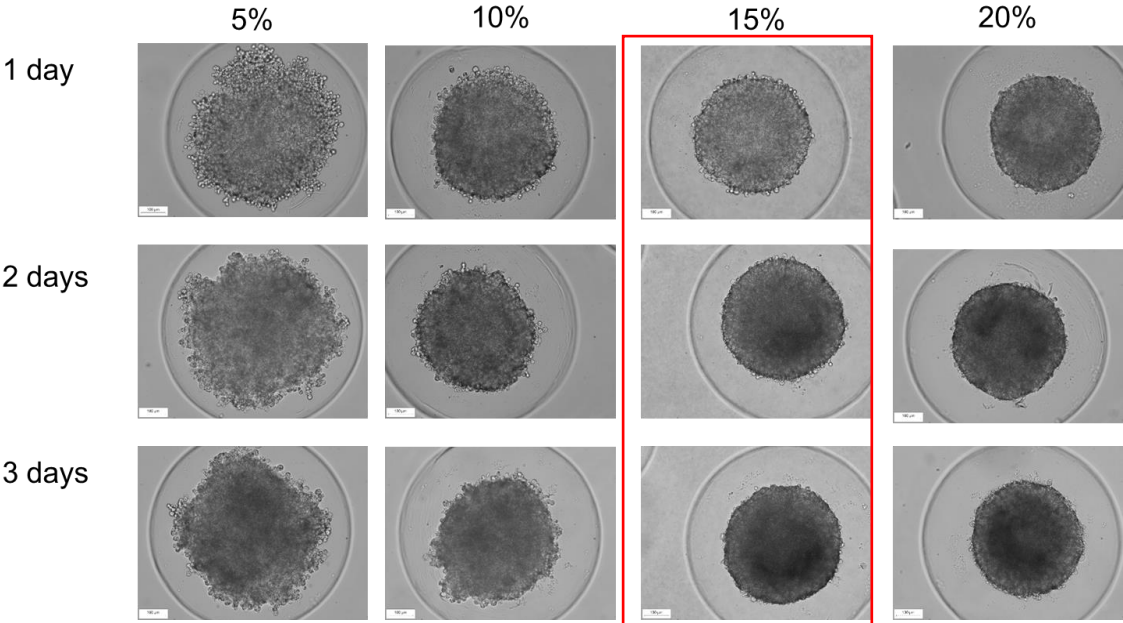
Figure 3.3.1.3 Characterization of 1889c (left) and Ty82 (right) spheroids using Ki67 (top row) and cleaved caspase-3 antibody (bottom row). Confocal microscopy fluorescence images are shown using DAPI to stain cellular nuclei (blue), Ki67 to stain the proliferating cells (green) and cleaved caspase-3 as an apoptotic marker (green).

A combination of 3D molds with matrigel resulted in reproducible 3D models of 1889c cells, with optimum growth conditions found for 15% matrigel (Figure 3.3.1.4). For purposes of comparison, 1889c spheroids were also grown in microtissue molds, but without applying matrigel, for seeding numbers of 1000, 8000 and 15000 cells (Figure 3.3.1.4). As shown in Figure 3.3.1.4, removal of serum reduced the compactness of 1889c derived spheroids. Spheroid size and shape were daily controlled under the microscope to check the roundness and compactness of the spheroids developing.

Normal media (molds)



Normal media Molds & Matrigel



Results

Figure 3.3.1.4 (Top) 1889c spheroids grown in microtissue molds, without matrigel, with seeding numbers of 1000, 8000 and 15000 cells. The combined use of microtissue molds and matrigel resulted in reproducible 3D models of 1889c cells that showed optimal growth (Middle) 1889c cells grown in microtissue molds and in the presence of various proportions of matrigel (5, 10, 15 and 20%) starting with 8000 seeding cells (Bottom) Comparison of spheroid formation and size in either the absence or presence of matrigel.

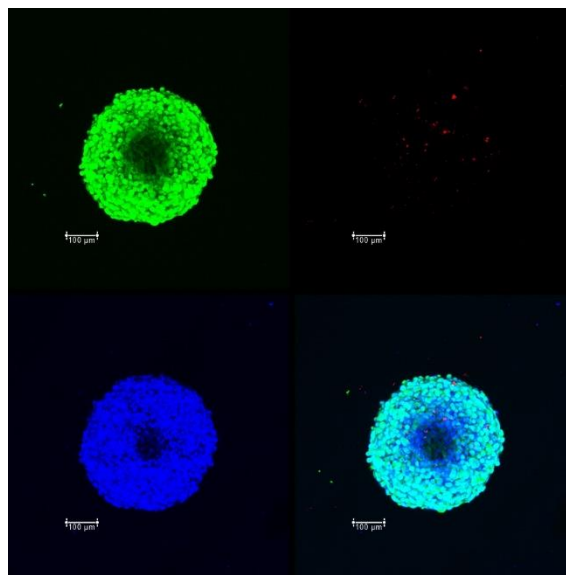


Figure 3.3.1.5 Confocal microscopy image of untreated 1889c spheroids (Serum rich) stained with a combination of three dyes: 10 μM Hoechst to visualize nuclei and nuclei fragmentation (Blue bottom Left), 2 μM EthD-1 as a marker for dead cells (Red top right), 1 μM calcein AM for viable cells (Green Top left), and a merged image (bottom right). Images were taken using a Leica TCS SP8 DLS, and a maximum projection was applied to the 3D-stack with 1 μm intervals. Scale bars represent 100 μM .

Spheroid size of 1889c cells increased after removal from 3D microtissue molds as shown in Figure 3.3.1.5A using 24 well ultra low attachment plates. On the other hand, spheroids tended to attach to the bottom of the well when using normal plates as shown in Figure 3.3.1.5B. In order to check the viability of the 1889c cells, they were stained with CalceinAM

Results

(Green) for viable cells and Ethd-1 (Red) for dead cells followed by confocal microscopy as shown in Figure 3.3.1.5.

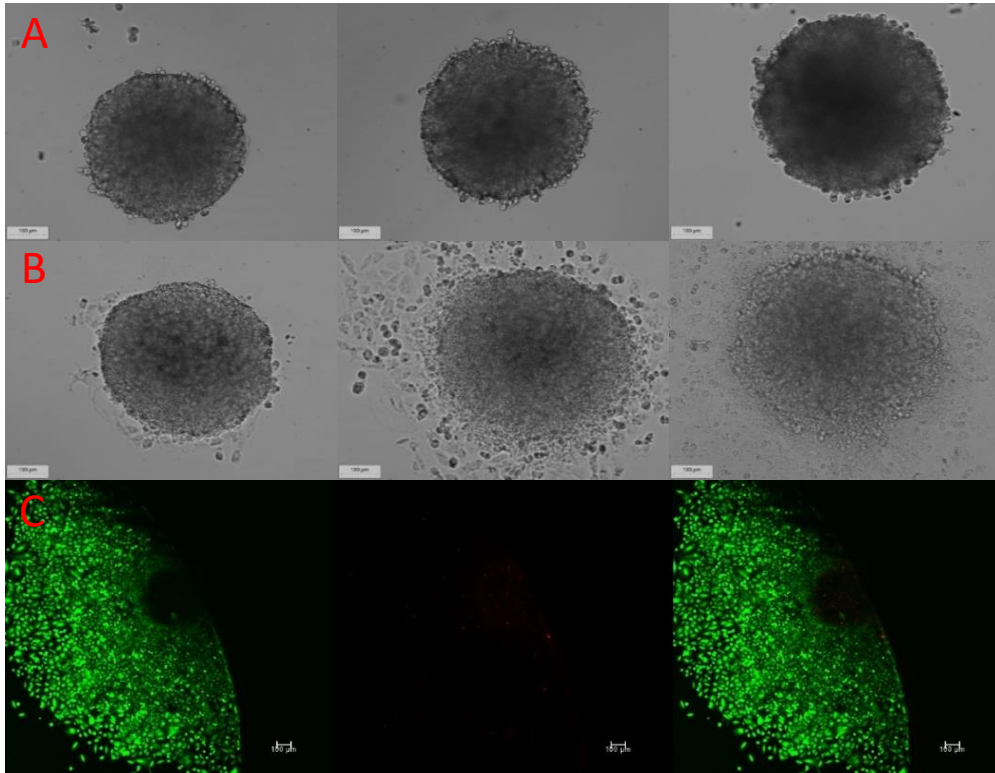


Figure 3.3.1.6 A) Spheroidal growth of 1889c cells after 5, 6 and 8 days (from left to right) using Ultra Low Attachment plates. B) Spheroidal attachment to the bottom using normal plastic plates. C) Confocal imaging to check the viability of cells from the spheroid. Green reflects viable cells and red reflects dead cells.

In order to check the importance of serum for 3D culture of 1889c cells, the cells were cultured in both serum poor and serum rich medium. It turned out, that 1889c spheroids grown in serum rich medium showed a better roundness as compared to spheroids grown in serum poor medium, that were less compact, see Figure 3.3.1.6.

Results

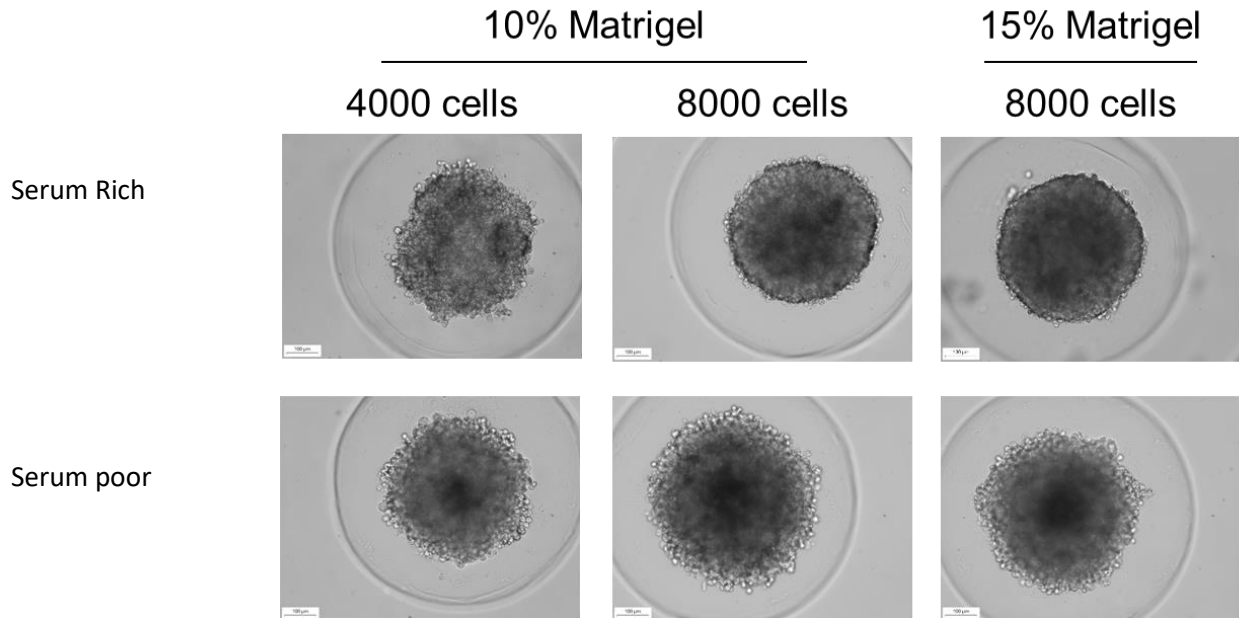


Figure 3.3.1.7 Removal of serum to induce spheroid formation reduces compactness of 1889c spheroids. Serum was highly important for 1889c (but not for Ty82) cells to form round shaped spheroids that are suitable for NMR measurements. For this reason TTS was excluded from subsequent experiments with 1889c cells.

3.4 NMR based toxicology: In vitro NMR metabolomics with the newly developed technique to study the impact of the anti-cancer drug bortezomib on 3D cell culture models of the thymic carcinoma cell lines 1889c and Ty82

3.4.1 Dose response curves for 2D and 3D cell cultures

EC values for bortezomib (evaluating concentrations in the range of 0.0001 μM -1000 μM) were obtained with the CellTiter-Glo Luminescent Cell Viability Assay as readout (described in subchapter 2.2.2.12 in the “Materials and Methods” section). This assay was chosen, because the quantification of ATP as viability test works with both 2D and 3D cells, which aids in comparison, although the following assay adaptations were necessary: in 2D cell cultures just high serum (TMTS, 10% serum) conditions were employed, while in 3D cell cultures both high serum (TMTS, 10% serum) and low serum (TTS, 0.5% serum) were applied. Moreover, for 3D culture the preparations were done in the presence of Matrigel.

EC₂₀, EC₅₀ and EC₈₀ values for bortezomib were determined from the dose response curves shown in Figures 3.4.1.1 and 3.4.1.2 and are listed in Table 3.4.1.1. The values for EC₂₀, EC₅₀ and EC₈₀ were higher for 1889c cells than for Ty82 cells, irrespective of whether 2D or 3D cultures were compared. Furthermore, the 3D models of both cell lines showed higher values for both EC₂₀, EC₅₀ and EC₈₀ than the corresponding 2D models. This indicates that both cell lines were more drug resistant if grown as 3D cultures (i.e. spheroids) than as 2D cultures (Figures 3.4.1.1, 3.4.1.2 and Table 3.4.1.1). Moreover, Ty82 3D cell culture grown with TMTS showed higher values for EC₂₀, EC₅₀ and EC₈₀ as compared to Ty82 spheroids grown with TTS, which also indicates that spheroids grown in TMTS (i.e. serum high medium) are more drug resistant than those grown in TTS. No such data are available for 1889c spheroids, which were exclusively grown in TMTS. Nevertheless, by far the highest drug resistance was found for 1889c spheroids grown in TMTS (see Table 3.4.1.1).

Results

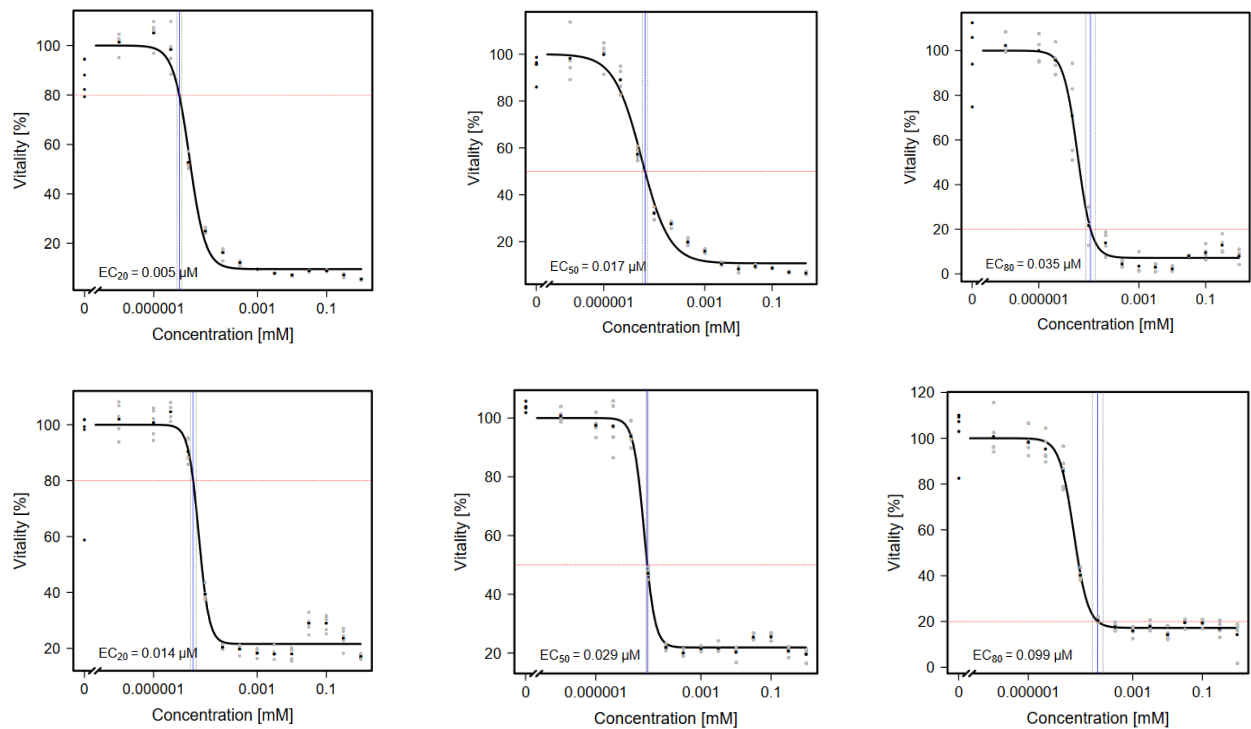


Figure 3.4.1.1 Dose response curves for bortezomib for the cell lines Ty82 (top row) and 1889c (bottom row) in 2D cell culture, both with high (10%) serum. A quantification of ATP was performed 48 hours after the application of bortezomib to measure the number of viable cells employing a CellTiter-Glo® Luminescent Cell Viability Assay. The 2D cultures were established with a seeding number of 10000 cells per well of a 96 well plate. A standard curve for ATP and untreated controls were employed as references for data normalization.

Results

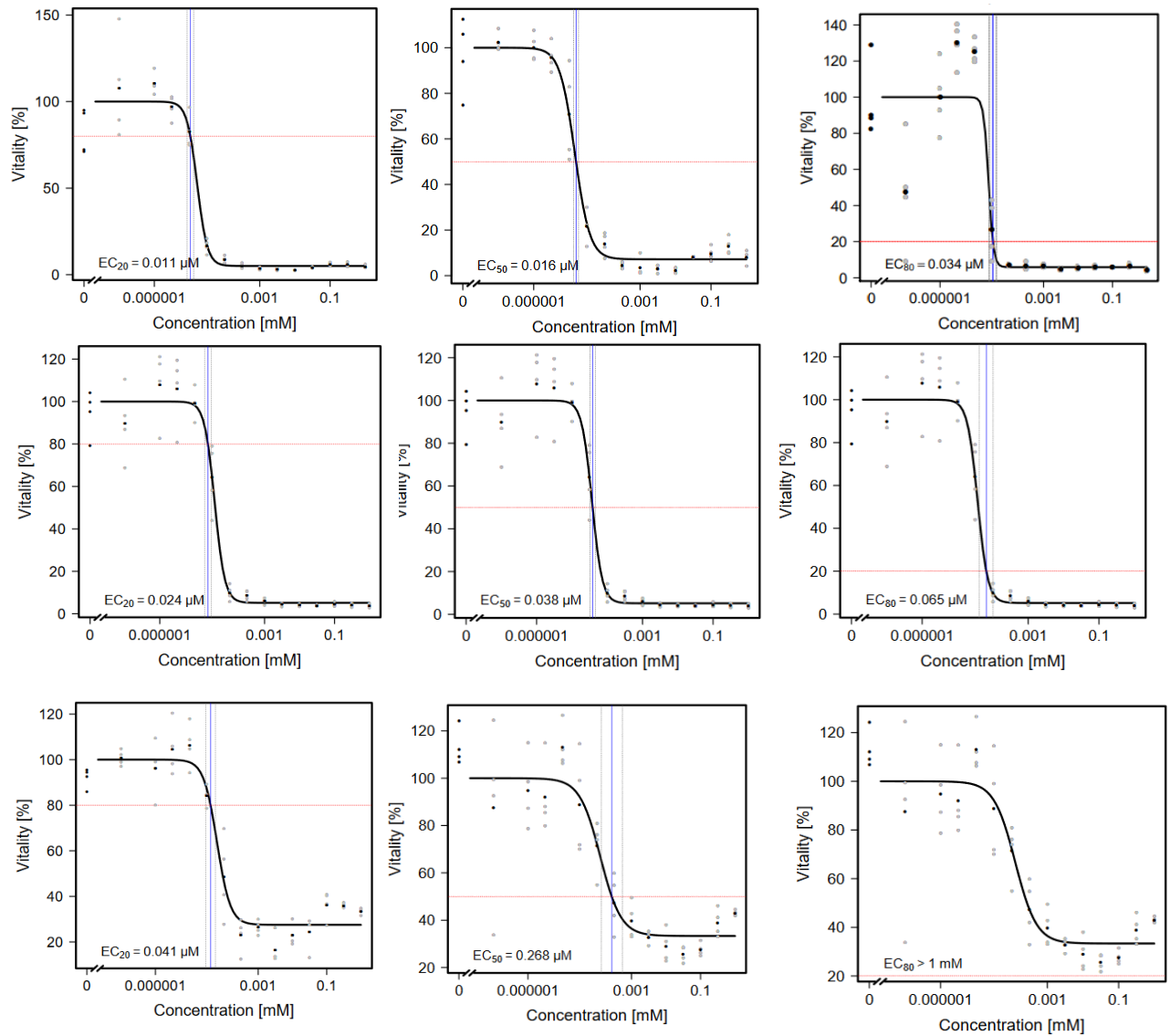


Figure 3.4.1.2 Dose response curves for bortezomib for the cell lines Ty82 with 10% serum (top row), with 0.5% serum (middle row) and 1889c with 10% serum (bottom row) in 3D cell culture. A quantification of ATP was performed to measure the number of viable cells employing a CellTiter-Glo® Luminescent Cell Viability Assay. Spheroids of Ty82 and 1889c cells were generated using the simple rotation technique combined with 3D molds and co-culturing with matrigel. A standard curve for ATP and untreated controls were employed as references for data normalization.

Results

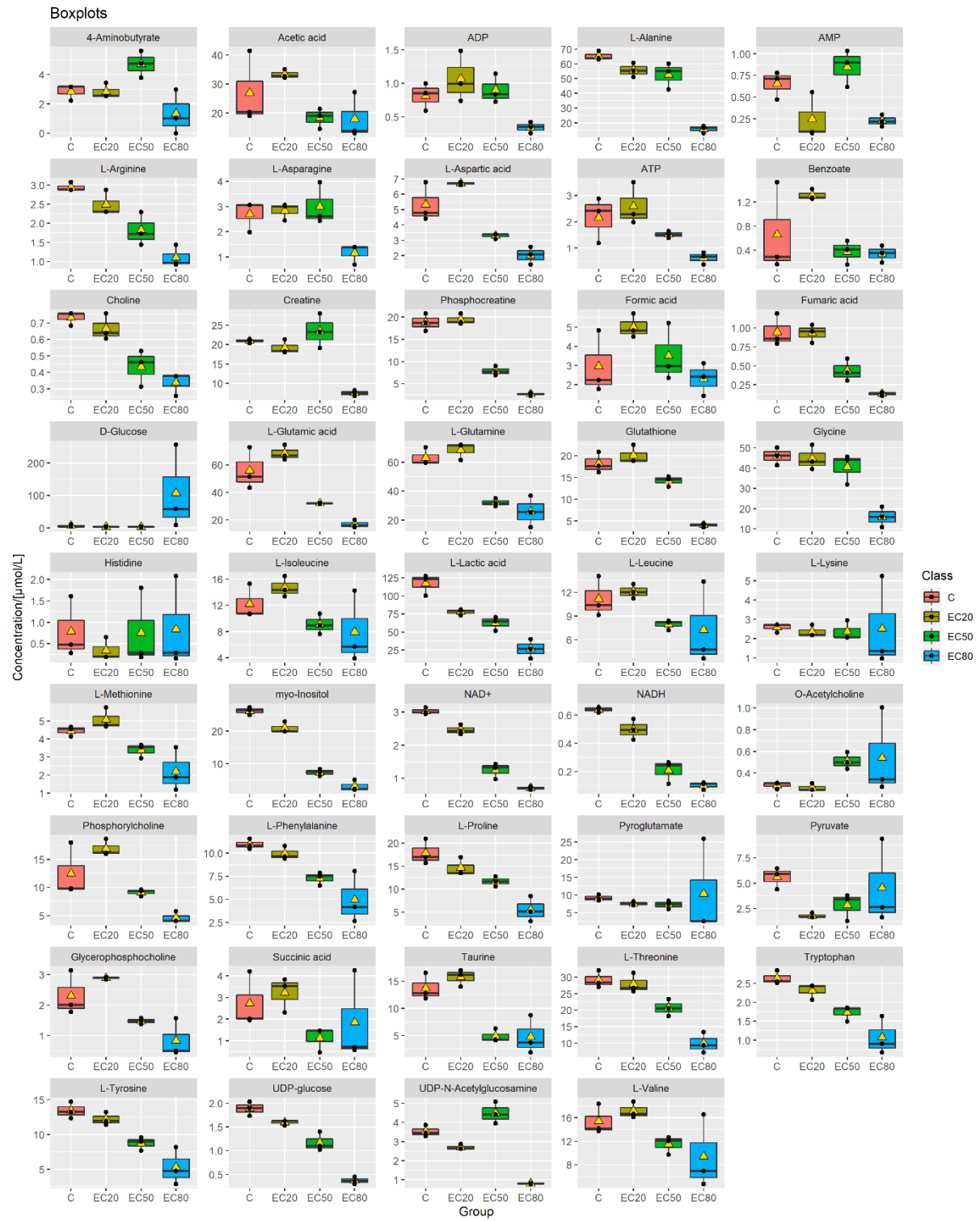
Table 3.4.1.1 EC20, EC50 and EC80 values for bortezomib for the cell lines Ty82 and 1889c, both for 2D and 3D cell culture (the latter with high (10%) serum and with minimal (0.5%) serum), as determined from the dose response curves in Figures 3.4.1.1 and 3.4.1.2. TMTS (Thymic Multicellular Tumor Spheroids Serum) consists of the same ingredients as the 2D culture medium for both cell lines. TTS (Thymic tumor spheroid) on the other hand consists of 50mL RPMI without HEPES with 5mL (v/v) penicillin and streptomycin, 100µL Epidermal Growth Factor human EGF, 500µL B-27 Supplement (50x), 10µL Recombinant Human FGFb, 25µL Insulin, 500µL Hydrocortisone and 250µL Heparin.

Cell line	EC20	EC50	EC80
Ty82 2D	6.5nM	15nM	37nM
1889c 2D	14.5nM	27nM	99nM
TY82 TMTS 3D	23nM	33nM	66nM
TY82 TTS 3D	10nM	19nM	47nM
1889c TMTS 3D	46.5nM	180nM	400nM

3.4.2 Impact of bortezomib on the metabolite profiles of Ty82 cells and 1889c cells in 2D cell culture

NMR-based profiling revealed 44 and 45 metabolites in Ty82 and 1889c cells, respectively grown in 2D cell culture, after bortezomib treatment. Bortezomib was applied at concentrations corresponding to EC20, EC50 and EC80 (given in Table 3.4.1.1) for 24 hours. Boxplots of the metabolic profiles obtained in Ty82 cells and 1889c cells are displayed in Figures 3.4.2.1 and 3.4.2.2, respectively.

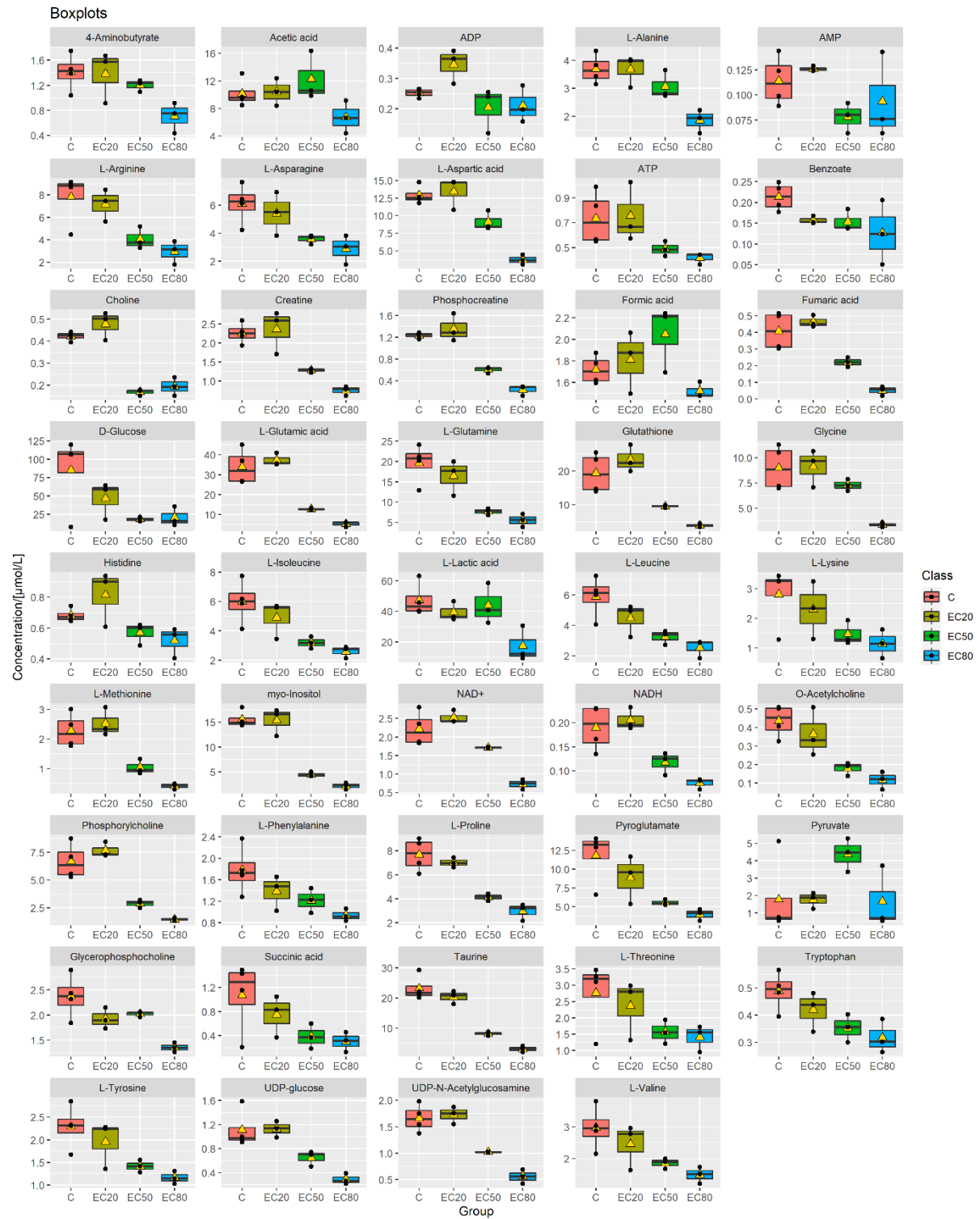
Results



Results

Figure 3.4.2.1: NMR-based profiling revealed 45 metabolites in Ty82 cells grown in 2D culture, after bortezomib treatment. Bortezomib was applied at concentrations corresponding to EC20, EC50 and EC80 (see Table 3.4.1.1 for the values) for 24 hours. For comparison, an untreated control is shown as well. On drug application, the concentrations of most metabolites, except pyruvate, decreased with respect to the control, especially for EC80. Note the decrease of lactate, glutamate and glutathione concentrations with increasing drug concentrations. Profiling experiments were done in triplicate.

Results



Results

Figure 3.4.2.2: NMR-based profiling revealed 44 metabolites in the 1889c cell line in 2D culture after bortezomib treatment. Bortezomib was applied at concentrations corresponding to EC20, EC50 and EC80 for 24 hours. For comparison, an untreated control is shown as well. On drug application, the concentrations of most metabolites, except pyruvate, decreased with respect to the control, especially for EC80. Note the decrease of lactate, glutamate and glutathione concentrations with increasing drug concentrations. Profiling experiments were done in triplicate.

As shown in Figure 3.4.2.1 (for Ty82 2D cell culture) and Figure 3.4.2.2 (for 1889c 2D cell culture) the application of bortezomib was followed by a decrease of the concentrations of most metabolites, except pyruvate. Especially the concentrations of most metabolites at bortezomib concentrations of EC80 were lower than in the control and at bortezomib concentrations of EC20 and EC50. Note especially the decrease of lactate, glutamate and glutathione concentrations with increasing concentrations of bortezomib. On the other hand, the concentrations of pyruvate remained constant in both cell lines if grown in 2D cell culture.

3.4.3 Impact of bortezomib on the metabolite profiles of Ty82 cells and 1889c cells in 3D cell culture, measuring whole spheroids

The effect of bortezomib on the metabolism of 3D models of Ty82 cells and 1889c cells was profiled over 24 hours at a drug concentration corresponding to EC80 (see Table 3.4.1.1) as a function of time (distance between time points of 3h, overall time was 24h) with a newly developed NMR technique that measures metabolites in whole spheroids. The metabolic profiles comprised 9 metabolites each in Ty82 cells and 1889c cells and are displayed in Figures 3.4.3.1 and 3.4.3.2, respectively. The display of just 9 metabolites for 3D cell cultures, in contrast to more than 40 metabolites for 2D cell cultures, is due to the much reduced signal to noise ratio of NMR data from 3D cell cultures.

In some analogy to the 2D cell culture results, where I found a decrease of glutamate and glutathione concentrations with time, I observed a decrease of glutamate and glutathione concentrations in 3D cell culture with time. In contrast to the findings in 2D cell cultures, pyruvate could not be detected at all in the 3D cell cultures, and lactate levels were increasing with time in spheroids of both Ty82 cells and 1889c cells (Figures 3.4.3.1 and 3.4.3.2, respectively), while in 2D cell cultures the lactate levels were decreasing with time.

Results

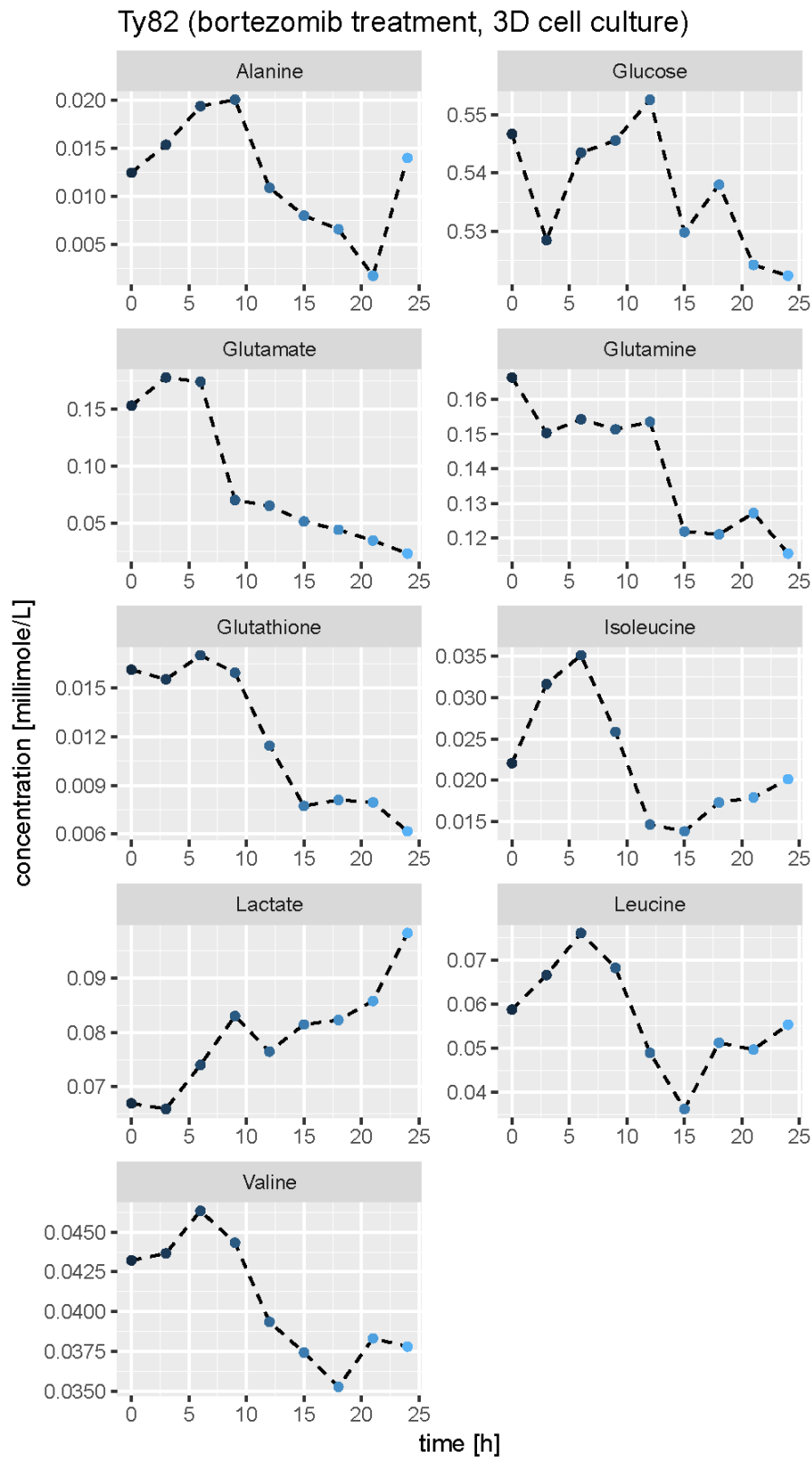


Figure 3.4.3.1: Concentrations of 9 metabolites in a Ty82 spheroid, measuring the whole spheroid as a function of time. Bortezomib was applied at the time $t=0$ at a concentration corresponding to EC80 (see Table 3.4.1.1). Note that pyruvate, in contrast to 2D cell culture, could not be detected at all. Lactate levels are increasing with time, also in contrast to 2D cell

Results

culture. Generally the concentrations of all metabolites except lactate are decaying with time, see especially the values for glutamate and glutathione.

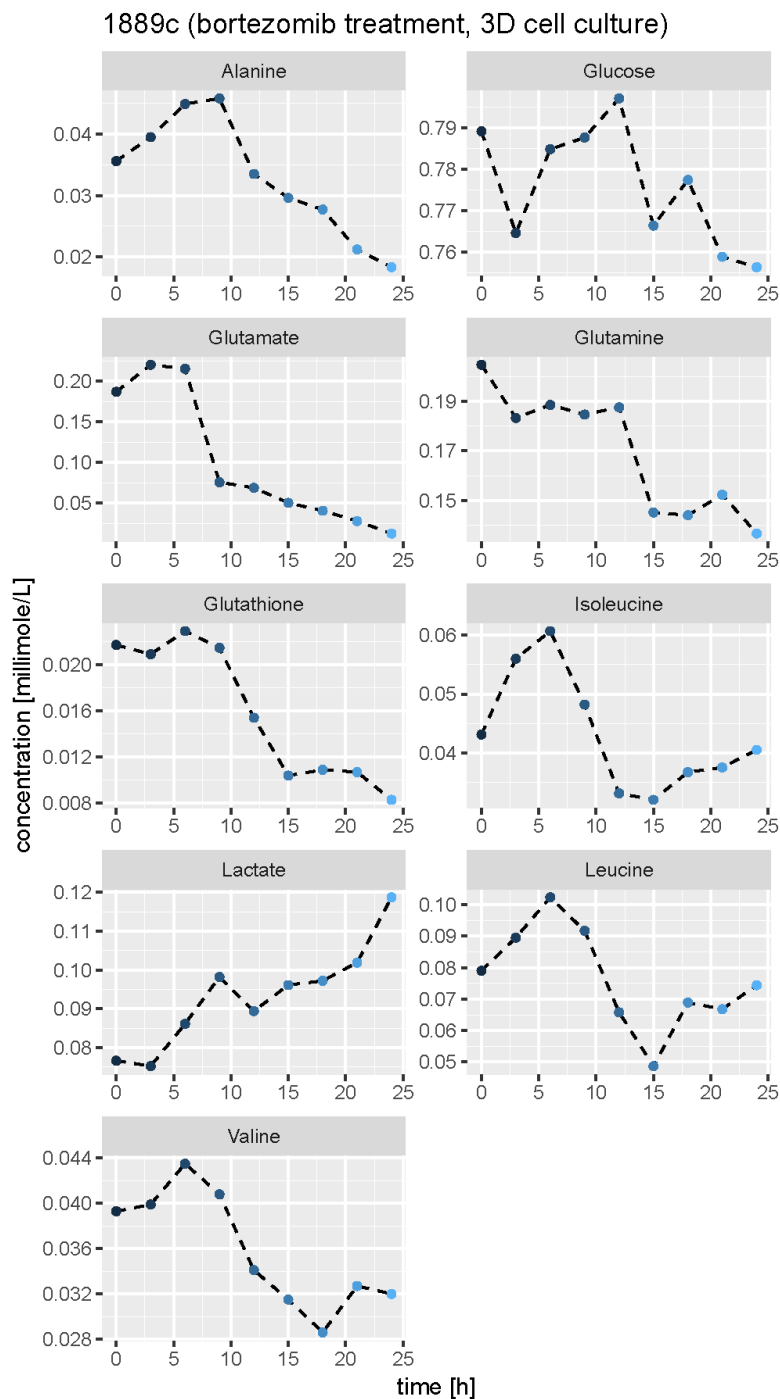


Figure 3.4.3.2: Concentrations of 9 metabolites in a 1889c spheroid, measuring the whole spheroid as a function of time. Bortezomib was applied at the time $t=0$ at a concentration corresponding to EC80 (see Table 3.4.1.1). Note that pyruvate, in contrast to 2D cell culture, could not be detected at all. Lactate levels are increasing with time, also in contrast to 2D cell

culture. Generally the concentrations of all metabolites except lactate are decaying with time, see especially the values for glutamate and glutathione.

4 Discussion

The major new findings of this thesis are the following:

- 1) HRMAS ¹H-NMR and cluster analysis detected 37 metabolites and differentially enriched metabolic pathways, respectively, in indolent compared to aggressive TETs.
- 2) Using a new NMR and long-term perfusion technique, space-resolved metabolomics studies of individual 3D TC cell line spheroids over extended time periods were achieved.
- 3) TC cell line-adapted techniques to generate spheroids suitable for NMR metabolomics were developed.
- 4) Metabolic responses and drug susceptibilities of TC cell lines to the proteasome inhibitor, Bortezomib, were found to be different in 2D as compared to 3D cell culture models.

4.1 TET tissue metabolomics studies

4.1.1 General versus TET-specific metabolites

The number of 37 metabolites detected in TETs in this NMR study compares well with metabolite numbers (n=9-34) found in previous studies of non-thymic cancers (Choi et al., 2012; Park et al., 2016) as well as with the 42 metabolites detected with NMR in breast cancers (Gogiashvili et al., 2018b). Although breast cancers are adenocarcinomas with very different genetic aberrations, the overlap of detected metabolites between thymic cancer on the one hand and breast and lung cancers on the other hand was noticeable (Figure 4.1.1). Most detected metabolites obviously reflect general tumor-biological processes rather than organ- or tumor-specific features. Thus, the higher levels of lactic acid shared by aggressive thymomas and TCs likely reflect the switch in energy metabolism known as the Warburg effect, which is observed in many cancer types (Lemasters, 2021). Similarly, high levels of glutathione, one of the key regulators of the cellular redox state, are also typical of other aggressive cancers and associated

Discussion

with resistance to chemotherapy (Kennedy et al., 2020). Conversely, aggressive TETs showed low levels of cysteine and myo-inositol i.e. a feature of non-thymic aggressive cancer types with alterations of the redox state and oncogenic PI3K/AKT signaling (Bizzarri et al., 2016; Choi et al., 2012; Daher et al., 2020).

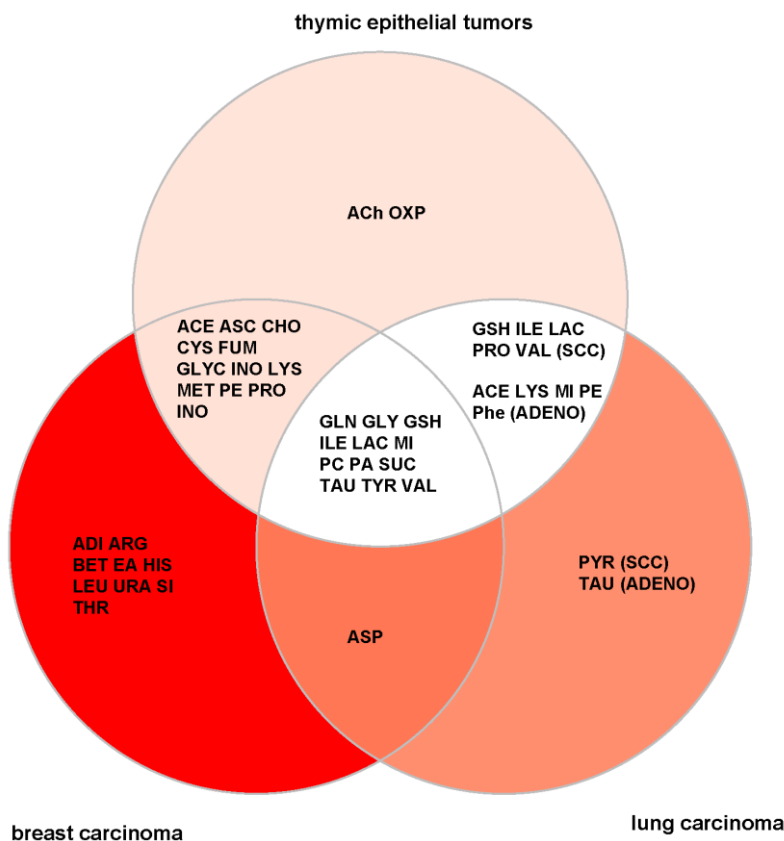


Figure 4.1.1.1 Venn diagram of the metabolite distribution in breast cancer (Choi et al., 2012), thymic epithelial tumors (TETs) (this study) and lung cancer (Bamji-Stocke et al., 2018). Note that most detected metabolites in TETs were previously detected in lung and breast cancers as well. Only acetylcholine and oxypurinol are 'unique' metabolites of TETs. For squamous cell (SCC) lung carcinoma and adenocarcinoma (adeno) of the lung the 'unique' metabolites were

pyruvate and taurine, respectively (Part of these results were recently submitted for publication in *CANCERS*.).

In contrast to the mostly unspecific metabolites detected in TETs, acetylcholine and oxypurinol were undetectable in breast and lung cancers (Figure 4.1.1.1). This is intriguing since acetylcholine receptor subunits are expressed by the tumor cells of thymomas, particularly if associated with Myasthenia Gravis (MG) (Marx, Yamada et al., 2021; Radovich et al., 2018). Accordingly, sufficiently powered, future metabolite profiling studies of myasthenic versus non-myasthenic TETs might provide new insights into the enigmatic pathogenesis of thymoma-associated MG. The occurrence of oxypurinol in B2 and B3 thymomas (Figure 3.1.1.2) is even more enigmatic: While careful anamnesis excluded allopurinol medication as source of oxypurinol (Wilson & Berns, 2012), high natural levels of intratumorous oxypurinol have not yet been reported, and the link to the observed enrichment of the KEGG purine pathway in aggressive TETs (Figure 4.1.1.1) is currently unclear.

However, since purine metabolites are constituents of tumor derived exosomes (Ludwig et al., 2020) and oxypurinol was recently detected in the blood of non-thymic cancer patients (Dumanskiy et al., 2020), it appears warranted to evaluate oxypurinol in TETs and in the blood of patients with a mediastinal mass as prognostic and non-invasive diagnostic marker, respectively (Part of these results were recently submitted for publication in *CANCERS*.).

4.1.2 Metabolite profiles meet KEGG pathway activation and gene expression

Although the number of up to 37 metabolites detected in TETs might appear low, it clearly distinguished the three tumor-biologically different and clinically relevant TET groups by unsupervised cluster analysis: i) the indolent type A, AB and B1 thymomas that can mostly be cured by surgery; ii) type B2 and B3 thymomas that often require (neo-) adjuvant treatments and have a less favorable prognosis; and iii) the often lethal TCs that are mostly unassociated with autoimmunity (Travis et al., 2015).

Furthermore, based on the 37 metabolites, the MetPA algorithm was able to predict shared and differentially activated metabolic pathways in the clinically most relevant groups of aggressive TETs, i.e. B2 and B3 thymomas versus TCs. The relevance of these pathways, in turn, could be

confirmed through gene set enrichment analysis (GSEA) of the independent TCGA TET dataset (Radovich et al., 2018). By GSEA, the glycolysis/gluconeogenesis pathway (together with the citrate/TCA cycle) was the most strongly enriched pathway in aggressive TETs (Figure 4.1.1.1). This is in line with metabolic alterations previously reported as characteristic of the Warburg effect - high levels of lactic acid, and the preferential expression of the glucose transporter, GLUT1 in TCs and B3 thymomas. While these features are the reason for the success of 18F-fluorodeoxy-glucose-based positron emission tomography to predict aggressive TETs, they are not specific for them (Kaira et al., 2012). Likewise, the enrichment of the TCA cycle pathway and the Alanine/aspartate/glutamate metabolic pathway in aggressive TETs (Figure 4.1.1.1) is a feature of many aggressive cancers (N. Anderson et al., 2018). (Part of these results were recently submitted for publication in *CANCERS*.).

4.1.3 Therapeutic perspectives

Proline was the most strongly and differentially expressed metabolite in aggressive TETs compared to normal thymi (Figure 3.1.2.1), and I observed differential transcription of the *PYCR1* gene, which encodes pyrroline-5-carboxylate reductase 1 in the TCGA dataset (Table 3.1.5.1). *PYCR1* catalyzes the last step of proline biogenesis (D'Aniello et al., 2020). With proline having a major impact on energy metabolism, the redox state, apoptosis and proliferation of tumor cells, *PYCR1* has been suggested as a promising therapeutic target in many cancers (D'Aniello et al., 2020; Liu et al., 2017; Phang, 2019). It seems reasonable to assume that aggressive TETs may also respond to *PYCR1* inhibition. Since *PYCR1*-targeting agents that block proline synthesis are under development (Christensen et al., 2020), it will become possible to test the responsiveness of TETs to *PYCR1* inhibition.

Low levels of cysteine (a glutathione precursor), in conjunction with high levels of glutathione (Figure 3.1.1.2) are another new finding in TETs. In many cancers, this profile indicates an altered redox landscape that promotes tumor progression and treatment resistance (Narayanan et al., 2020). Tightly regulated levels of reactive oxygen species (ROS) and anti-oxidants like glutathione are important to maintain redox homeostasis and tumor cell survival (Kennedy et al., 2020). Therefore, drugs that tip the redox balance towards excess oxidative stress (van Loenhout et al., 2020) or towards reduced glutathione synthesis either directly or through cysteine starvation (Kennedy et al., 2020) appear worth testing in future studies of refractory TETs. Such drugs are currently being developed (Zhang et al., 2021).

Discussion

High lactate levels (Figure 3.1.1.2), enrichment of the glycolysis pathway (Figure 4.1.1.1), including overexpression of hexokinases (*HK1*, *HK3*) and pyruvate kinase (*PKM*) (Table 3.1.5.1), as well as the strong protein expression of the glucose transporter, GLUT1 (Thomas de Montpréville et al., 2015) all hint to altered metabolism indicative of the so-called ‘Warburg effect’ as a source of vulnerability in aggressive TETs (Akins et al., 2018). Small molecule inhibitors to GLUT1, hexokinases and PKM2 are already available for preclinical testing (Sukjoi et al., 2021).

Finally, a prominent ‘Warburg effect’ implies the critical need of cancer cells to fuel the TCA cycle with glutamate through glutaminolysis for the synthesis of vital cellular constituents, including nucleotides and glutathione (Akins et al., 2018). High levels of glutamine (Figure 3.1.1.2) and an activated glutamine/glutamate pathway (Table 3.1.4.1) suggest that this pathway is functional in aggressive TETs. Therefore, inhibitors of glutaminolysis and downstream pathways of the TCA cycle appear to be rational therapeutic strategies. In fact, the TCA cycle inhibitor, AG-881 that targets IDH1 (isocitrate dehydrogenase 1) and is currently being tested in phase I clinical trials with leukemia and glioma patients (NCT02492737 and NCT02481154) appears as promising agent, since I found IDH1 to be highly expressed in aggressive TETs (Table 3.1.5.1) (Part of these results were recently submitted for publication in *CANCERS*).

4.1.4 Conclusion

Platinum-based chemotherapies and immune checkpoint inhibitors are the established mainstay and promising drug candidates, respectively, for first- and second/third-line treatments of non-resectable, aggressive TETs (Conforti et al., 2020). However, it is known from other types of cancers (Guo et al., 2019; Sharma et al., 2020) that these very therapies are compromised by some of the metabolic features described here for the first time in TETs. Therefore, it appears as promising future personalized strategy for patients with advanced or refractory TETs to augment the limited efficacy of well-established chemotherapies and modern biological interventions. Through the additional targeting of tumor-specific metabolic vulnerabilities in such scenarios, the determination of metabolic profiles of TETs as biomarkers appears warranted (Part of these results were recently submitted for publication in *CANCERS*).

4.2 A new NMR technique for online metabolomics studies of 3D cell culture

4.2.1 Comparison of the technique to other approaches

The currently available methods to investigate metabolic processes in small 3D models (e.g. tumor cell spheroids) have the disadvantage to provide a “snap-shot” of the metabolic state at a selected time point and to be destructive. Accordingly, a measurement at another time point so far does require the selection of another spheroid. Alternatively cell extracts from 3D cell cultures can be investigated, which is the topic of several Mass Spectrometry (MS) or NMR based metabolic studies (Coloff et al., 2016; Fan et al., 2018; Rusz et al., 2019; Vorrink et al., 2017). Unfortunately, the chemical extraction can effect metabolic concentrations and any spatial information is lost, which would be a valuable information to characterize the distribution of nutrition and waste products as well as the response to drugs and toxins in 3D culture. It has been shown that spatial resolved metabolomics can be performed using Matrix-Assisted Laser Desorption/Ionization (MALDI) MS, although fixing of the spheroid in a matrix potentially alters metabolite concentrations and impedes dynamic investigations of single spheroids (Ahlf Wheatcraft et al., 2014; Palubeckaitė et al., 2020). On the contrary, NMR spectroscopy as a non-destructive technique can yield spatially resolved spectra of living spheroids. Indeed ^1H , ^{13}C , ^{19}F and ^{31}P NMR spectra have been acquired for cells and multiple spheroids dispersed in gel matrices or suspended by mechanical force, keeping the cells viable via perfusion with medium (Cerofolini et al., 2019; Freyer et al., 1990). Due to the comparably low sensitivity of NMR spectroscopy, all of these studies have been performed without spatial resolution using large cell and spheroid numbers. However, a few studies already demonstrated that ^1H NMR spectra can indeed be obtained for single spheroids and that spatial resolved NMR sequences enable to differentiate between the core and the shell domain (Minard et al., 1998; Palma et al., 2016). In these studies the spheroids were fixed in an agarose gel and were not supplied with any medium, again preventing dynamic measurements. Instead, the approach used in this thesis allows to obtain spatial and temporal resolved metabolic data on single spheroids measured over several days under physiological conditions. In this thesis, I describe the development of an easy to replicate microfluidic measurement insert fixing the spheroid’s position, while maintaining nutrition supply and waste product removal. Furthermore, I use slice-selective pulse sequences that can be employed with any commercially available cryogenic NMR equipment, which ensures the highest detection sensitivity possible with NMR (Reprinted with permission from *Anal. Chem.* 2021, 93, 40, 13485–13494, doi: 10.1021/acs.analchem.1c02221, Publication Date: September 3, 2021, Copyright 2021 American Chemical Society.).

4.2.2 Conclusion

In this thesis I introduced a new NMR approach providing time and spatial resolved metabolic insights in 3D cell models in non invasive measurements. First results applying this technique to living Ty82 spheroids are in agreement with literature data and staining experiments on spheroids of similar size. Finally, long term data for a spheroid provided evidence that this technique can be employed to observe dynamic processes in metabolism for up to 92 hours. These findings reveal that the presented method might become a valuable tool to study the metabolic impact e.g. of anticancer drugs on tumor cells grown in 3D models.

4.3 New technique to prepare spheroids suitable for NMR

4.3.1 The rotation technique to produce spheroids

In a cell culture suspension, cells tend to aggregate and to go through the process of self-assembly. When a constant circular rotation is acting on the cells in a rotating wall vessel, the cells are kept in a suspended state in the vessel (Melnik et al., 2020). In the standard rotating wall vessel technique the cell suspension is centrifuged for five minutes and then left to grow (Melnik et al., 2020). The main drawback of this technique is the broad size range of spheroids being generated (Badea et al., 2019).

In my new technique the cells rotate continuously at a speed of 100rpm and are co-cultured with the biological scaffold Matrigel™. This scaffold is commonly used for spheroid formation, as it provides physical support for cells to attach and reorganize into 3D structures and it contributes soluble growth factors as well as hormones, which can affect gene and protein expression (Langhans, 2018). Moreover, some key components for cell growth and attachment such as collagen and laminin are found in Matrigel (Langhans, 2018). The process of co-culturing is performed in a microtissue mold. For co-culturing with matrigel the cells are transferred to a microtissue mold, followed by another period of rotation at 100 rpm. This avoids batch to batch variations and ensures a better roundness of the spheroids obtained.

This approach led to the formation of well-defined 3D models, with a uniform morphology, increased diameter and good circularity. This is in accordance with a study (Dubiak-Szepietowska et al., 2016) comparing HepG2 MCS culture in collagen, gelatin and Matrigel hydrogels, which revealed that cells proliferated rapidly in Matrigel, and larger spheroids were

harvested from Matrigel. Especially the latter property is essential for NMR studies as described in 4.2. Another study (Badea et al., 2019) shows that the addition of Matrigel improves the growth environment of tumor spheroids, bringing it closer to that of in vivo tumor conditions. Serum as a source of growth factors (Heger et al., 2018) for cells growing in cell culture had to be added to the 1889c cell line 3D culture, while the Ty82 cell line could be cultured both with and without serum, which remains enigmatic and is possibly due to different levels of proliferation of the two cell lines.

4.3.2 Conclusion

The new NMR technique for the long term measurement of metabolites in individual spheroids does not require a high yield of spheroids but is best supported by large spheroids with minimal size variation and maximal roundness. This aim was best accomplished with the “100 pm-rotation technique” for 3D cell cultures that could be combined with the intermediate co-culturing with Matrigel in a microtissue mold. Thus, the combination of the new NMR technique with the new method to generate a homogeneous population of “next to perfect” spheroids will set the stage for the optimal long-term monitoring of metabolite profiles in cancers cells grown as spheroids.

4.4 NMR toxicology: Bortezomib impact on 2D and 3D culture of thymic cell lines

4.4.1 Bortezomib as a drug against thymic malignancies?

Metabolic features identified in TET tissue analysis (see 4.1) with NMR are known to coincide with the failure of typical therapies employed for non-resectable TETs like resistance to cisplatin-based drugs, kinase inhibitors and immune checkpoint blockers. Lacking therapeutic options for non-resectable TETs have fostered the search for new therapeutic options, including the use of proteasome inhibition. For an unresectable stage III thymic cancer it has been reported (Dooley & Anderson, 2016) that a combination of intensity modulated radiation therapy and Bortezomib treatment, continued also post-radiation, appears to be a useful

definitive treatment option for unresectable thymic carcinomas. The patient made a full recovery and remained disease free 4 years after the treatment. It is, however, uncertain whether Bortezomib was decisive in the patient's treatment outcome (Dooley & Anderson, 2016).

Bortezomib as the first approved (D. Chen et al., 2011) proteasome inhibitor has become the gold standard in the treatment of multiple myeloma (K. Anderson, 2012; Moreau et al., 2012) and other hematologic malignancies (Niewerth et al., 2015). The efficacy as well as metabolic consequences of Bortezomib applied to thymic malignancies, however, have remained enigmatic so far.

4.4.2 Bortezomib impact detected with NMR metabolic profiling

The NMR based metabolic profiling investigations in this study revealed substantial differences between thymic cancer 2D and 3D cell culture. Specifically the studies showed that 3D cell cultures were largely resistant to Bortezomib. It is obvious from the higher levels of glutathione detected in 3D as compared to 2D cell cultures that there is an increased antioxidant capacity in the former. In line with this, it was found (Z.-X. Du et al., 2009) that high intracellular glutathione levels protect cells from Bortezomib-induced apoptosis. Moreover, pathways involved in the response to reactive oxygen species were shown to be connected to Bortezomib resistance (Fujiwara et al., 2013; Maiso et al., 2015; Sanchez et al., 2013; I.-S. Song et al., 2013; Soriano et al., 2016; Thompson et al., 2017). A decrease of glutamate and glutathione levels with increasing dose of Bortezomib was observed, being attributed to the inhibition of glutaminase (GLS) (N. Anderson et al., 2018) and glutamate-cysteine ligase (GCLC), respectively. GCLC converts glutamate to glutathione, and is known to be highly expressed in several cancers (Beatty et al., 2018; Lien et al., 2016). Moreover, decreasing glutamate levels correspond to decreasing aspartate and proline levels in both Ty82 and 1889c cell lines (Figures 3.4.2.1 and 3.4.2.2, resp.), limiting the proliferation of cancer cells (Lien et al., 2016; Loayza-Puch et al., 2016).

Differences in the metabolic response to Bortezomib between 2D and 3D cell culture can be traced back to LDHA, which is assumed to be expressed in 3D while inhibited in 2D thymic cell culture. LDHA is known to be associated with carcinogenesis (Feng et al., 2018). 3D cell culture models of thymic cancer show a resistance to Bortezomib toxicity which is not found in the corresponding 2D models. From hematologic malignancies it is known, that cancer cells

Discussion

resistant to Bortezomib show an increased mitochondrial activity employing glutamine as an energy source (Thompson et al., 2017). This is in accordance with the inhibition of GLS, which blocks the metabolism of glutamine to glutamate (GLS independent glutamine utilization) (Thompson et al., 2017), that was assumed in this investigation.

However, Bortezomib was found ineffective against solid tumors both in animal experiments and in clinical trials (Harris et al., 2020). Studies of the sensitivity of Bortezomib to osteosarcoma cells both in vitro and in vivo were performed (Patatsos et al., 2018). Though preclinical data were promising, a phase 1 clinical trial investigating the efficacy of Bortezomib in pediatric patients with solid tumors and a phase II clinical trial investigating the efficacy of Bortezomib for treatment of metastatic sarcomas found minimal activity of Bortezomib in these contexts, when applied as a single agent. Additional studies have shown that Bortezomib has poor anti-cancer activity against a range of solid tumors in vivo (C. Li et al., 2016). Explanations of the poor responses of proteasome inhibitors to solid tumors were given (Roeten et al., 2018). TP53 mutations were found to decrease the sensitivity of Bortezomib. These mutations frequently occur in solid cancers, but are uncommon in multiple myeloma and other hematologic malignancies (Flynt et al., 2020). Also KRAS mutations, occur in many pancreatic cancers (Buscail et al., 2020), were also found to be responsible for resistance to proteasome inhibition (Chiu et al., 2015).

4.4.3 Conclusions

I conclude that reports about the sensitivity of 2D cancer models towards Bortezomib must be viewed with caution. Furthermore, in view of the near lack of available TET cell lines, the establishment of *representative* tumor models for thymic malignancies must be a priority, since the NUT carcinoma cell line, Ty82 that was studied here is representative of only a rare thymic carcinoma type (Travis et al., 2015) and 1889c cells have lost some in vivo features of typical thymic squamous cell carcinomas (Yamada et al., 2021). Nevertheless, these results do not exclude that Ty82 cells and 1889c cells grown in 3D cell culture may help to elucidate resistance mechanisms in TETs, And the toxic effect of Bortezomib was much higher in 2D compared to 3D models.

4.5 Limitations of the study

Ad 4.1) The major limitations of the present study are the small sample size, the heterogeneity of histotypes and the lack of an independent validation set of TETs for repetition of the HRMAS ¹H-NMR analysis. These shortcomings are related to the rarity of TETs (Travis et al., 2015), and the even rarer chance of obtaining native resection specimens immediately after surgery in order to retrieve true ex-vivo snap-frozen tumor material which is critical for HRMAS ¹H-NMR. In future studies, this problem can be overcome by core needle biopsies that retrieve tumor material of “near-to-in-vivo” quality. Still, through the combined use of metabolite profiling for functional pathway prediction in a small cohort of tumors and the analysis of transcriptomic profiles of the same and related pathways in a large, independent cohort of TETs, I achieved new insights into their metabolic features and spotted therapeutic candidate targets.

Ad 4.2) Under conditions of high spatial resolution, i.e. with a slice thickness of 100 μm, the detection of the metabolite signal might take as long as 4 hours, if a good signal to noise ratio is to be obtained. Dynamic changes in metabolism might, however, appear much faster than observable on this timescale. In such a case sacrificing the spatial resolution and measuring the full spheroid instead of individual slices allows for a faster measurement and typically for a time resolution of 30 minutes.

Ad 4.3) Why serum as a source of growth factors had to be added to the 1889c cell line 3D culture, while the Ty82 cell line could be cultured both with and without serum, remains enigmatic. Moreover the spheroids produced lack many important parameters influencing the tumor microenvironment. The development of more complex 3D cell co-culture models would help to mimic additional physiological parameters like angiogenesis, for example by adding endothelial cells.

Ad 4.4) The expression levels of GLS, GCLC and LDHA have not yet been measured, neither in 2D nor in 3D cell cultures treated with Bortezomib. So far, just a metabolomic readout exists.

In spite of these limitations, the current thesis advanced our knowledge of metabolic features of thymic epithelial tumors. In particular, the NMR based investigations of ex vivo derived, snap frozen thymoma and thymic carcinoma tissues gave strong hints to potential vulnerabilities for future drug development and either preclinical drug testing (if representative tumor models will become available) or the design of clinical trials. The latter may take metabolite profiles as new biomarkers into account.

5 Summary

Thymomas and thymic carcinomas (TC) are malignant thymic epithelial tumors (TETs) that mostly lack targetable mutations. Metabolic signatures of TETs have not yet been studied and may offer new therapeutic options. Metabolic profiles in snap-frozen thymomas (n=12) and TCs (n=3) were determined by high resolution magic angle spinning ^1H nuclear magnetic resonance (HRMAS- ^1H NMR) spectroscopy. Metabolite-based prediction of active KEGG metabolic pathways was achieved with MetPA. In relation to metabolite-based metabolic pathways, gene expression signatures of TETs (n=115) in “The Cancer Genome Atlas” (TCGA) dataset were investigated using gene set enrichment analysis tools. Overall, thirty-seven metabolites were quantified in TETs, including acetylcholine that was not previously detected in other non-endocrine cancers. Metabolite-based cluster analysis distinguished indolent (WHO types A, AB, B1) and aggressive (B2, B3) thymomas and TCs. Six KEGG metabolic pathways were predicted as activated, including proline/arginine, glycolysis and glutathione pathways, and these pathways were generally enriched transcriptionally in the independent TCGA dataset. Shared high lactic acid and glutamine levels and associated gene expression signatures hint to a strong “Warburg effect”, glutaminolysis and redox homeostasis as potential vulnerabilities in aggressive TETs.

Since a recent study observed a vulnerability of neoplastic thymic epithelial cells grown in 2-dimensional (2D) cultures towards Bortezomib, the impact of this proteasome inhibitor on the metabolic profiles of Ty82 and 1889c TC cell lines was analyzed by NMR, revealing a decrease of glutamate and glutathione levels. This suggests an inhibition of glutaminase (GLS) and glutamate-cysteine ligase (GCLC) and hints to a role of oxidative stress as mechanism of action of Bortezomib, as low glutathione levels foster Bortezomib-induced apoptosis. In both TC cell lines, pyruvate levels increased with Bortezomib doses, while lactate concentrations decreased, suggesting inhibition of lactate dehydrogenase A (LDHA). Employing a new spatially selective NMR pulse technique that was developed in the framework of this thesis for *in vitro* metabolic profiling of 3D cell cultures (spheroids) under viable conditions, the impact of Bortezomib on metabolite profiles could be measured repeatedly in the same spheroids during 24h, revealing a decrease of glutamate and glutathione levels as in 2D cultures. However, in contrast to the 2D cell culture findings, pyruvate could not be detected at all in 3D cultures/spheroids, while lactate levels were increasing with time, suggesting a high expression of functional LDHA in spheroids. Finally, spheroids of TC cell lines showed relative resistance to Bortezomib when compared with the respective cell lines grown in 2D cultures. In conclusion, these results

underline the need to establish in vitro models that reflect the in vivo tumor setting as closely as possible and cast some light on the impact of Bortezomib on the metabolism of TC cell lines depending on the 2D versus 3D cell culture conditions.

6 References

- Adams, J. (2002). Preclinical and clinical evaluation of proteasome inhibitor PS-341 for the treatment of cancer. *Current Opinion in Chemical Biology*, 6(4), 493–500. doi: 10.1016/s1367-5931(02)00343-5
- Akins, N. S., Nielson, T. C., Le, H. V. (2018). Inhibition of Glycolysis and Glutaminolysis: An Emerging Drug Discovery Approach to Combat Cancer. *Current Topics in Medicinal Chemistry*, 18(6), 494–504. doi: 10.2174/1568026618666180523111351
- Akoka, S., Barantin, L., Trierweiler, M. (1999). Concentration Measurement by Proton NMR Using the ERETIC Method. *Analytical Chemistry*, 71(13), 2554–2557. doi: 10.1021/ac981422i
- AlWahsh, M., Othman, A., Hamadneh, L., Telfah, A., Lambert, J., Hikmat, S. et al. (2019). *Second exposure to acetaminophen overdose is associated with liver fibrosis in mice.*
- Anderson, K. (2012). The 39th David A. Karnofsky Lecture: bench-to bedside translation of targeted therapies in multiple myeloma. *Journal of Clinical Oncology : Official Journal of the American Society of Clinical Oncology*, 30(4), 445–452. doi: 10.1200/JCO.2011.37.8919
- Anderson, N., Mucka, P., Kern, J., Feng, H. (2018). The emerging role and targetability of the TCA cycle in cancer metabolism. *Protein & Cell*, 9(2), 216–237. doi: 10.1007/s13238-017-0451-1
- Badea, M. A., Balas, M., Hermenean, A., Ciceu, A., Herman, H., Ionita, D., Dinischiotu, A. (2019). Influence of Matrigel on Single- and Multiple-Spheroid Cultures in Breast Cancer Research. *SLAS Discovery : Advancing Life Sciences R & D*, 24(5), 563–578. doi: 10.1177/2472555219834698
- Bamji-Stocke, S., van Berkel, V., Miller, D., Frieboes, H. B. (2018). A review of metabolism-associated biomarkers in lung cancer diagnosis and treatment. *Metabolomics : Official Journal of the Metabolomic Society*, 14(6), 81. doi: 10.1007/s11306-018-1376-2
- Beatty, A., Fink, L., Singh, T., Strigun, A., Peter, E., Ferrer, C. M. et al. (2018). Metabolite Profiling Reveals the Glutathione Biosynthetic Pathway as a Therapeutic Target in Triple-Negative Breast Cancer. *Molecular Cancer Therapeutics*, 17(1), 264–275. doi: 10.1158/1535-7163.MCT-17-0407

References

- Beckonert, O., Keun, Hector C., Ebbels, T. M. D., Bundy, J., Holmes, E., Lindon, J. C., Nicholson, J. (2007). Metabolic profiling, metabolomic and metabonomic procedures for NMR spectroscopy of urine, plasma, serum and tissue extracts. *Nature Protocols*, 2(11), 2692–2703. doi: 10.1038/nprot.2007.376
- Bingol, K. (2018). Recent Advances in Targeted and Untargeted Metabolomics by NMR and MS/NMR Methods. *High Throughput*, 7(2), 9. doi: 10.3390/ht7020009
- Bingol, K., Brüscheiler, R. (2014). Multidimensional approaches to NMR-based metabolomics. *Analytical Chemistry*, 86(1), 47–57. doi: 10.1021/ac403520j
- Bizzarri, M., Dinicola, S., Bevilacqua, A., Cucina, A. (2016). Broad Spectrum Anticancer Activity of Myo-Inositol and Inositol Hexakisphosphate. *International Journal of Endocrinology*, 2016, 5616807. doi: 10.1155/2016/5616807
- Bliziotis, N. G., Engelke, U. F. H., Aspers, R. L. E. G., Engel, J., Deinum, J., Timmers, H. J. L. M. et al. (2020). A comparison of high-throughput plasma NMR protocols for comparative untargeted metabolomics. *Metabolomics : Official Journal of the Metabolomic Society*, 16(5), 64. doi: 10.1007/s11306-020-01686-y
- Bruzzone, C., Loizaga-Iriarte, A., Sánchez-Mosquera, P., Gil-Redondo, R., Astobiza, I., Diercks, T. et al. (2020). 1h NMR-Based Urine Metabolomics Reveals Signs of Enhanced Carbon and Nitrogen Recycling in Prostate Cancer. *Journal of Proteome Research*, 19(6), 2419–2428. doi: 10.1021/acs.jproteome.0c00091
- Buscail, L., Bournet, B., Cordelier, P. (2020). Role of oncogenic KRAS in the diagnosis, prognosis and treatment of pancreatic cancer. *Nature Reviews. Gastroenterology & Hepatology*, 17(3), 153–168. doi: 10.1038/s41575-019-0245-4
- Cerofolini, L., Giuntini, S., Barbieri, L., Pennestri, M., Codina, A., Fragai, M. et al. (2019). Real-Time Insights into Biological Events: In-Cell Processes and Protein-Ligand Interactions. *Biophysical Journal*, 116(2), 239–247. doi: 10.1016/j.bpj.2018.11.3132
- Chen, D., Frezza, M., Schmitt, S., Kanwar, J., Dou, Q. P. (2011). Bortezomib as the first proteasome inhibitor anticancer drug: current status and future perspectives. *Current Cancer Drug Targets*, 11(3), 239–253. doi: 10.2174/156800911794519752
- Chen, L., Miao, Y., Liu, M., Zeng, Y., Gao, Z., Di Peng et al. (2018). Pan-Cancer Analysis Reveals the Functional Importance of Protein Lysine Modification in Cancer Development. *Frontiers in Genetics*, 9, 254. doi: 10.3389/fgene.2018.00254
- Chiu, H.-W., Lin, S.-W., Lin, L.-C., Hsu, Y.-H., Lin, Y.-F., Ho, S.-Y. et al. (2015). Synergistic antitumor effects of radiation and proteasome inhibitor treatment in pancreatic cancer through the induction of autophagy and the downregulation of TRAF6. *Cancer Letters*, 365(2), 229–239. doi: 10.1016/j.canlet.2015.05.025
- Choi, J. S., Baek, H.-M., Kim, Suhkmann, Kim, M., Youk, J. H., Moon, H. J. et al. (2012). Hr-MAS MR spectroscopy of breast cancer tissue obtained with core needle biopsy: correlation with prognostic factors. *PloS One*, 7(12), e51712. doi: 10.1371/journal.pone.0051712
- Chong, J., Wishart, D. S., Xia, J. (2019). Using MetaboAnalyst 4.0 for Comprehensive and Integrative Metabolomics Data Analysis. *Current Protocols in Bioinformatics*, 68, 1–128. doi: 10.1002/cpbi.86

References

- Christensen, E., Bogner, A. N., Vandekeere, A., Tam, G. S., Patel, S. M., Becker, D. F. et al. (2020). In crystallo screening for proline analog inhibitors of the proline cycle enzyme PYCR1. *The Journal of Biological Chemistry*, 295(52), 18316–18327. doi: 10.1074/jbc.RA120.016106
- Coloff, J. L., Murphy, J. P., Braun, C. R., Harris, I., Shelton, L. M., Kami, K. et al. (2016). Differential Glutamate Metabolism in Proliferating and Quiescent Mammary Epithelial Cells. *Cell Metabolism*, 23(5), 867–880. doi: 10.1016/j.cmet.2016.03.016
- Conforti, F., Pala, L., Giaccone, G., Pas, T. de. (2020). Thymic epithelial tumors: From biology to treatment. *Cancer Treatment Reviews*, 86, 102014. doi: 10.1016/j.ctrv.2020.102014
- Daher, B., Vučetić, M., Pouysségur, J. (2020). Cysteine Depletion, a Key Action to Challenge Cancer Cells to Ferroptotic Cell Death. *Frontiers in Oncology*, 723. doi: 10.3389/fonc.2020.00723
- D'Aniello, C., Patriarca, E. J., Phang, J. M., Minchiotti, G. (2020). Proline Metabolism in Tumor Growth and Metastatic Progression. *Frontiers in Oncology*, 10, 776. doi: 10.3389/fonc.2020.00776
- Davies, A. M., Ho, C., Metzger, A. S., Beckett, L. A., Christensen, S., Tanaka, M. et al. (2007). Phase I study of two different schedules of bortezomib and pemetrexed in advanced solid tumors with emphasis on non-small cell lung cancer. *Journal of Thoracic Oncology : Official Publication of the International Association for the Study of Lung Cancer*, 2(12), 1112–1116. doi: 10.1097/JTO.0b013e31815ba7d0
- Detterbeck, F. C., Nicholson, A., Kondo, K., van Schil, P., Moran, C. (2011). The Masaoka-Koga stage classification for thymic malignancies: clarification and definition of terms. *Journal of Thoracic Oncology : Official Publication of the International Association for the Study of Lung Cancer*, 6(7 Suppl 3), S1710-6. doi: 10.1097/JTO.0b013e31821e8cff
- Dooley, Sarah, Anderson, C. (2016). Definitive IMRT for Stage III Thymic Carcinoma: A Brief Report and Literature Review. *Frontiers in Oncology*, 6, 219. doi: 10.3389/fonc.2016.00219
- Du, J., Zhou, X.-J. (2017). Precise Diagnosis and Treatment of Thymic Epithelial Tumors Based on Molecular Biomarkers. *Critical Reviews in Oncogenesis*, 22(5-6), 507–514. doi: 10.1615/CritRevOncog.2017020577
- Du, Z.-X., Zhang, H.-Y., Meng, X., Guan, Y., Wang, H.-Q. (2009). Role of oxidative stress and intracellular glutathione in the sensitivity to apoptosis induced by proteasome inhibitor in thyroid cancer cells. *BMC Cancer*, 9, 56. doi: 10.1186/1471-2407-9-56
- Dubiak-Szepietowska, M., Karczmarczyk, A., Jönsson-Niedziółka, M., Winckler, T., Feller, K.-H. (2016). Development of complex-shaped liver multicellular spheroids as a human-based model for nanoparticle toxicity assessment in vitro. *Toxicology and Applied Pharmacology*, 294, 78–85. doi: 10.1016/j.taap.2016.01.016
- Dumanskiy, Y. V., Stoliarova, O. Y., Syniachenko, O. V., Aliev, R. F., Iermolaeva, M. V., Sokrut, O. P. (2020). Comparative evaluation of purine dysmetabolism in gastric and pulmonary adenocarcinomas. *Experimental Oncology*, 42(3), 220–223. doi: 10.32471/exp-oncology.2312-8852.vol-42-no-3.15068

References

- Ehemann, V., Kern, M., Breinig, M., Schnabel, P. A., Gunawan, B., Schulten, H.-J. et al. (2008). Establishment, characterization and drug sensitivity testing in primary cultures of human thymoma and thymic carcinoma. *International Journal of Cancer*, *122*(12), 2719–2725. doi: 10.1002/ijc.23335
- Fan, T., El-Amouri, S. S., Macedo, J. K. A., Wang, Q., Song, H., Cassel, T., Lane, A. N. (2018). Stable Isotope-Resolved Metabolomics Shows Metabolic Resistance to Anti-Cancer Selenite in 3D Spheroids versus 2D Cell Cultures. *Metabolites*, *8*(3). doi: 10.3390/metabo8030040
- Feng, Y., Xiong, Y., Qiao, T., Li, Xiaofei, Jia, L., Han, Y. (2018). Lactate dehydrogenase A: A key player in carcinogenesis and potential target in cancer therapy. *Cancer Medicine*, *7*(12), 6124–6136. doi: 10.1002/cam4.1820
- Flynt, E., Bisht, K., Sridharan, V., Ortiz, M., Towfic, F., Thakurta, A. (2020). Prognosis, Biology, and Targeting of TP53 Dysregulation in Multiple Myeloma. *Cells*, *9*(2). doi: 10.3390/cells9020287
- Freyer, J. P., Fink, N., Schor, P. L., Coulter, J. R., Neeman, M., Sillerud, L. O. (1990). A system for viably maintaining a stirred suspension of multicellular spheroids during NMR spectroscopy. *NMR in Biomedicine*, *3*(5), 195–205. doi: 10.1002/nbm.1940030502
- Fujiwara, S., Kawano, Y., Yuki, H., Okuno, Y., Nosaka, K., Mitsuya, H., Hata, H. (2013). Pdk1 inhibition is a novel therapeutic target in multiple myeloma. *British Journal of Cancer*, *108*(1), 170–178. doi: 10.1038/bjc.2012.527
- Geistlinger, L., Csaba, G., Zimmer, R. (2016). Bioconductor's EnrichmentBrowser: seamless navigation through combined results of set- & network-based enrichment analysis. *BMC Bioinformatics*, *17*, 45. doi: 10.1186/s12859-016-0884-1
- Girard, N., Ruffini, E., Marx, A., Faivre-Finn, C., Peters, S. (2015). Thymic epithelial tumours: ESMO Clinical Practice Guidelines for diagnosis, treatment and follow-up. *Annals of Oncology : Official Journal of the European Society for Medical Oncology*, *26 Suppl 5*, v40-55. doi: 10.1093/annonc/mdv277
- Gogiashvili, M., Horsch, S., Marchan, R., Gianmoena, K., Cadenas, C., Tanner, B. et al. (2018a). Impact of intratumoral heterogeneity of breast cancer tissue on quantitative metabolomics using high-resolution magic angle spinning 1 H NMR spectroscopy. *NMR in Biomedicine*, *31*(2). doi: 10.1002/nbm.3862
- Gogiashvili, M., Horsch, S., Marchan, R., Gianmoena, K., Cadenas, C., Tanner, B. et al. (2018b). Impact of intratumoral heterogeneity of breast cancer tissue on quantitative metabolomics using high-resolution magic angle spinning 1 H NMR spectroscopy. *NMR in Biomedicine*, *31*(2). doi: 10.1002/nbm.3862
- Gogiashvili, M., Nowacki, J., Hergenröder, R., Hengstler, J. G., Lambert, J., Edlund, K. (2019). Hr-MAS NMR Based Quantitative Metabolomics in Breast Cancer. *Metabolites*, *9*(2). doi: 10.3390/metabo9020019
- Guo, Chunqing, Chen, S., Liu, W., Ma, Y., Li, J., Fisher, P. B. et al. (2019). Immunometabolism: A new target for improving cancer immunotherapy. *Advances in Cancer Research*, *143*, 195–253. doi: 10.1016/bs.acr.2019.03.004

References

- Hanahan, D., Weinberg, R. A. (2011). Hallmarks of cancer: the next generation. *Cell*, *144*(5), 646–674. doi: 10.1016/j.cell.2011.02.013
- Harris, M., Miles, M. A., Shekhar, T. M., Cerra, C., Georgy, S. R., Ryan, S. et al. (2020). The Proteasome Inhibitor Ixazomib Inhibits the Formation and Growth of Pulmonary and Abdominal Osteosarcoma Metastases in Mice. *Cancers*, *12*(5). doi: 10.3390/cancers12051207
- He, X., Lin, X., Cai, M., Zheng, X., Lian, L., Fan, D. et al. (2016). Overexpression of Hexokinase 1 as a poor prognosticator in human colorectal cancer. *Tumour Biology : the Journal of the International Society for Oncodevelopmental Biology and Medicine*, *37*(3), 3887–3895. doi: 10.1007/s13277-015-4255-8
- Heger, J. I., Froehlich, K., Pastuschek, J., Schmidt, Astrid, Baer, C., Mrowka, R. et al. (2018). Human serum alters cell culture behavior and improves spheroid formation in comparison to fetal bovine serum. *Experimental Cell Research*, *365*(1), 57–65. doi: 10.1016/j.yexcr.2018.02.017
- Henry, N. L., Hayes, Daniel. (2012). Cancer biomarkers. *Molecular Oncology*, *6*(2), 140–146. doi: 10.1016/j.molonc.2012.01.010
- Hsu, C.-H., Chan, J. K., Yin, C.-H., Lee, C.-C., Chern, C.-U., Liao, C.-I. (2019). Trends in the incidence of thymoma, thymic carcinoma, and thymic neuroendocrine tumor in the United States. *PLoS One*, *14*(12), e0227197. doi: 10.1371/journal.pone.0227197
- Huang, B., Belharazem, D., Li, L., Kneitz, S., Schnabel, P. A., Rieker, R. J. et al. (2013). Anti-Apoptotic Signature in Thymic Squamous Cell Carcinomas - Functional Relevance of Anti-Apoptotic BIRC3 Expression in the Thymic Carcinoma Cell Line 1889c. *Frontiers in Oncology*, *3*, 316. doi: 10.3389/fonc.2013.00316
- Hwang, T., Shaka, A. J. (1995). Water Suppression That Works. Excitation Sculpting Using Arbitrary Wave-Forms and Pulsed-Field Gradients. *Journal of Magnetic Resonance, Series a*, *112*(2), 275–279. doi: 10.1006/jmra.1995.1047
- Italiano, A. (2011). Prognostic or predictive? It's time to get back to definitions! *Journal of Clinical Oncology : Official Journal of the American Society of Clinical Oncology*, *29*(35), 4718; author reply 4718-9. doi: 10.1200/JCO.2011.38.3729
- Jensen, C., Teng, Y. (2020). Is It Time to Start Transitioning From 2D to 3D Cell Culture? *Frontiers in Molecular Biosciences*, *7*, 33. doi: 10.3389/fmolb.2020.00033
- Johnson, C. H., Ivanisevic, J., Siuzdak, G. (2016). Metabolomics: beyond biomarkers and towards mechanisms. *Nature Reviews. Molecular Cell Biology*, *17*(7), 451–459. doi: 10.1038/nrm.2016.25
- Kaira, K., Abe, M., Nakagawa, K., Ohde, Y., Okumura, T., Takahashi, T. et al. (2012). 18F-FDG uptake on PET in primary mediastinal non-thymic neoplasm: a clinicopathological study. *European Journal of Radiology*, *81*(9), 2423–2429. doi: 10.1016/j.ejrad.2011.09.017
- Kanehisa, M., Araki, M., Goto, S., Hattori, M., Hirakawa, M., Itoh, M. et al. (2008). Kegg for linking genomes to life and the environment. *Nucleic Acids Research*, *36*(Database issue), D480-4. doi: 10.1093/nar/gkm882

References

- Kelly, R. J. (2013). Thymoma versus thymic carcinoma: differences in biology impacting treatment. *Journal of the National Comprehensive Cancer Network : JNCCN*, *11*(5), 577–583. doi: 10.6004/jnccn.2013.0073
- Kelm, J. M., Timmins, N. E., Brown, C. J., Fussenegger, M., Nielsen, L. K. (2003). Method for generation of homogeneous multicellular tumor spheroids applicable to a wide variety of cell types. *Biotechnology and Bioengineering*, *83*(2), 173–180. doi: 10.1002/bit.10655
- Nunes, A., Barros, A., Costa, E., Moreira, A., & Correia, I. (2018). 3D tumor spheroids as in vitro models to mimic in vivo human solid tumors resistance to therapeutic drugs. *Biotechnology And Bioengineering*, *116*(1), 206-226. doi: 10.1002/bit.26845 [Add to Citavi project by DOI]
- Kennedy, L., Sandhu, J. K., Harper, M.-E., Cuperlovic-Culf, M. (2020). Role of Glutathione in Cancer: From Mechanisms to Therapies. *Biomolecules*, *10*(10). doi: 10.3390/biom10101429
- Keun, Hector. (2014). Metabolomic studies of patient material by high-resolution magic angle spinning nuclear magnetic resonance spectroscopy. *Methods in Enzymology*, *543*, 297–313. doi: 10.1016/B978-0-12-801329-8.00015-5
- Kovacs, H., Moskau, D. (2013). Cryogenic NMR Probes. In G. C. K. Roberts (Ed.), *Encyclopedia of Biophysics* (pp. 392–396). Berlin, Heidelberg: Springer Berlin Heidelberg. doi: 10.1007/978-3-642-16712-6_322
- Kuzume, T., Kubonishi, I., Takeuchi, S., Takeuchi, T., Iwata, J., Sonobe, H. et al. (1992). Establishment and characterization of a thymic carcinoma cell line (Ty-82) carrying t(15;19)(q15;p13) chromosome abnormality. *International Journal of Cancer*, *50*(2), 259–264. doi: 10.1002/ijc.2910500216
- Langhans, S. A. (2018). Three-Dimensional in Vitro Cell Culture Models in Drug Discovery and Drug Repositioning. *Frontiers in Pharmacology*, *9*, 6. doi: 10.3389/fphar.2018.00006
- Lazar, M. A., Birnbaum, M. J. (2012). Physiology. De-meaning of metabolism. *Science (New York, N.Y.)*, *336*(6089), 1651–1652. doi: 10.1126/science.1221834
- Lê Cao, K.-A., Boitard, S., Besse, P. (2011). Sparse PLS discriminant analysis: biologically relevant feature selection and graphical displays for multiclass problems. *BMC Bioinformatics*, *12*, 253. doi: 10.1186/1471-2105-12-253
- Lee, M., Hu, T. (2019). Computational Methods for the Discovery of Metabolic Markers of Complex Traits. *Metabolites*, *9*(4). doi: 10.3390/metabo9040066
- Lemasters, J. J. (2021). Metabolic implications of non-Electrogenic ATP/ADP exchange in Cancer cells: A mechanistic basis for the Warburg effect. *Biochimica Et Biophysica Acta. Bioenergetics*, 148410. doi: 10.1016/j.bbabo.2021.148410
- Li, Chun, Hu, J., Li, W., Song, G., Shen, J. (2016). Combined bortezomib-based chemotherapy and p53 gene therapy using hollow mesoporous silica nanospheres for p53 mutant non-small cell lung cancer treatment. *Biomaterials Science*, *5*(1), 77–88. doi: 10.1039/C6BM00449K
- Li, J.-Q., Wu, Xian, Gan, L., Yang, X.-L., Miao, Z.-H. (2017). Hypoxia induces universal but differential drug resistance and impairs anticancer mechanisms of 5-fluorouracil in

References

- hepatoma cells. *Acta Pharmacologica Sinica*, 38(12), 1642–1654. doi: 10.1038/aps.2017.79
- Liang, Q., Wang, C., Li, B., Zhang, A.-H. (2015). Metabolic fingerprinting to understand therapeutic effects and mechanisms of silybin on acute liver damage in rat. *Pharmacognosy Magazine*, 11(43), 586–593. doi: 10.4103/0973-1296.160469
- Lien, E. C., Lyssiotis, C. A., Juvekar, A., Hu, H., Asara, J. M., Cantley, L. C., Toker, A. (2016). Glutathione biosynthesis is a metabolic vulnerability in PI(3)K/Akt-driven breast cancer. *Nature Cell Biology*, 18(5), 572–578. doi: 10.1038/ncb3341
- Lin, L.-L., Huang, H.-C., Juan, H.-F. (2012). Discovery of biomarkers for gastric cancer: a proteomics approach. *Journal of Proteomics*, 75(11), 3081–3097. doi: 10.1016/j.jprot.2012.03.046
- Liu, C.-W., Hua, K.-T., Li, K.-C., Kao, H.-F., Hong, R.-L., Ko, J.-Y. et al. (2017). Histone Methyltransferase G9a Drives Chemotherapy Resistance by Regulating the Glutamate-Cysteine Ligase Catalytic Subunit in Head and Neck Squamous Cell Carcinoma. *Molecular Cancer Therapeutics*, 16(7), 1421–1434. doi: 10.1158/1535-7163.MCT-16-0567-T
- Loayza-Puch, F., Rooijers, K., Buil, L. C. M., Zijlstra, J., Oude Vrielink, J. F., Lopes, R. et al. (2016). Tumour-specific proline vulnerability uncovered by differential ribosome codon reading. *Nature*, 530(7591), 490–494. doi: 10.1038/nature16982
- Ludwig, N., Gillespie, D. G., Reichert, T. E., Jackson, E. K., Whiteside, T. L. (2020). Purine Metabolites in Tumor-Derived Exosomes May Facilitate Immune Escape of Head and Neck Squamous Cell Carcinoma. *Cancers*, 12(6). doi: 10.3390/cancers12061602
- Machálková, M., Pavlatovská, B., Michálek, J., Pruška, A., Štěpka, K., Nečasová, T. et al. (2019). Drug Penetration Analysis in 3D Cell Cultures Using Fiducial-Based Semiautomatic Coregistration of MALDI MSI and Immunofluorescence Images. *Analytical Chemistry*, 91(21), 13475–13484. doi: 10.1021/acs.analchem.9b02462
- Maiso, P., Huynh, D., Moschetta, M., Sacco, A., Aljawai, Y., Mishima, Y. et al. (2015). Metabolic signature identifies novel targets for drug resistance in multiple myeloma. *Cancer Research*, 75(10), 2071–2082. doi: 10.1158/0008-5472.CAN-14-3400
- Maruvada, P., Wang, W., Wagner, P. D., Srivastava, S. (2005). Biomarkers in molecular medicine: cancer detection and diagnosis. *BioTechniques, Suppl*, 9–15. doi: 10.2144/05384SU04
- Marx, Alexander, Belharazem, D., Lee, D.-H., Popovic, Z. V., Reißfelder, C., Schalke, B. et al. (2021). Molecular pathology of thymomas: implications for diagnosis and therapy. *Virchows Archiv : an International Journal of Pathology*, 478(1), 101–110. doi: 10.1007/s00428-021-03068-8
- Marx, Alexander, Pfister, F., Schalke, B., Saruhan-Direskeneli, G., Melms, A., Ströbel, P. (2013). The different roles of the thymus in the pathogenesis of the various myasthenia gravis subtypes. *Autoimmunity Reviews*, 12(9), 875–884. doi: 10.1016/j.autrev.2013.03.007
- Marx, Alexander, Yamada, Y., Simon-Keller, K., Schalke, B., Willcox, N., Ströbel, P., Weis, C.-A. (2021). Thymus and autoimmunity. *Seminars in Immunopathology*, 43(1), 45–64. doi: 10.1007/s00281-021-00842-3

References

- Melnik, D., Sahana, J., Corydon, T. J., Kopp, S., Nassef, M. Z., Wehland, M. et al. (2020). Dexamethasone Inhibits Spheroid Formation of Thyroid Cancer Cells Exposed to Simulated Microgravity. *Cells*, 9(2). doi: 10.3390/cells9020367
- Miller, J. (2020). The function of the thymus and its impact on modern medicine. *Science (New York, N.Y.)*, 369(6503). doi: 10.1126/science.aba2429
- Min, L., Choy, E., Tu, C., Hornicek, F., Duan, Z. (2017). Application of metabolomics in sarcoma: From biomarkers to therapeutic targets. *Critical Reviews in Oncology/hematology*, 116, 1–10. doi: 10.1016/j.critrevonc.2017.05.003
- Minard, K. R., Guo, X., Wind, R. A. (1998). Quantitative ¹H MRI and MRS microscopy of individual V79 lung tumor spheroids. *Journal of Magnetic Resonance (San Diego, Calif. : 1997)*, 133(2), 368–373. doi: 10.1006/jmre.1998.1493
- Moreau, P., Richardson, P. G., Cavo, M., Orłowski, R. Z., San Miguel, Jesús F., Palumbo, A., Harousseau, J.-L. (2012). Proteasome inhibitors in multiple myeloma: 10 years later. *Blood*, 120(5), 947–959. doi: 10.1182/blood-2012-04-403733
- Mueller, W. H. (1991). Biological markers in epidemiology. Edited by B. S. Hulka, T. C. Wilcosky, and J. D. Griffith. xi + 236 pp. New York: Oxford University Press, 1990, \$40.00 (cloth). *American Journal of Human Biology*, 3(2), 218–219. doi: 10.1002/ajhb.1310030225
- Mussap, M., Zaffanello, M., Fanos, V. (2018). Metabolomics: a challenge for detecting and monitoring inborn errors of metabolism. *Annals of Translational Medicine*, 6(17), 338. doi: 10.21037/atm.2018.09.18
- Narayanan, D., Ma, S., Özcelik, D. (2020). Targeting the Redox Landscape in Cancer Therapy. *Cancers*, 12(7). doi: 10.3390/cancers12071706
- Naylor, S. (2003). Biomarkers: current perspectives and future prospects. *Expert Review of Molecular Diagnostics*, 3(5), 525–529. doi: 10.1586/14737159.3.5.525
- Niewerth, D., Jansen, G., Assaraf, Y. G., Zweegman, S., Kaspers, G. J. L., Cloos, J. (2015). Molecular basis of resistance to proteasome inhibitors in hematological malignancies. *Drug Resistance Updates : Reviews and Commentaries in Antimicrobial and Anticancer Chemotherapy*, 18, 18–35. doi: 10.1016/j.drug.2014.12.001
- Obeng, E. A., Carlson, L. M., Gutman, D. M., Harrington, W. J., Lee, K., Boise, L. H. (2006). Proteasome inhibitors induce a terminal unfolded protein response in multiple myeloma cells. *Blood*, 107(12), 4907–4916. doi: 10.1182/blood-2005-08-3531
- Orłowski, R. Z., Nagler, A., Sonneveld, P., Bladé, J., Hajek, R., Spencer, A. et al. (2007). Randomized phase III study of pegylated liposomal doxorubicin plus bortezomib compared with bortezomib alone in relapsed or refractory multiple myeloma: combination therapy improves time to progression. *Journal of Clinical Oncology : Official Journal of the American Society of Clinical Oncology*, 25(25), 3892–3901. doi: 10.1200/JCO.2006.10.5460
- Palma, A., Grande, S., Luciani, A. M., Mlynárik, V., Guidoni, L., Viti, V., Rosi, A. (2016). Metabolic Study of Breast MCF-7 Tumor Spheroids after Gamma Irradiation by (¹H) NMR Spectroscopy and Microimaging. *Frontiers in Oncology*, 6, 105. doi: 10.3389/fonc.2016.00105

References

- Palubeckaitė, I., Crooks, L., Smith, D., Cole, L. M., Bram, H., Le Maitre, C. et al. (2020). Mass spectrometry imaging of endogenous metabolites in response to doxorubicin in a novel 3D osteosarcoma cell culture model. *Journal of Mass Spectrometry : JMS*, 55(4), e4461. doi: 10.1002/jms.4461
- Park, V., Yoon, D., Koo, J. S., Kim, E.-K., Kim, Seung, Choi, J. S. et al. (2016). Intratumoral Agreement of High-Resolution Magic Angle Spinning Magnetic Resonance Spectroscopic Profiles in the Metabolic Characterization of Breast Cancer. *Medicine*, 95(15), e3398. doi: 10.1097/MD.0000000000003398
- Patatsos, K., Shekhar, T. M., Hawkins, C. J. (2018). Pre-clinical evaluation of proteasome inhibitors for canine and human osteosarcoma. *Veterinary and Comparative Oncology*, 16(4), 544–553. doi: 10.1111/vco.12413
- Phang, J. M. (2019). Proline Metabolism in Cell Regulation and Cancer Biology: Recent Advances and Hypotheses. *Antioxidants & Redox Signaling*, 30(4), 635–649. doi: 10.1089/ars.2017.7350
- Pretzier, G., Jäger, H., Neger, T., Philipp, H., Woisetschlager, J. (1992). Comparison of Different Methods of Abel Inversion Using Computer Simulated and Experimental Side-On Data. *Zeitschrift Für Naturforschung a*, 47(9), 955–970. doi: 10.1515/zna-1992-0906
- Putri, S. P., Yamamoto, S., Tsugawa, H., Fukusaki, E. (2013). Current metabolomics: technological advances. *Journal of Bioscience and Bioengineering*, 116(1), 9–16. doi: 10.1016/j.jbiosc.2013.01.004
- Radovich, M., Pickering, C. R., Felau, I., Ha, G., Zhang, H., Jo, H. et al. (2018). The Integrated Genomic Landscape of Thymic Epithelial Tumors. *Cancer Cell*, 33(2), 244–258.e10. doi: 10.1016/j.ccell.2018.01.003
- Rangel-Huerta, O. D., Pastor-Villaescusa, B., Gil, A. (2019). Are we close to defining a metabolomic signature of human obesity? A systematic review of metabolomics studies. *Metabolomics : Official Journal of the Metabolomic Society*, 15(6), 93. doi: 10.1007/s11306-019-1553-y
- Roeten, M. S. F., Cloos, J., Jansen, G. (2018). Positioning of proteasome inhibitors in therapy of solid malignancies. *Cancer Chemotherapy and Pharmacology*, 81(2), 227–243. doi: 10.1007/s00280-017-3489-0
- Roy, M., Finley, S. D. (2019). Metabolic reprogramming dynamics in tumor spheroids: Insights from a multicellular, multiscale model. *PLoS Computational Biology*, 15(6), e1007053. doi: 10.1371/journal.pcbi.1007053
- Russell, S., Wojtkowiak, J., Neilson, A., Gillies, R. J. (2017). Metabolic Profiling of healthy and cancerous tissues in 2D and 3D. *Scientific Reports*, 7(1), 15285. doi: 10.1038/s41598-017-15325-5
- Rusz, M., Rampler, E., Keppler, B. K., Jakupec, M. A., Koellensperger, G. (2019). Single Spheroid Metabolomics: Optimizing Sample Preparation of Three-Dimensional Multicellular Tumor Spheroids. *Metabolites*, 9(12). doi: 10.3390/metabo9120304
- Sanchez, W. Y., McGee, S. L., Connor, T., Mottram, B., Wilkinson, A., Whitehead, J. P. et al. (2013). Dichloroacetate inhibits aerobic glycolysis in multiple myeloma cells and increases

References

- sensitivity to bortezomib. *British Journal of Cancer*, 108(8), 1624–1633. doi: 10.1038/bjc.2013.120
- Sharma, N. S., Gupta, V. K., Garrido, V. T., Hadad, R., Durden, B. C., Kesh, K. et al. (2020). Targeting tumor-intrinsic hexosamine biosynthesis sensitizes pancreatic cancer to anti-PD1 therapy. *The Journal of Clinical Investigation*, 130(1), 451–465. doi: 10.1172/JCI127515
- Song, I.-S., Jeong, Y., Jeong, S., Heo, H. J., Kim, H., Lee, S. et al. (2013). Combination treatment with 2-methoxyestradiol overcomes bortezomib resistance of multiple myeloma cells. *Experimental & Molecular Medicine*, 45, e50. doi: 10.1038/emm.2013.104
- Song, Z., Wang, H., Yin, X., Deng, P., Jiang, W. (2019). Application of NMR metabolomics to search for human disease biomarkers in blood. *Clinical Chemistry and Laboratory Medicine*, 57(4), 417–441. doi: 10.1515/cclm-2018-0380
- Soriano, G. P., Besse, L., Li, N., Kraus, M., Besse, A., Meeuwenoord, N. et al. (2016). Proteasome inhibitor-adapted myeloma cells are largely independent from proteasome activity and show complex proteomic changes, in particular in redox and energy metabolism. *Leukemia*, 30(11), 2198–2207. doi: 10.1038/leu.2016.102
- Sukjoi, W., Ngamkham, J., Attwood, P. V., Jitrapakdee, S. (2021). Targeting Cancer Metabolism and Current Anti-Cancer Drugs. *Advances in Experimental Medicine and Biology*, 1286, 15–48. doi: 10.1007/978-3-030-55035-6_2
- Thomas de Montpréville, V., Quilhot, P., Chalabreysse, L., Muret, A. de, Hofman, V., Lantuéjoul, S. et al. (2015). Glut-1 intensity and pattern of expression in thymic epithelial tumors are predictive of WHO subtypes. *Pathology, Research and Practice*, 211(12), 996–1002. doi: 10.1016/j.prp.2015.10.005
- Thompson, R. M., Dytfeld, D., Reyes, L., Robinson, R. M., Smith, B., Manevich, Y. et al. (2017). Glutaminase inhibitor CB-839 synergizes with carfilzomib in resistant multiple myeloma cells. *Oncotarget*, 8(22), 35863–35876. doi: 10.18632/oncotarget.16262
- Thurtle, D. R., Jenkins, V., Pharoah, P. D., Gnanapragasam, V. J. (2019). Understanding of prognosis in non-metastatic prostate cancer: a randomised comparative study of clinician estimates measured against the PREDICT prostate prognostic model. *British Journal of Cancer*, 715–718. doi: 10.1038/s41416-019-0569-4
- Tilgner, M., Vater, T. S., Habbel, P., Cheng, L. L. (2019). High-Resolution Magic Angle Spinning (HRMAS) NMR Methods in Metabolomics. *Methods in Molecular Biology (Clifton, N.J.)*, 2037, 49–67. doi: 10.1007/978-1-4939-9690-2_4
- Travis, W. D., Brambilla, E., Nicholson, A., Yatabe, Y., Austin, J. H. M., Beasley, M. B. et al. (2015). The 2015 World Health Organization Classification of Lung Tumors: Impact of Genetic, Clinical and Radiologic Advances Since the 2004 Classification. *Journal of Thoracic Oncology : Official Publication of the International Association for the Study of Lung Cancer*, 10(9), 1243–1260. doi: 10.1097/JTO.0000000000000630
- Trifonova, O., Knight, R. A., Lisitsa, A., Melino, G., Antonov, A. V. (2016). Exploration of individuality in drug metabolism by high-throughput metabolomics: The fast line for personalized medicine. *Drug Discovery Today*, 21(1), 103–110. doi: 10.1016/j.drudis.2015.07.011

References

- Tseng, Y.-C., Tseng, Y.-H., Kao, H.-L., Hsieh, C.-C., Chou, T.-Y., Goan, Y.-G. et al. (2017). Long term oncological outcome of thymoma and thymic carcinoma - an analysis of 235 cases from a single institution. *PloS One*, *12*(6), e0179527. doi: 10.1371/journal.pone.0179527.
- Ussher, J. R., Elmariah, S., Gerszten, R. E., Dyck, J. R. B. (2016). The Emerging Role of Metabolomics in the Diagnosis and Prognosis of Cardiovascular Disease. *Journal of the American College of Cardiology*, *68*(25), 2850–2870. doi: 10.1016/j.jacc.2016.09.972
- Van Loenhout, J., Peeters, M., Bogaerts, A., Smits, E., Deben, C. (2020). Oxidative Stress-Inducing Anticancer Therapies: Taking a Closer Look at Their Immunomodulating Effects. *Antioxidants (Basel, Switzerland)*, *9*(12). doi: 10.3390/antiox9121188
- Vest, C. M. (1974). Formation of images from projections: Radon and Abel transforms *Journal of the Optical Society of America*, *64*(9), 1215. doi: 10.1364/JOSA.64.001215
- Vinci, M., Gowan, S., Boxall, F., Patterson, L., Zimmermann, M., Court, W. et al. (2012). Advances in establishment and analysis of three-dimensional tumor spheroid-based functional assays for target validation and drug evaluation. *BMC Biology*, *10*, 29. doi: 10.1186/1741-7007-10-29
- Vorrink, S. U., Ullah, S., Schmidt, S., Nandania, J., Velagapudi, V., Beck, O. et al. (2017). Endogenous and xenobiotic metabolic stability of primary human hepatocytes in long-term 3D spheroid cultures revealed by a combination of targeted and untargeted metabolomics. *FASEB Journal : Official Publication of the Federation of American Societies for Experimental Biology*, *31*(6), 2696–2708. doi: 10.1096/fj.201601375R
- Wilson, F. P., Berns, J. S. (2012). Onco-nephrology: tumor lysis syndrome. *Clinical Journal of the American Society of Nephrology : CJASN*, *7*(10), 1730–1739. doi: 10.2215/CJN.03150312
- Xia, J., Wishart, D. S. (2010). Metpa: a web-based metabolomics tool for pathway analysis and visualization. *Bioinformatics (Oxford, England)*, *26*(18), 2342–2344. doi: 10.1093/bioinformatics/btq418
- Xue, J., Li, Y., Yi, J., Jiang, H. (2019). Havcr1 Affects the MEK/ERK Pathway in Gastric Adenocarcinomas and Influences Tumor Progression and Patient Outcome. *Gastroenterology Research and Practice*, *2019*, 6746970. doi: 10.1155/2019/6746970
- Yamada, Y., Simon-Keller, K., Belharazem-Vitacolonna, D., Bohnenberger, H., Kriegsmann, M., Kriegsmann, K. et al. (2021). A Tuft Cell-Like Signature Is Highly Prevalent in Thymic Squamous Cell Carcinoma and Delineates New Molecular Subsets Among the Major Lung Cancer Histotypes. *Journal of Thoracic Oncology : Official Publication of the International Association for the Study of Lung Cancer*, *16*(6), 1003–1016. doi: 10.1016/j.jtho.2021.02.008
- Yamada, Y., Weis, C.-A., Thelen, J., Sticht, C., Schalke, B., Ströbel, P., Marx, Alexander. (2020). Thymoma Associated Myasthenia Gravis (TAMG): Differential Expression of Functional Pathways in Relation to MG Status in Different Thymoma Histotypes. *Frontiers in Immunology*, *11*, 664. doi: 10.3389/fimmu.2020.00664

References

- Yang, X., Zhao, K., Li, Chuan, Yang, Y., Guo, Chenglin, Pu, Y., Liu, L. (2020). Thymic Squamous Cell Carcinoma: A Population-Based Surveillance, Epidemiology, and End Result Analysis. *Frontiers in Oncology*, *10*, 592023. doi: 10.3389/fonc.2020.592023
- Zaal, E. A., Berkers, C. R. (2018). The Influence of Metabolism on Drug Response in Cancer. *Frontiers in Oncology*, *8*, 500. doi: 10.3389/fonc.2018.00500
- Zhang, Junmin, Duan, D., Song, Z.-L., Liu, T., Hou, Y., Fang, J. (2021). Small molecules regulating reactive oxygen species homeostasis for cancer therapy. *Medicinal Research Reviews*, *41*(1), 342–394. doi: 10.1002/med.21734
- Zheng, H., Dong, B., Ning, J., Shao, X., Zhao, L., Jiang, Q. et al. (2020). Nmr-based metabolomics analysis identifies discriminatory metabolic disturbances in tissue and biofluid samples for progressive prostate cancer. *Clinica Chimica Acta; International Journal of Clinical Chemistry*, *501*, 241–251. doi: 10.1016/j.cca.2019.10.046

7 CURRICULUM VITAE

Personal Information

Name and first name: Mohammad Ibrahim Mohammad AlWahsh

Birth date: 07.03.1994

Place of birth: Dubai, UAE

Nationality: Jordanian

School education

June 2011 High School Diploma, Al Shaarawi School, 35 14 A St - Al Manara - Dubai - United Arab Emirates (Grade: Excellent GPA)

University education

2011-2015 B.Sc. degree in Pharmacy with Excellent GPA from Alzaytonah University of Jordan, Amman

2015-2018 M.Sc. degree in Pharmaceutical science with Excellent GPA, Master thesis Title “Molecular and Metabolic Signatures Associated with Acute Paracetamol Multiple Doses Toxicity in Mice” In collaboration between Alzaytonah University of Jordan-Amman, University of Heidelberg Germany and Leibniz Institut für Analytische Wissenschaften – ISAS – e.V., Dortmund, Germany

Patents related to the thesis

Hergenröder, R.; Lambert, J.; **AlWahsh, M.**; Raschke, H.; Knitsch, R. „Verfahren zur Analyse des Metaboloms dreidimensionaler lebender Zellkulturen mittels NMR-Spektroskopie“, DPMA Nr. 64/24651 jm/s.

Publications related to the thesis

Robert Knitsch, **Mohammad AlWahsh***, Hannes Raschke, Jörg Lambert, and Roland Hergenröder. (2021) In Vitro Spatio-Temporal NMR Metabolomics of Living 3D Cell Models. Anal, Chem, <https://doi.org/10.1021/acs.analchem.1c02221>

Farhat, J., Pandey, I., **AlWahsh, M***. (2021) Transcending towards advanced 3D cell culture modalities: A review about an emerging paradigm in translational oncology. Cells Journal, <https://doi.org/10.3390/cells10071657>

Mohammad Alwahsh*, Robert Knitsch, Rosemarie Marchan, Jörg Lambert, Christian Hoerner, Xiaonan Zhang, Berthold Schalke, De Hyung Lee, Elena Bulut, Thomas Graeter, German Ott, Katrin Kurz, Gerhard Preissler, Sebastian Schölch, Zhihan Yao, Carsten Sticht, Philipp Ströbel, Roland Hergenröder, Alexander Marx and Djeda Belharazem. (2022) Metabolic profiling of thymic epithelial tumors hints to a strong Warburg effect, glutaminolysis and precarious redox homeostasis as potential therapeutic targets. Cancers, (Under revision)

8 ACKNOWLEDGMENT

First of all I would like to deeply thank my main supervisor Prof. Dr. med. Alexander Marx for his endless support, guidance, help and time during my doctoral study, I am so glad that I learnt from you and I was one of your students.

A huge thank to my Co-Advisor Dr. Roland Hergenröder at Leibniz Institute for Analytical Sciences-ISAS- Dortmund for his beautiful support that he gave to me, his trust on me and my work, which allowed me to do my masters, doctoral work at his labrotory with endless support I am happy that I am moving step by step with your help and support again thank you!

Special and BIG thank to the most closest person to me the one who I shared with all my life events during my doctoral studies Dr. Jörg Lambert! You were more than a Co-Advisor to me! I think words can't describe you Dr. Lambert. I am so glad that I was with you at the same office I learned from your endless knowledge in NMR day by day. You are the most honest and white heart person I've ever seen in my whole life! A great scientist with white heart. Many thanks and I highly appreciate everything you did to know and I will never ever forget that. Thank you till the end of this life...!

I would like to thank the most smartest and kindest person Dr. Rosemarie Marchan! Thank you very much you are great I am lucky that you were one of my Co-Adisvors guiding me with toxicological staff during my studies I learned a lot from your knowledge, whenever we make meeting you were one of the reasons why I reached this point! I am happy that you were part of this and I am more happy that we will keep working afterwards.

Of course I won't forget to thank Mr (Doottoo) Hannes Raschke a very skilled engineer. I highly appreciate your endless help with thinking, solving the problems and producing many nice ideas and disgenes and most important thing for organizing the lunch (Trouble) break with my weirdo type of food ;)

To Dr. Robert Knitsch a cardial thank to you! You came during my doctoral work you boosted the work very nicely you made a lot of things working I am happy that I learned from you and I am so happy that our work is moving forward and getting more and more again thank you very much Robert!

Many Thanks to Dr. Djeda Belharazem for her support and help at the begning to contiune my PhD project I would never forget this.

To all my colleagues at ISAS Dortmund, IfADo Dortmund and Medical faculty Mannheim (Heidelberg University) thank you very much for your help and support.

ACKNOWLEDGMENT

I would like also to thank Alzaytoonah university of Jordan for supporting my studies and helping me during my doctoral work looking forward to start my job.

A huge thank to Karo Zajac for her help with imaging and organizing.

I would like to thank Prof. Kristina Lorenz and her group in Dortmund for supporting me and allowing me to work in their labs (Edeltraut, Jonas and Dr Elen Tolstik)

To Esraa My lovely beautiful and peaceful wife thank you for your support you were with me during my most important life events! I got to know you during my bachelor studies and we celebrated together my bachelor and masters graduation and I hope now we can celebrate my doctoral graduation with our lovely small Zain

To my father Prof. Dr. Ibrahim AlWahsh the person who deeply encouraged me to go into this field and to continue my studies thank you for your endless support

To my mom your the reason why I am here, you were the cure for my problems your phone calls, messages were like the medicine for any problem thank you very much!

To my brother (Asal) and his lovely wife (Amal) thanks a lot for your support I am glad that you both will come to my defense

Also I would like to thank a special person to my heart that has an important place. Wasan your more than a sister thank you very much for your care and help during my studies I would never ever forget this I wish the best for you and your family

Many thanks go to my sisters (Hadeel, Ghasaq and Assel) for supporting me and the endless phone calls.

Thanks to Franziska Kappenberg, TU Dortmund for generating the DS curves.

Also I would like to thank the Ministerium für Innovation, Wissenschaft und Forschung des Landes Nordrhein-Westfalen, the Senatsverwaltung für Wirtschaft, Technologie und Forschung des Landes Berlin, and the Bundesministerium für Bildung und Forschung is gratefully acknowledged.

I would not finish my thanks without mentioning an important person that has a great impact in my life. Dr Lama Hamadneh thank you very much for your endless support and guidance and great advice.

I would also like to thank my best friends Ahmad Khalifa, Ward, Mahmoud and Abdullah AlRamahi we were together via phone always and you guys deserve a big thank

To all my lovely friends here in Germany, Dubai and Jordan thank you very much